Karlsruhe Institute of Technology

# Angular Correlations and Soft Jets as Probes of Parton Showers

## Winkelkorrelationen und weiche Jets für die Untersuchung von Partonschauern

Masterarbeit
von

Nadine Fischer

am Institut für Theoretische Physik
der Fakultät für Physik

| | |
|---|---|
| Referent: | PD Dr. S. Gieseke |
| Korreferent: | Prof. Dr. U. Nierste |

Dezember 2013

last modified: January 2014

Ich versichere, dass ich die vorliegende Arbeit selbständig verfasst und keine anderen als die angegebenen Quellen und Hilfsmittel verwendet habe.

Nadine Fischer<br>
Karlsruhe, den 10. Dezember 2013

Als Masterarbeit anerkannt.

PD Dr. Stefan Gieseke<br>
Karlsruhe, den 10. Dezember 2013

# Contents


**1 Introduction** **1**

**2 Quantum Chromodynamics and Standard Model** **3**
- 2.1 The QCD Lagrangian . . . 3
- 2.2 Asymptotic Freedom and Confinement . . . 4
- 2.3 Standard Model . . . 5

**3 The Experiment** **7**
- 3.1 The LEP Collider . . . 7
- 3.2 The OPAL Experiment . . . 7

**4 Physics of Event Generators** **9**
- 4.1 Hard Processes . . . 9
- 4.2 Parton Shower . . . 10
  - 4.2.1 Parton Branching in the Collinear Limit . . . 10
  - 4.2.2 Coherent Branching and Angular Ordering . . . 12
  - 4.2.3 The Colour Dipole Model . . . 13
  - 4.2.4 Antenna Functions . . . 14
  - 4.2.5 Sudakov Form Factors and the Shower Chain . . . 15
- 4.3 Hadronization Models . . . 16
  - 4.3.1 Independent Fragmentation . . . 16
  - 4.3.2 String Model . . . 17
  - 4.3.3 Cluster Model . . . 17

**5 Monte Carlo Event Generators and Analysis Tools** **19**
- 5.1 Hard Process . . . 19
- 5.2 Shower Algorithm . . . 20
  - 5.2.1 Herwig++ Shower Algorithms . . . 21
  - 5.2.2 Vincia Shower Algorithm . . . 24
  - 5.2.3 Pythia8 Shower Algorithm . . . 25
- 5.3 Matching . . . 26
- 5.4 Hadronization . . . 28
  - 5.4.1 Cluster Model in Herwig++ . . . 28
  - 5.4.2 Lund String Model in Pythia8 . . . 29
- 5.5 The Rivet Analysis Tool . . . 31
- 5.6 The Professor Tuning System . . . 31

**6 Analyses for the Simulation** **33**
- 6.1 Basics: Jet Algorithms . . . 33

6.2 Analysis on Parton Level . . . 35
6.3 Influence of Hadronization . . . 36
6.3.1 Observables . . . 36
6.3.2 Analysis 1: $k_t$ Algorithm with $y_{\text{cut}}$ . . . 38
6.3.3 Analysis 2: $k_t$ Algorithm with $y_{3\to 4,\text{cut}}$ . . . 38
6.3.4 Analysis 3: Anti-$k_t$ Algorithm . . . 41
6.3.5 Conclusions . . . 42
6.4 Asymmetries . . . 43
6.5 Experimental Resolution . . . 47
6.6 Conclusions . . . 48

**7 Tuning 49**
7.1 Input for the Tuning . . . 49
7.1.1 Parameters . . . 49
7.1.2 Observables . . . 50
7.1.3 Tuning Procedure . . . 50
7.2 Results . . . 51
7.2.1 Hadronization Effects . . . 54
7.2.2 Eigentunes . . . 54
7.2.3 New Observables and Experimental Resolution . . . 57
7.3 Conclusions . . . 57

**8 Data Analysis 61**
8.1 Selection of Events . . . 61
8.2 Reconstruction and Correction . . . 61
8.3 Systematic Uncertainties . . . 63

**9 Comparison of LEP Data with Monte Carlo Event Generators 65**
9.1 Observables . . . 65
9.2 General Comparison . . . 67
9.3 Strong and Smooth Ordering in Vincia . . . 78
9.4 Matching . . . 81

**10 Summary and Conclusions 85**

**A Tuning 87**

**B LEP Data 103**

**Bibliography 105**

**Acknowledgements 109**

# 1. Introduction

Besides the standard separation of natural sciences into theory and experiment, the simulation of physical processes came up as a third mainstay during the last decades. For instance, Monte Carlo event generators play an essential role in collider physics. By simulating the final states of particle collisions they are used to compare theoretical models with data measurements in experiments such as the Large Electron Positron Collider (LEP).

The theory of strong interactions is called Quantum Chromodynamics (QCD) and is formulated in terms of quarks, antiquarks and gluons, collectively referred to as partons. The event generation starts by generating scattering processes on a probabilistic basis by calculating the corresponding amplitude with perturbation theory. The partons remaining after the hard process often radiate additional gluons, so-called bremsstrahlung gluons, or undergo other branching processes. This radiation is calculated with a careful treatment of perturbation theory during the parton shower. Nature tells us, that partons are never observed as free states. Therefore the partons have to be transferred into collimated sprays of hadrons, so-called jets, at non-perturbative scales.

The processes of QCD are very dominant in the high-energy collisions described before. In the course of searches for new particles, such as the Higgs boson, or searches for beyond the Standard Model physics the QCD effects should be controlled on a very high level. Thereby the QCD background is subtracted from the total signal leaving a precise signal for the process of interest. Besides the importance for special searches, the properties of QCD are interesting by themselves. Events with underlying QCD processes are usually multi-jet events, containing two or more jets initiated by quarks and gluons that are either produced during the hard process or originate in additional emissions. That is why the modelling of QCD jets is very important for multi-purpose Monte Carlo event generators for high-energy collisions, such as Herwig++ [1] or Pythia8 [2]. The characteristics of jets are determined by the implementation of the parton shower algorithm. Properties such as QCD colour coherence, the destructive interference effect between colour-connected partons, or the emissions of soft jets are implemented in different ways. Therefore the comparison of different models for the shower algorithm with data measurements can give some indication of QCD properties.

Chapter 2 provides a short overview of the theory of strong interactions and the Standard Model whereas Chapter 4 aims at giving the most important physical features that are used to build up a shower algorithm. The basics of current hadronization models are described as well. Chapter 5 continues with details on how the formulas presented before are implemented in the different Monte Carlo generators and presents the main free parameters of the theoretical models.

In Chapter 6 the analysis used for measuring shower properties is described, including information about how events are selected in order to be sensitive to the parton shower and which observables can be used to compare the different shower implementations. In order to ensure a fair comparison of the latter Chapter 7 deals with constraining the free parameters of the theoretical models by using existing data, which is referred to as generator tuning.

For the validation of Monte Carlo event generators it is crucial to compare its predictions to real data. Therefore Chapter 8 deals with the analysis of LEP data and provides information about the event selection, reconstruction and correction procedure and systematical errors of the data. The comparison to the event generators is presented in Chapter 9 and finally Chapter 10 rounds up with a summary and some conclusions.

# 2. Quantum Chromodynamics and Standard Model

The Standard Model of Particle Physics (SM) is a combination of two relativistic quantum field theories, Quantum Chromodynamics (QCD) and the electroweak theory, and its underlying gauge group is therefore the

$$\mathrm{SU}(3)_\mathrm{C} \times \mathrm{SU}(2)_\mathrm{L} \times \mathrm{U}(1)_\mathrm{Y} \; . \tag{2.1}$$

The SM is able to describe all known fundamental particles and forces (except for gravity) in nature.

Since this thesis deals with QCD coherence the basic properties of QCD are outlined in this chapter followed by a description of the SM. A more detailed discussion of QCD and the SM can be found in many textbooks, for example in Refs. [3–5].

## 2.1 The QCD Lagrangian

The theory of strong interaction is described by a non-abelian gauge theory based on the $\mathrm{SU}(3)_\mathrm{C}$ gauge group where C stands for colour. The classical QCD Lagrangian with the massive quark fields $\Psi_f$ of flavour $f$ is

$$\mathcal{L}_\mathrm{QCD} = \sum_{f=u,d,\ldots} \bar{\Psi}_f (i\gamma^\mu D_\mu - m_f)\Psi_f - \frac{1}{4} G^{a\mu\nu} G^a_{\mu\nu} \tag{2.2}$$

with the covariant derivative

$$D_\mu = \partial_\mu - i g_s T^a G^a_\mu \; . \tag{2.3}$$

The eight massless gluon fields in the adjoint representation of the $\mathrm{SU}(3)_\mathrm{C}$ gauge group are $G^a_\mu$ with $G_\mu = G^a_\mu T^a$ and the field strength tensors are

$$\begin{aligned} G^a_{\mu\nu} &= \partial_\mu G^a_\nu - \partial_\nu G^a_\mu + g_S f^{abc} G^b_\mu G^c_\nu \\ G_{\mu\nu} &= D_\mu G_\nu - D_\nu G_\mu = \frac{i}{g_s} \left[D_\mu, D_\nu\right] \end{aligned} \tag{2.4}$$

with the strong coupling constant $g_s$. The eight gauge fields correspond to the eight $\mathrm{SU}(3)_\mathrm{C}$ generators $T^a$. The Lie algebra

$$\left[T^a, T^b\right] = i f^{abc} T^c \tag{2.5}$$

defines the structure constants $f^{abc}$. The generators are the Gell-Mann matrices in the fundamental representation for the $\mathrm{SU}(3)_\mathrm{C}$ gauge group: $T^a_{ij} = \frac{1}{2}\lambda^a_{ij}$ .

The last term of Eq. (2.2) leads to the self-coupling of the gluon:

$$\begin{aligned}\mathcal{L}_g &= -\frac{1}{4} G^{a\mu\nu} G^a_{\mu\nu} = -\frac{1}{2} \mathrm{Tr}\left(G^{\mu\nu} G_{\mu\nu}\right) \\ &= -\frac{1}{2}\mathrm{Tr}\left(\left(\partial_\mu G_\nu - \partial_\nu G_\mu\right)^2\right) + \frac{1}{2} g_s^2 \mathrm{Tr}\left(\left[G_\mu, G_\nu\right]^2\right) + i g_s \mathrm{Tr}\left(\left(\left(\partial_\mu G_\nu - \partial_\nu G_\mu\right)\left[G^\mu, G^\nu\right]\right)^2\right)\end{aligned} \tag{2.6}$$

The second and third term represent the three-point and four-point gluon self-interaction respectively.

The quarks are colour triplets $\Psi_f \equiv \Psi_f^c$ with $c =$ red, blue, green since they transform according to the fundamental representation. For simplicity the colour indices are suppressed from now on whenever unmistakeable. The QCD Lagrangian is invariant under infinitesimal local $\mathrm{SU}(3)_\mathrm{C}$ gauge transformations described by the infinitesimal real parameters $\Theta^a(x)$. The fields transform as

$$\begin{aligned}\Psi_f(x) &\rightarrow \left[1 + i g_s \Theta^a(x) T^a\right] \Psi_f(x) \\ D^\mu \Psi_f(x) &\rightarrow \left[1 + i g_s \Theta^a(x) T^a\right] D^\mu \Psi_f(x) \\ G^a_\mu(x) &\rightarrow G^a_\mu(x) + \partial_\mu \Theta^a(x) - g_s f^{abc} \Theta^b(x) G^c_\mu(x) \ .\end{aligned} \tag{2.7}$$

Quantization of the gluon fields can be performed with the introduction of an additional gauge-fixing term $\mathcal{L}_\mathrm{gauge}$ in $\mathcal{L}_\mathrm{QCD}$. It is necessary to get rid of unphysical degrees of freedom with the help of Fadeev-Popov ghost fields causing a second additional term $\mathcal{L}_\mathrm{ghost}$ in $\mathcal{L}_\mathrm{QCD}$. In special cases for the gauge-fixing this last term $\mathcal{L}_\mathrm{ghost}$ can be zero causing a more complicated structure of the propagators.

Since QCD is treated here as a separate theory the mass terms $m\bar{\Psi}_f\Psi_f$ in Eq. (2.2) could be introduced. But these terms break the weak isospin and hypercharge symmetries and can thus not be used as mass terms in the SM.

## 2.2 Asymptotic Freedom and Confinement

The QCD coupling $\alpha_S = g_s^2/4\pi$ is not a constant, it becomes small at high energies or short distances. This scale dependence is known as asymptotic freedom [6, 7] and can be described with the beta function

$$\beta(\alpha_S) = Q^2 \frac{\partial \alpha_S}{\partial Q^2} = \frac{\partial \alpha_S}{\partial \ln Q^2} \tag{2.8}$$

where $Q$ is the energy scale where the coupling is measured. The beta function, derived from higher-order calculations, can be expanded in powers of $\alpha_S$

$$\beta(\alpha_S) = -\alpha_S^2 \left(b_0 + b_1 \alpha_S + \mathcal{O}\left(\alpha_S^2\right)\right) \tag{2.9}$$

with the leading order (LO) and next-to-leading order (NLO) coefficients

$$b_0 = \frac{33 - 2N_f}{12\pi} \quad \text{and} \quad b_1 = \frac{153 - 19N_f}{24\pi^2} \tag{2.10}$$

where $N_f$ is the number of quark flavours with masses smaller than $\sim Q$. Since the number of observed quark flavours is $N_f = 6$ the beta function is of negative sign and therefore the resulting running coupling $\alpha_S(Q^2)$ decreases with increasing energy and becomes small for short distance interactions. For the cancellation of ultra-violet divergences it is necessary to choose a specific reference scale $Q^2 = \mu^2$ during the the renormalization process. A typical choice for this scale is the mass of the $Z^0$ boson where the coupling has been measured to be $\alpha_S(M_Z^2) \approx 0.12$. To calculate the strong coupling at a certain energy scale the value of the coupling at the reference scale $\mu$ is used, from which the value at any other scale can be obtained by solving Eq. (2.8)

$$\alpha_S(Q^2) = \frac{\alpha_S(\mu^2)}{1 + b_0\alpha_S(\mu^2)\ln\left(Q^2/\mu^2\right) + \mathcal{O}\left(\alpha_S^2\right)} \ . \tag{2.11}$$

When considering the coupling at sufficiently small energies Eq. (2.11) can be rewritten as

$$\alpha_S(Q^2) = \frac{1}{b_0 \ln\left(Q^2/\Lambda^2\right)} \tag{2.12}$$

where $\Lambda \approx 200$ MeV specifies the energy scale at which the perturbative coupling nominally becomes infinite and perturbation theory therefore breaks down.

Another important property of QCD is the (colour) confinement which describes the phenomenon that quarks and gluons are not observed as free states and can therefore not propagate over macroscopic distances. If the QCD coupling is sufficiently strong the only observed states are $\mathrm{SU(3)_C}$ singlet states, namely mesons and baryons.

## 2.3 Standard Model

The combination of QCD and the theory of weak and electromagnetic interactions is the Standard Model (SM). Its underlying gauge group, see Eq. (2.1), contains the gauge groups $\mathrm{SU(3)_C}$ of QCD and $\mathrm{SU(2)_L} \times \mathrm{U(1)_Y}$ of the electroweak theory where L denotes left-handed and Y stands for hypercharge. The particle content of the SM includes the leptons and quarks

$$\begin{pmatrix}\nu_e\\ e\end{pmatrix}, \begin{pmatrix}\nu_\mu\\ \mu\end{pmatrix}, \begin{pmatrix}\nu_\tau\\ \tau\end{pmatrix} \quad \text{and} \quad \begin{pmatrix}u\\ d\end{pmatrix}, \begin{pmatrix}c\\ s\end{pmatrix}, \begin{pmatrix}t\\ b\end{pmatrix},$$

in each case arranged in three generations. The bosons for QCD are the eight gluons and for the electroweak theory the photon, $W$ and $Z$ bosons:

$$g_1,\ ...,\ g_8 \quad \text{and} \quad \gamma,\ W^+,\ W^-,\ Z^0\ .$$

Tab. 2.1 shows the representations of the first generation fermion fields in the three gauge groups. The fundamental representation of the $\mathrm{SU(2)_L}$ gauge group are the left-chiral projections of the fields, $\Psi_L = \frac{1}{2}(1-\gamma_5)\Psi$, namely the doublets $Q_L = (u_L, d_L)^T$ for the quarks and $L = (\nu_L, e_L)^T$ for the leptons. Right-chiral projections, $\Psi_R = \frac{1}{2}(1+\gamma_5)\Psi$, are

| Field $\Psi$ | $Q_{em}$ | $SU(3)_C$ | $I_s$ | $SU(2)_L$ | $I_w$ | $I_w^3$ | $Y = Q_{em} - I_w^3$ |
|---|---|---|---|---|---|---|---|
| $Q_L = \begin{pmatrix} u_L \\ d_L \end{pmatrix}$ | $\begin{matrix} 2/3 \\ -1/3 \end{matrix}$ | Triplet | 1/2 | Doublet | 1/2 | $\begin{matrix} 1/2 \\ -1/2 \end{matrix}$ | 1/6 |
| $u_R$ | 2/3 | Triplet | 1/2 | Singlet | 0 | 0 | 2/3 |
| $d_R$ | −1/3 | Triplet | 1/2 | Singlet | 0 | 0 | −1/3 |
| $L = \begin{pmatrix} \nu_{eL} \\ e_L \end{pmatrix}$ | $\begin{matrix} 0 \\ -1 \end{matrix}$ | Singlet | 0 | Doublet | 1/2 | $\begin{matrix} 1/2 \\ -1/2 \end{matrix}$ | −1/2 |
| $R = e_R$ | −1 | Singlet | 0 | Singlet | 0 | 0 | −1 |

Table 2.1: Representations of the first generation fermions with electromagnetic charge $Q_{em}$, representation in the $SU(3)_C$ gauge group, eigenvalues to the strong isospin $I_s$, representation in the $SU(2)_L$ gauge group, eigenvalues of the weak isospin $I_w$, its third component $I_w^3$ and eigenvalues of the hypercharge operator $Y = Q_{em} - I_w^3$.

singlets under $SU(2)_L$. Note that neutrinos do not appear righthanded[1] and are assumed to be massless here. The Lagrangian of the SM is

$$\begin{aligned}\mathcal{L}_{SM} =& \mathcal{L}_{boson} + \mathcal{L}_{fermion} + \mathcal{L}_{Higgs} + \mathcal{L}_{Yukawa} \\ =& -\frac{1}{4}G^{a\mu\nu}G^a_{\mu\nu} - \frac{1}{4}B^{\mu\nu}B_{\mu\nu} - \frac{1}{4}W^{i\mu\nu}W^i_{\mu\nu} \\ &+ \sum_{\Psi_{L/R}} \bar{\Psi}_{L/R} i\gamma^\mu \left(\partial_\mu - ig_s I_s \lambda^a G^a_\mu - ig'YB_\mu - igI_w\sigma^i W^i_\mu\right)\Psi_{L/R} \\ &+ \left|\left(\partial_\mu - \frac{i}{2}g'B_\mu - \frac{i}{2}g\sigma^i W^i_\mu\right)\Phi\right|^2 - \mu^2\Phi^\dagger\Phi - \lambda\left(\Phi^\dagger\Phi\right)^2 \\ &- \sum_{\Psi_{L/R}} G_e\left(\bar{\Psi}_L\Phi\Psi_R + \bar{\Psi}_R\Phi^\dagger\Psi_L\right)\end{aligned} \tag{2.13}$$

with the kinetic part of the gauge fields $\mathcal{L}_{boson}$ with the gauge field $B_\mu$ of the $U(1)_Y$ gauge group, the three gauge fields $W^i_\mu$ ($i = 1, 2, 3$) of the $SU(2)_L$ and the eight gluon fields $G^a_\mu$ ($a = 1..8$) of the $SU(3)_C$. The kinetic part of the fermions and their couplings to the gauge fields appear in $\mathcal{L}_{fermion}$ with the dimensionless coupling constants $g$ and $g'$. The coupling to the $U(1)_Y$ gauge field goes proportional with the according quantum number, the hypercharge $Y$, and analogously for the coupling to $SU(2)_L$ and $SU(3)_C$ gauge fields. The fermion fields and their eigenvalues to the corresponding operators for the first generation can be found in Tab. 2.1. The kinetic part of the Higgs doublet, its coupling to the gauge fields and its potential is $\mathcal{L}_{Higgs}$. The last term, $\mathcal{L}_{Yukawa}$, contains the coupling of the fermions to the Higgs doublet, the Yukawa coupling, with a dimensionless coupling constant $G_e$.

[1] The Goldhaber experiment (1957) showed that neutrinos only appear lefthanded in nature.

# 3. The Experiment

Since part of this thesis deals with the analysis of data the collider and the experiment the data was taken from are shortly described in the following sections.

## 3.1 The LEP Collider

The Large Electron Positron Collider (LEP) with its 27-kilometer circumference was the largest electron-positron accelerator ever built. In the first phase of the LEP operation (1989-1995), called LEP1, the center of mass energy was chosen to be at the mass of the $Z^0$ boson, around 91 GeV. In this way around 7 million of events producing $Z^0$ bosons were accumulated for high precision measurements. Therewith the $Z^0$ boson was discovered at CERN in 1983. In 1995 LEP was upgraded for the second operation phase, LEP2, where the center of mass energy was increased up to 209 GeV. During this second phase (1996-2000) the colliding energy was high enough to produce $W^+W^-$ boson pairs and to search for possible new particles or physical effects.

The detectors at LEP provided a detailed study of the SM, especially of the electroweak interaction, and proved that there are exactly three generations of particles of matter. After closing LEP in the end of 2000 the Large Hadron Collider (LHC) was built in the same tunnel.

## 3.2 The OPAL Experiment

The OPAL detector (Omni-Purpose Apparatus at LEP) was one of four enormous detectors observing the collisions at LEP. The data taking started in August 1989 and finally ended in November 2000.

The detector components, as shown in Fig. 3.1, were arranged around the beam pipe, in a layered structure like that of an onion. The following information about the components are taken from Ref. [8] where a more detailed description of the detector parts can be found.

The tracking system of the OPAL detector consisted of a silicon microvertex detector, a vertex detector, a jet chamber, and so-called Z-chambers (from the beam pipe out).

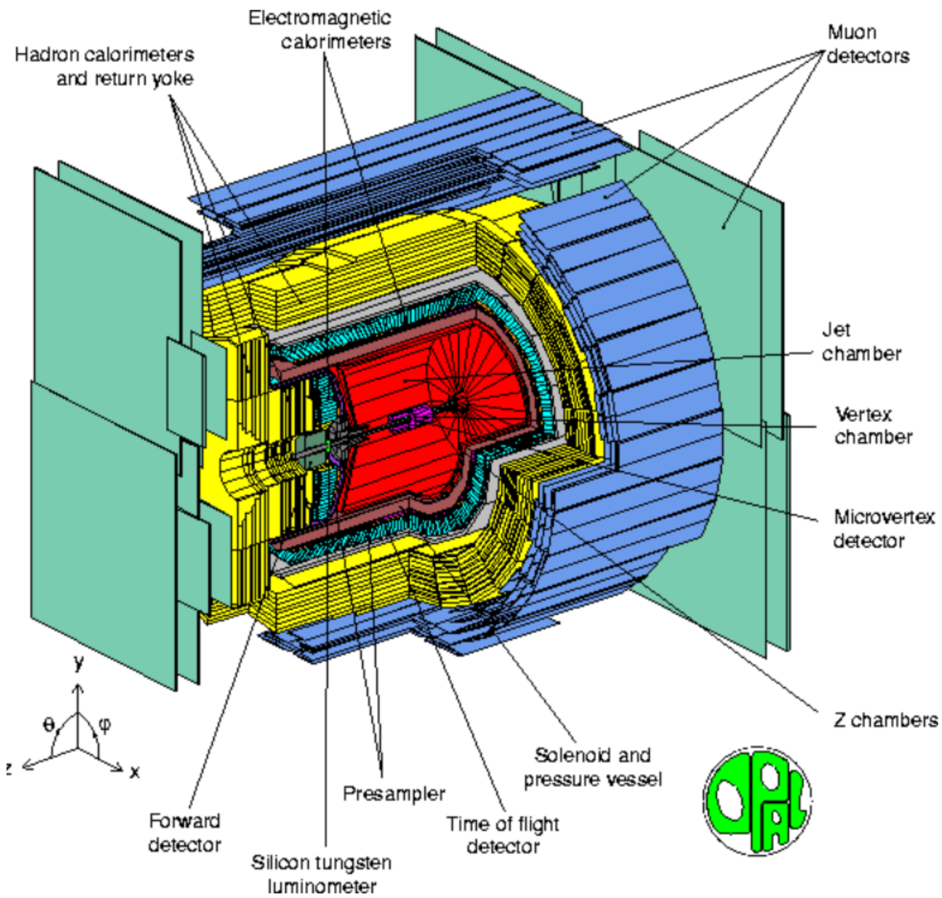


Figure 3.1: Schematic picture the OPAL detector which was about 12 m long, 12m high and 12m wide. Its different components such as vertex chambers or muon detectors are shown. Taken from Ref. [8].

Decay vertices of short-lived particles were detected by the silicon microvertex detector and the vertex chamber. They also worked together to improve the momentum resolution. The fact that different particles produce different amounts of ionization and get discriminatively far diffracted in magnetic fields was used by the central jet chamber to identify the particles. Tracks in the plane perpendicular to the beam axis were well identified by the combination of these chambers. The last chambers, the Z-chambers located at the outside edge of the jet chamber, led to precise measurements of the perpendicular coordinates of the tracks.

The calorimeter system of OPAL contained the electromagnetic calorimeter in order to detect electrons and photons and the hadron calorimeter for identifying hadrons. The third part of this system was the forward calorimeter placed close to the beam at the two ends of the detector in order to detect forward flying particles. At the end caps muons were identified by the muon detectors.

# 4. Physics of Event Generators

A highly non-trivial task is to understand the final states at high-energy collisions containing a large number of particles with momenta ranging over many orders of magnitude. Due to factorization it is possible to treat the different processes separately: First a subprocess at the highest energy scale of the event can be computed in perturbation theory with its matrix element. During the parton shower additional emissions occur and the scale evolves down to low scales at which perturbation theory breaks down. Now the hadronization forms hadrons out of the partons and finally the unstable hadrons decay into the observed particles. All these steps are very well suited to computer simulations using Monte Carlo techniques. The aim of this chapter is to give a basic overview of the physics behind these processes.

## 4.1 Hard Processes

The first step to be calculated is the hard subprocess. The differential cross section for an observable $\mathcal{O}$ taking all orders of the strong coupling $\alpha_S$ into account is

$$\frac{\mathrm{d}\sigma_n}{\mathrm{d}\mathcal{O}} = F \sum_{k=0}^{\infty} \int \mathrm{d}\Phi_{n+k} \left| \sum_{l=0}^{\infty} \mathcal{M}_{n+k}^{(l)} \right|^2 \delta\left(\mathcal{O} - \mathcal{O}(\Phi_{n+k})\right) \tag{4.1}$$

with flux factor $F$. The final state contains $n$ plus $k$ additional particles and $\Phi_{n(+k)}$ denotes the according phase space. The first sum runs over all additional external legs $k$ and the second over all additional loops $l$. Therefore $M_{n+k}^{(l)}$ is the amplitude for a system containing $n$ particles plus $k$ external legs and $l$ loops. $M_n^{(0)}$ is the LO contribution for producing the $n$-particle final state and higher terms correspond to real and virtual corrections. Considering perturbative QCD, the order of the perturbative series can be obtained as follows [9]:

$$\begin{array}{lll}
k = 0,\, l = 0 & \Longrightarrow & \text{LO for the production of } n \text{ particles} \\
k = m,\, l = 0 & \Longrightarrow & \text{LO for } n \text{ particles plus } m \text{ additional jets} \\
k + l \leq m & \Longrightarrow & \text{N}^m\text{LO for } n \text{ particles (includes N}^{m-1}\text{LO for } n+1 \text{ jet,} \\
 & & \text{N}^{m-2}\text{LO for } n+2 \text{ jet, ... LO for } n+m \text{ jets)}
\end{array}$$

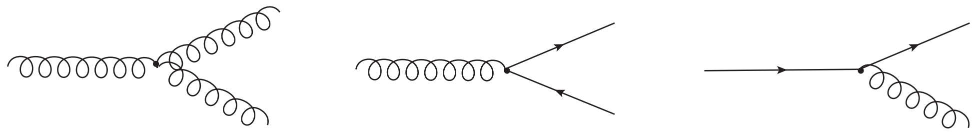

Figure 4.1: Relevant splittings in the QCD parton shower: $g \to gg$, $g \to q\bar{q}$ and $q \to qg$.

For example the NLO cross section for the production of only one particle, meaning $k + l \leq 1$ and $n = 1$, is

$$\begin{aligned}\sigma_1^{\mathrm{NLO}} &= F \int \mathrm{d}\Phi_1 \left|\mathcal{M}_1^{(0)}\right|^2 + F \int \mathrm{d}\Phi_2 \left|\mathcal{M}_2^{(0)}\right|^2 + F \int \mathrm{d}\Phi_1 2\mathrm{Re}\left[\mathcal{M}_1^{(1)}\mathcal{M}_1^{(0)*}\right] \\ &= \sigma_0^{(0)} \qquad\qquad + \sigma_1^{(0)} \qquad\qquad + \sigma_0^{(1)} \end{aligned} \tag{4.2}$$

with the Born cross section $\sigma_0^{(0)}$, real correction $M_2^{(0)}$ and virtual correction $M_1^{(1)}$. Note that the term $\sigma_1^{(1)} = F \int \mathrm{d}\Phi_1 \left|\mathcal{M}_1^{(1)}\right|^2$ does not appear since this term contains higher orders of the strong coupling constant, and therefore belongs to the NNLO contribution. Integrating over the whole phase space $\mathrm{d}\Phi_{n+k}$ in Eq. (4.1) would lead to divergences in the real and virtual corrections. By adding the contributions these singularities cancel each other order by order.

## 4.2 Parton Shower

The hard processes are usually generated according to lowest-order matrix elements. To get higher accuracy it is possible to include higher orders of the strong coupling constant $\alpha_S$ in perturbation theory. But these corrections get more difficult to calculate with increasing order of $\alpha_S$ and in some cases the cross section for certain phase space regions of the final state is enhanced in higher orders [5]. Therefore a shower algorithm is used to resum the effect of higher orders. This approach is typically formulated as an evolution in momentum transfer down from the higher scales associated with the hard process to low scales [10].

QCD matrix elements have enhancements for two kinematic configurations:

1. The emission of a soft gluon ($E \to 0,$ soft singularity).
2. The splitting into two collinear partons $i$ and $j$ ($\theta_{ij} \to 0,$ collinear singularity).

The cross section $\sigma_{n+1}$ for a hard configuration accompanied by an additional emission can be calculated from the cross section $\sigma_n$ of the hard process due to the fact that gauge theory amplitudes factorize in the soft and collinear limit. This is used in parton shower algorithms to generate emissions iteratively.

### 4.2.1 Parton Branching in the Collinear Limit

Consider the splitting of an outgoing parton $a$ into two partons $b$ and $c$: $a \to bc$. The relevant branchings in QCD, namely $g \to gg$, $g \to q\bar{q}$ and $q \to qg$, are shown in Fig. 4.1. After the splitting parton $b$ carries the energy fraction $z$ of the mother parton $a$, $E_b = zE_a$, and due to energy conservation the energy of parton $c$ is $E_c = (1 - z)E_a$.

| Process $a \to bc$ | Splitting Function $P_{a\to bc}(z)$ |
|---|---|
| $g \to gg$ | $P_{g\to gg} = N_C \left[\frac{z}{1-z} + \frac{1-z}{z} + z(1-z)\right]$ |
| $g \to q\bar{q}$ | $P_{g\to q\bar{q}} = T_R\,[z^2 + (1-z)^2]$ |
| $q \to qg$ | $P_{q\to qg} = C_F \frac{1+z^2}{1-z}$ |
| $q \to gq$ | $P_{q\to gq} = C_F \frac{1+(1-z)^2}{z}$ |

Table 4.1: The Altarelli-Parisi splitting functions $P_{a\to bc}(z)$ for the relevant splitting processes $a \to bc$ in QCD. Equations taken from Ref. [10]. Recap that parton $b$ carries the momentum fraction $z$ and hence parton $c$ carries $z-1$. The colour factors are $T_R = \frac{1}{2}$, $N_C = C_A = 3$ and $C_F = \frac{4}{3}$.

As mentioned above, the amplitude factorizes for small opening angles $\theta_{bc}$ between the partons $b$ and $c$, hence in the collinear limit, and can therefore be written as

$$|\mathcal{M}_{n+1}(..,b,c,...)|^2 \quad \xrightarrow{b||c} \quad 4\pi\alpha_S\,\frac{P_{a\to bc}(z)}{s_{bc}}\,|\mathcal{M}_n(..,b+c,...)|^2 \tag{4.3}$$

with the Altarelli-Parisi splitting kernels $P_{a\to bc}(z)$, which contain a colour factor $\mathcal{C}_{a\to bc}$ for the considered branching $a \to bc$, and the universal singularity containing the invariants $s_{bc}$ which are defined as

$$s_{bc} \equiv 2p_b \cdot p_c = (p_b + p_c)^2 - m_b^2 - m_c^2 = 2E_bE_c(1-\cos\theta_{bc})\ . \tag{4.4}$$

In the massless limit $s_{bc}$ is equal to the virtuality of parton $a$,

$$s_{bc} = (p_b + p_c)^2 = p_a^2 \equiv Q^2\ . \tag{4.5}$$

In the collinear limit, $s_{bc} \to 0$, the propagator of the parent $a$, $1/Q^2$, goes on shell. Thus the singularity of the propagator is the origin of the collinear singularity.

The relation between the cross section for the hard process $\sigma_n$ and the cross section for the same process accompanied by an additional parton with momentum fraction $z$ in the collinear limit is given by

$$\mathrm{d}\sigma_{n+1} \quad \xrightarrow{b||c} \quad \mathrm{d}\sigma_n \sum_{b,c} \frac{\alpha_S}{2\pi}\frac{\mathrm{d}Q^2}{Q^2}\mathrm{d}z P_{a\to bc}(z) \tag{4.6}$$

with the appropriate splitting function $P_{a\to bc}(z)$ listed in Tab. 4.1 for the relevant splittings. Instead of the virtuality $Q^2$ of the parent parton $a$ it is also possible to use any other variable proportional to $\theta_{bc}^2$, for example the transverse momentum of parton $b$ with respect to the parent parton's direction, $k_\perp^2 = z^2(1-z)^2E_a^2\theta_{bc}^2$, since

$$\frac{\mathrm{d}k_\perp^2}{k_\perp^2} = \frac{\mathrm{d}\theta_{bc}^2}{\theta_{bc}^2} = \frac{\mathrm{d}p_a^2}{p_a^2} = \frac{\mathrm{d}Q^2}{Q^2} \equiv \mathrm{d}t = \mathrm{d}\ln Q^2\ . \tag{4.7}$$

Each variable gives the same result in the collinear limit, but different extrapolations away from it.

### 4.2.2 Coherent Branching and Angular Ordering

Besides the collinear singularities there are enhancements associated with soft gluon emission for any emission angle and any velocity of the emitting parton [5]. Consider a soft gluon with momentum $p_j$ emitted by a colour-connected pair of partons with momenta $p_I$ and $p_K$. Since gauge theory amplitudes factorize in the soft limit, the matrix element squared can be written as

$$|\mathcal{M}_{n+1}(..,i,j,k,...)|^2 \quad \overset{E_j\to 0}{\longrightarrow} \quad 4\pi\alpha_S\,\mathcal{C}_{IK\to ijk}\left(\frac{2s_{ik}}{s_{ij}s_{jk}} - \frac{m_i^2}{s_{ij}^2} - \frac{m_j^2}{s_{jk}^2}\right)|\mathcal{M}_n(..,I,K,...)|^2 \tag{4.8}$$

with the universal soft eikonal factor (term in parenthesis), colour factor $\mathcal{C}_{IK\to ijk}$ for the specific splitting $IK \to ijk$ and the invariants $s_{ab}$ as defined in Eq. (4.5). In the limit where the emitted gluon is soft, the propagators of both partons $i$ and $j$ go on shell. Thus the soft singularity $2s_{ik}/(s_{ij}s_{jk})$ is generated by the singularities of the propagators of both parent partons.

Following Eq. (4.8) the cross section for the soft emission contains the dipole radiation term

$$W_{IK}(j) \equiv \frac{1}{2}E_j^2\left(\frac{2s_{ik}}{s_{ij}s_{jk}} - \frac{m_i^2}{s_{ij}^2} - \frac{m_j^2}{s_{jk}^2}\right) \tag{4.9}$$

with gluon energy $E_j$. In the massless limit ($\beta_{I,K} = v_{I,K}/c \to 1$) the radiation function in Eq. (4.9) has enhancements for either $\theta_{ij} \to 0$ or $\theta_{jk} \to 0$. Thus it can be written as

$$\begin{aligned} W_{IK}(j) &\equiv W_{IK}^{(I)}(j) + W_{IK}^{(K)}(j) \\ &= \frac{1}{2}E_j^2\left(\frac{1}{s_{ij}} - \frac{m_i^2}{s_{ij}^2} + \frac{s_{ik}-s_{ij}}{s_{ij}s_{jk}}\right) + \frac{1}{2}E_j^2\left(\frac{1}{s_{jk}} - \frac{m_j^2}{s_{jk}^2} + \frac{s_{ik}-s_{jk}}{s_{ij}s_{jk}}\right) \end{aligned} \tag{4.10}$$

where $W_{IK}^{(I)}(j)$ only contains the singularity for the gluon being collinear to parton $i$ and is finite if the gluon and parton $k$ are collinear. Hence it may naturally be associated with emission off parton $i$. The radiation function $W_{IK}^{(I)}(j)$ is everywhere positive-definite for angles $\theta_{ij} < \theta_{IK}$, whereas the function goes to negative values for $\theta_{ij} > \theta_{IK}$ [11]. Azimuthal averaging gives

$$\langle W_{IK}^{(I)}\rangle_{\phi_i} = H_{IK}^{(I)}(\theta_{ij})\frac{E_I E_j \beta_I}{s_{ij}} \quad \Rightarrow \quad \Theta(\theta_{IK}-\theta_{ij})\frac{1}{1-\cos\theta_{ij}} \quad \text{for} \quad \beta_{I,K} \to 1\ , \tag{4.11}$$

where $H_{IK}^{(I)}$ is a function depending on $\theta_{ij}$ and $\theta_{IK}$. After azimuthal averaging the contribution from $W_{IK}^{(I)}$ is limited to a cone around parton $I$ with opening angle $2\theta_{IK}$ in the massless limit $\beta_{I,K} \to 1$. Similarly, the contribution from $W_{IK}^{(K)}$ is limited to a cone around parton $K$ with opening angle $2\theta_{IK}$.

For massive emitting partons $I$ and $K$ the Heaviside step function of the radiation function $H_{IK}^{(I)}(\theta_{ij})$ is softened. The emission at small opening angles is suppressed since the masses shield the collinear enhancement. Hence there is a so-called dead cone for $\theta_{ij} < m_I/E_I$, namely for emissions near to the direction of the massive particle $I$.

By using the emission angle as the shower ordering variable the coherence property of QCD can be described. Fig. 4.2 shows the QCD colour coherence for soft gluon emissions

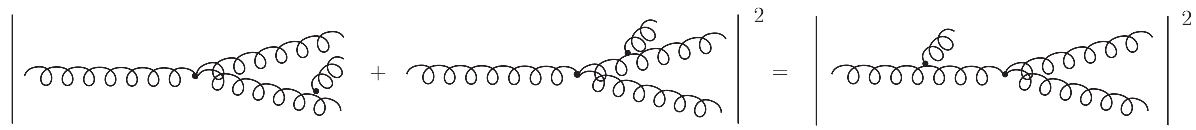

Figure 4.2: Illustration of QCD coherence, the destructive interference effects between colour-connected partons, in this case gluons.

from a pair of colour-connected gluons. The two Feynman diagrams where the additional gluon is attached to any of the external gluons interfere destructivly. Hence the coherent sum of these diagrams is equal to the emission off a single gluon with the total momentum and colour of the two external gluons. This is, as if it were emitted before the smaller-angle harder gluon. The angular ordering property of soft emission is an example of a coherence effect common to all gauge theories [5]. In Quantum Electrodynamics (QED) soft wide-angle bremsstrahlung from $e^-e^+$ pairs is suppressed, which is called Chudakov effect. The coherent parton branching formalism, whose basis is the angular ordering, can be used to calculate the soft gluon enhancements to all orders.

The cross section of a hard process with a $n$-particle final state, accompanied by one additional radiation can be written in terms of the radiation function,

$$\mathrm{d}\sigma_{n+1} \overset{E_j\to 0}{\longrightarrow} -\mathrm{d}\sigma_n \frac{\alpha_S}{2\pi}\sum_{i\neq k}\mathcal{C}_i\cdot\mathcal{C}_k\left\{\Theta(\theta_{IK}-\theta_{ij})W_{IK}^{(I)}(\phi_i)\frac{\mathrm{d}\phi_i}{2\pi}\mathrm{d}s_{ij}+(i\leftrightarrow k)\right\}\frac{\mathrm{d}E_j}{E_j} \tag{4.12}$$

for massless particles with colour factors $\mathcal{C}_i$ and $\mathcal{C}_j$.

### 4.2.3 The Colour Dipole Model

The basis of this model is the neglection of $1/N_C$ contributions in QCD diagrams in the limit of large number of colours $N_C$. Therewith the colour structure of an arbitrarily complicated parton system can be decomposed as a colour flow. The colour flow is represented by a set of colour lines, each connecting two partons. In the limit of soft gluons and large-$N_C$ the colour lines emit independently. For each configuration the probabilities of the possible colour flows can be calculated and one specific colour flow can be chosen since in the large-$N_C$ limit the contribution of the overlap of different colour flows is neglected. Colour dipoles are formed by colour-connected parton pairs as they can appear after the hard process or during the parton shower. The dipoles are characterized by their colour line and each of these lines emits independently.

Naturally dipole showers are ordered in transverse momentum since the dipole approximation is the limit in which the scales involved in the production of the colour lines are much larger than the transverse momentum of the emitted gluon. Transverse means here relative to the axis defined by the colour line from which the gluon is emitted [10].

Beginning with, for example, a quark-antiquark pair going out of the hard process, one colour dipole is formed out of the $q\bar{q}$ pair and one colour flow is chosen. The following dipole evolution makes use of this unique initial condition. After emissions off the dipole their number increases as the number of colour lines increases. Thereby each colour line connecting a pair of partons effectively forms a colour-anticolour dipole. Emissions with finite transverse momentum lead to recoils, which, if experienced by a gluon, may lead to effects on the neighbouring dipoles since gluons carry two colour lines. The emission with the highest transverse momentum appears first and its transverse momentum gives the upper limit for the following evolution of the dipoles.

| Process $IK \to ijk$ | $A_{IK\to ijk}(y_{ij}, y_{jk}; s_{IK}, \alpha_S)$ |
|---|---|
| $q\bar{q} \to qg\bar{q}$ | $A_{q\bar{q}\to qg\bar{q}} = 4\pi\alpha_S \frac{2C_F}{s_{IK}} \left( \frac{2}{y_{ij}y_{jk}} - \frac{2}{y_{ij}} - \frac{2}{y_{jk}} + \frac{y_{ij}}{y_{jk}} + \frac{y_{jk}}{y_{ij}} \right)$ |
| $qg \to qgg$ | $A_{qg\to qgg} = 4\pi\alpha_S \frac{2C_F}{s_{IK}} \left( \frac{2}{y_{ij}y_{jk}} - \frac{2}{y_{ij}} - \frac{2}{y_{jk}} + \frac{y_{ij}}{y_{jk}} + \frac{y_{jk}}{y_{ij}} - \frac{y_{ij}^2}{y_{jk}} \right)$ |
| $gg \to ggg$ | $A_{gg\to ggg} = 4\pi\alpha_S \frac{N_C}{s_{IK}} \left( \frac{2}{y_{ij}y_{jk}} - \frac{2}{y_{ij}} - \frac{2}{y_{jk}} + \frac{y_{ij}}{y_{jk}} + \frac{y_{jk}}{y_{ij}} - \frac{y_{ij}^2}{y_{jk}} - \frac{y_{jk}^2}{y_{ij}} \right)$ |
| $qg \to q\bar{q}'q'$ | $A_{qg\to q\bar{q}'q'} = 4\pi\alpha_S \frac{1}{s_{IK}} \left( \frac{1}{2y_{jk}} - \frac{y_{ij}}{y_{jk}} + \frac{y_{ij}^2}{y_{jk}} \right)$ |
| $gg \to gq'\bar{q}'$ | $A_{gg\to gq'\bar{q}'} = A_{qg\to q\bar{q}'q'}$ |

Table 4.2: The Gehrmann-Gehrmann-de-Ridder-Glover antenna functions $A_{IK\to ijk}(y_{ij}, y_{jk}; s_{IK}, \alpha_S)$, with finite terms subtracted, for different processes $IK \to ijk$. Taken from Ref. [12].

### 4.2.4 Antenna Functions

As shown in Eqs. (4.3) and (4.8) the amplitude factorizes in the collinear and soft limit. The different approaches for the shower algorithm combine the two limits into one universal set of functions to achieve a correct behaviour for both limits. One of these approaches uses antenna functions. For example the antenna function for the gluon emission from a colour-connected $q\bar{q}$ pair can be derived from the matrix elements squared for the process $Z \to q\bar{q} \to qg\bar{q}$ [9],

$$\frac{|\mathcal{M}(Z \to q_i g_j \bar{q}_k)|^2}{|\mathcal{M}(Z \to q_I \bar{q}_K)|^2} = 4\pi\alpha_S 2C_F \Bigg[ \underbrace{\frac{2s_{ik}}{s_{ij}s_{jk}}}_{\text{eikonal}} + \frac{1}{s_{IK}} \underbrace{\left( \frac{s_{jk}}{s_{ik}} + \frac{s_{ik}}{s_{jk}} \right)}_{\text{collinear}} \Bigg] . \tag{4.13}$$

This expression contains the same eikonal factor as in Eq. (4.8) and holds only for massless partons. However, massive generalizations do exist. In general a process-dependent additive finite factor occurs, which is zero for the process in Eq. (4.13). Since the singularity structure is universal, the antenna function for a splitting of type $IK \to ijk$ moving the system of $n$ to $n+1$ partons can in general be written as

$$|\mathcal{M}_{n+1}|^2 = \underbrace{4\pi\alpha_S\, \mathcal{C}_{IK\to ijk} \left( \frac{2s_{ik}}{s_{ij}s_{jk}} + \frac{1}{s_{IK}} \left( \frac{s_{jk}}{s_{ij}} + \frac{s_{ij}}{s_{jk}} \right) - \frac{s_{ij}^2}{s_{jk}} - \frac{s_{jk}^2}{s_{ij}} + \text{finite} \right)}_{\text{Antenna Function}} |\mathcal{M}_n|^2 . \tag{4.14}$$

Since this equation is process-independent the cross section $\mathrm{d}\sigma_{n+1}$ can approximately be expressed in terms of $\mathrm{d}\sigma_n$ and the antenna function,

$$\mathrm{d}\sigma_{n+1} \quad \longrightarrow \quad \mathrm{d}\sigma_n \sum_{i,j,k} \frac{\mathrm{d}y_{ik}\mathrm{d}y_{kj}}{16\pi^2} A_{IK\to ijk}(y_{ij}, y_{jk}; s_{IK}, \alpha_S) , \tag{4.15}$$

with the scaled branching invariants $y_{ij} = s_{ij}/s$, where $s = s_{IK} = s_{ijk}$. The most general form of the antenna function for the massless splitting $IK \to ijk$ is given by a double Laurent series in the two branching invariants,

$$a_{IK\to ijk}(y_{ij}, y_{jk}; s_{IK}, \alpha_S) = \frac{1}{s_{IK}} \sum_{\alpha,\beta=-1}^{\infty} C_{\alpha,\beta} \left(y_{ij}\right)^{\alpha} \left(y_{jk}\right)^{\beta} \ , \tag{4.16}$$

$$\text{with} \qquad A_{IK\to ijk}(y_{ij}, y_{jk}; s_{IK}, \alpha_S) = 4\pi\alpha_S \, \mathcal{C} \, a_{IK\to ijk}(y_{ik}, y_{jk}; s_{IK}) \ . \tag{4.17}$$

The most singular term contains the double (soft) singularity (the "double log" term) and its strength is controlled via the coefficient $C_{-1,-1}$. The single (collinear) singularities (the "single log" terms) appear with the coefficients $C_{-1,\beta\geq 0}$ and $C_{\alpha\geq 0,-1}$. These "leading log" terms are universal, as mentioned above, and the coefficients $C_{\alpha\geq 0,\beta\geq 0}$ are arbitrary. Different sets of antenna functions distinguishable by the values of the coefficients $C_{\alpha,\beta}$ exist, [12].
The Gehrmann-Gehrmann-de-Ridder-Glover antenna functions for different processes $IK \to ijk$ without the finite part are listed in Tab. 4.2.

### 4.2.5 Sudakov Form Factors and the Shower Chain

The so-called Sudakov form factor defines the probability that there is no resolvable splitting or emission between two scales $t_{\text{in}}$ and $t_{\text{end}}$ ($t_{\text{in}} > t_{\text{end}}$),

$$\Delta(t_{\text{in}}, t_{\text{end}}) = \exp\left\{ - \int_{t_{\text{end}}}^{t_{\text{in}}} \mathrm{d}t P(t) \right\} \ , \tag{4.18}$$

where $P(t)$ is the total parton evolution or splitting probability density. Considering a specific system of $n$ partons with phase space $\Phi_n$, the Sudakov form factor is

$$\Delta(t_n, t_{\text{end}}) = \exp\left\{ - \int_{t_{\text{end}}}^{t_n} \mathrm{d}t_{n+1} \sum_r \int \frac{\mathrm{d}\Phi^r_{n+1}}{\mathrm{d}\Phi_n} \delta(t_{n+1} - t^r_{n+1}) P(n \to n+1) \right\} \tag{4.19}$$

with the branching phase space $\mathrm{d}\Phi^r_{n+1}/\mathrm{d}\Phi_n$. The sum runs over all possible branchings $r$ that transfers the system with $n$ partons to a system with $n+1$ partons. To prevent double-counting the scale of the parton produced in the next branching has to be smaller than the one generated before, and so on, which is imposed by the integral over $t_{n+1}$ together with the $\delta$-function.

Since $\Delta$ describes the probability that there is no branching between two scales, $1 - \Delta$ is the integrated branching probability $\mathcal{P}_{\text{branch}}$ and its rate of change gives the branching probability

$$\begin{aligned}
\frac{\mathrm{d}\mathcal{P}_{\text{branch}}(t_n, t_{n+1})}{\mathrm{d}t_{n+1}} &= \frac{\mathrm{d}}{\mathrm{d}t_{n+1}} \left(1 - \Delta(t_n, t_{n+1})\right) \\
&= \sum_r \int \frac{\mathrm{d}\Phi^r_{n+1}}{\mathrm{d}\Phi_n} \delta(t_{n+1} - t^r_{n+1}) P(n \to n+1) \Delta(t_n, t_{n+1}) \ . 
\end{aligned} \tag{4.20}$$

Following Eq. (4.1) the Born cross section for a hard process with $n$ outgoing particles, differential in an observable $\mathcal{O}$, is

$$\frac{\mathrm{d}\sigma^{(0)}_n}{\mathrm{d}\mathcal{O}} = \int \mathrm{d}\Phi_n \left|\mathcal{M}^{(0)}_n\right|^2 \delta\left(\mathcal{O} - \mathcal{O}(\Phi_n)\right) \ . \tag{4.21}$$

To take the parton shower into account an evolution operator $\mathcal{S}$ acting on the final state before evaluating the observable is introduced:

$$\frac{\mathrm{d}\sigma_n}{\mathrm{d}\mathcal{O}} = \int \mathrm{d}\Phi_n \left|\mathcal{M}_n^{(0)}\right|^2 \mathcal{S}(\Phi_n, \mathcal{O}) \ . \tag{4.22}$$

This evolution operator can be computed iteratively for an event between the two scales $t_1 > t_2$ via

$$\begin{aligned}\mathcal{S}(\Phi_n, t_1, t_2, \mathcal{O}) = & \underbrace{\Delta(t_1, t_2)\delta\left(\mathcal{O} - \mathcal{O}(\Phi_n)\right)}_{n+0 \text{ exclusive above } t_2} \\ & + \underbrace{\sum_r \int \frac{\mathrm{d}\Phi^r_{n+1}}{\mathrm{d}\Phi_n} \delta(t_{n+1} - t^r_{n+1}) P(n \to n+1) \Delta(t_1, t_{n+1}) \mathcal{S}(\Phi_{n+1}, t_{n+1}, t_2, \mathcal{O})}_{n+1 \text{ inclusive above } t_2}\end{aligned} \tag{4.23}$$

with the Sudakov form factors $\Delta(t_1, t_2)$. The first term of the right side of Eq. (4.23) is the probability that no branching occurs during the evolution from $t_1$ down to $t_2$. The second part contains the probability that an emission occurs at the scale $t_{n+1}$, for which $t_1 > t_{n+1} > t_2$ holds. Then the system is evolved further from this scale $t_{n+1}$ down to $t_2$ via $\mathcal{S}(\Phi_n, t_{n+1}, t_2, \mathcal{O})$. For this expression Eq. (4.23) can be inserted again leading to an iterative algorithm for the parton shower.

## 4.3 Hadronization Models

Due to confinement partons are never observed as physically free states in nature. Thus an important step in the generation of a whole event is hadronization. It models the conversion from colour-charged particles into bound states, the hadrons. Since this happens at low momentum transfer and long distances, respectively, perturbation theory is not valid anymore and non-perturbative effects become important. Fortunately there are models which allow to shape the hadronization process. The three most important ones [5, 11] are shortly described in the following sections.

### 4.3.1 Independent Fragmentation

The oldest and simplest hadronization model is the independent fragmentation, which supposes, as the name implies, that each parton fragments independently. In this approach, originally formulated by Field and Feynman [13, 14], the occurring gluons are split into quark-antiquark pairs. Quark-antiquark or diquark-antidiquark pairs are created out of the vacuum with a Gaussian distributed transverse momentum. These created particles combine with the fragmenting quark in order to form hadrons. After each step a quark or diquark respectively with less energy is left over. The process stops until the remaining energy falls below some cut-off which leads to the great weakness of the model. The termination of the hadronization leads to a colour charged quark in each jet. Due to colour confinement these quarks have to be removed. Another disadvantage is the violation of momentum conservation due to the assumption that the quarks are on massshell. Beside the momentum the residual colour and flavour of the left over parton has to be corrected as well. Despite these simple basic assumption the independent fragmentation is quite successful in describing the broad features of two-jet and three-jet final states in $e^+e^-$ annihilation at moderate energies [5].

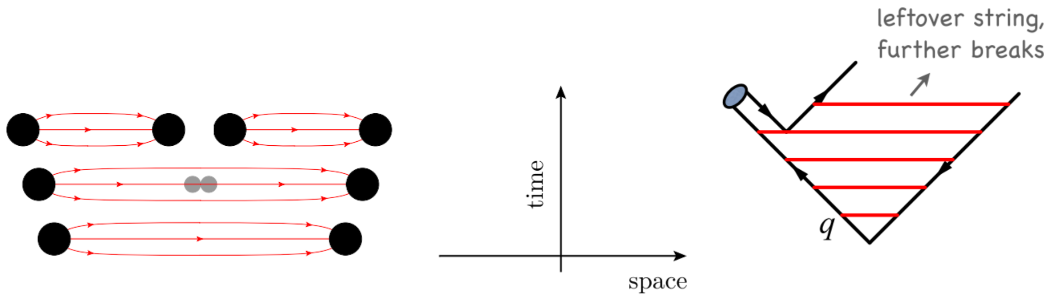


Figure 4.3: The left sketch shows a string which breaks due to the quark antiquark pair produced in the string. On the right side the fragmentation of a string is shown. Taken from Ref. [9].

### 4.3.2 String Model

Among several other hadronization models based on strings the so-called Lund model [15, 16] is most widely used. The model will be illustrated on the basis of a quark-antiquark event, as shown in Fig. 4.4. The two quarks build a colour dipole field whose energy increases linearly with the distance of the charges due to the potential $V(r) = \kappa r$ with tension (energy per unit length) $\kappa$. Thereby the short-distance Coulomb term is neglected. As the partons move apart, a colour flux tube is being stretched between the quark and the antiquark and the kinetic energy of the partons is converted to potential energy stored in the growing string. Fluctuations of quark-antiquark pairs inside the field of the string provide the formation of the observed hadrons by absorbing energy from the string and break it into two separate colour-singlet pieces, see left side of Fig. 4.3. In this picture gluons build “kinks” on the strings, which leads to the absorbance of very soft gluons. Due to the gluons modifications of the fragmentation model have to be included.

String fragmentation is carried out iteratively from both string ends inwards to the center of the string. Thereby the fragmentation off the two different sides is alternated randomly, see right side of Fig. 4.3, where a single on-shell hadron can be split off in each step.

### 4.3.3 Cluster Model

Cluster-like structures have a long history in models of non-perturbative physics [11]. They are best know from the cluster hadronization model in Herwig, implemented by Webber [17]. After the splitting of gluons into quark-antiquark pairs quark lines with the same colour index build clusters due to colour preconfinement, as illustrated on the right hand side of Fig. 4.4. The mass distributions of the clusters are thereby independent of the energy scale of the hard process. They have a maximum at low masses of some GeV and fall fast for higher masses. If the mass of a cluster is too high, it is first decayed into lighter clusters. Then the resulting clusters are decayed into hadrons, where two-body decays are assumed for the majority of clusters. For the decay into hadrons or lighter cluster, a quark-antiquark pair created out of the vacuum.

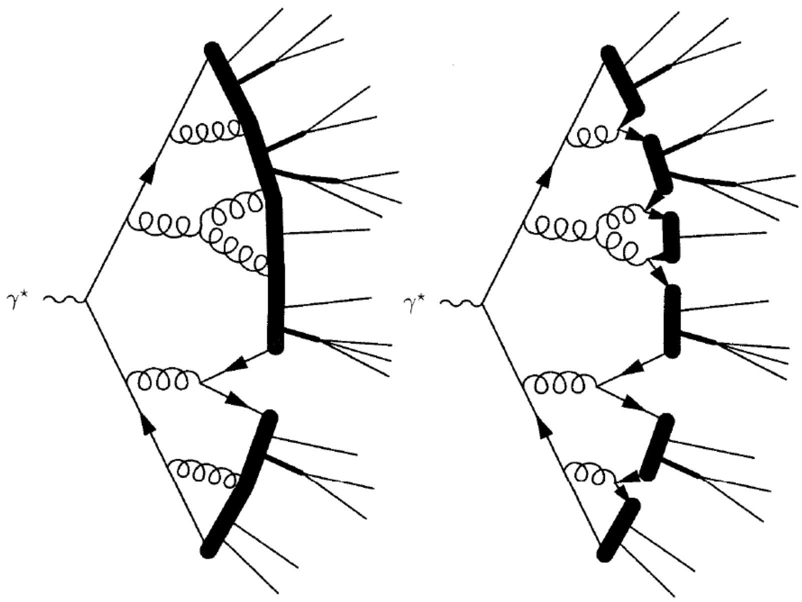


Figure 4.4: The hadronization of a $\gamma^* \to q\bar{q}$ event into hadrons, as pictured in the string model, left, and cluster model, right. During the parton shower a perturbative $g \to q\bar{q}$ vertex occurs and causes two strings to form. The gluons build "kinks" on the two strings. In the cluster model the final state gluons are split into $q\bar{q}$ pairs. Taken from Ref. [11].

# 5. Monte Carlo Event Generators and Analysis Tools

Herwig++ and Pythia8 are multi-purpose Monte Carlo event generators for the simulation of lepton-lepton, lepton-hadron and hadron-hadron collisions at high energies. The simulation contains all parts of the scattering including the hard subprocess, based on perturbation theory, a shower algorithm, hadronization and decays of unstable particles. Despite both are based on perturbation theory, the hard process and the shower algorithm are examined in two complementary approximations. The matrix-element based generation of the hard process is described in Sec. 5.1 whereas Sec. 5.2 deals with the implementation of the resummation of emissions to all orders. The hadronization models of Herwig++ and Pythia8 are described in Sec. 5.4. At last the tools for generator validation and tuning are presented.

## 5.1 Hard Process

The first step in an event generator is the interaction of the incoming particles with high transverse momentum via matrix elements. Most of these matrix elements are implemented at LO but NLO corrections are available for some processes. If the particles of the beams are hadrons the flavour and momenta of the colliding partons are sampled according to parton distribution functions. An important initial condition for the parton showers is the colour flow of the external partons. The user specifies the subprocesses which will be taken into account. To generate the hard processes with the correct fraction according to the cross sections the latter are calculated before the event simulation.

The Les Houches Accord interface [18, 19] specifies a standard format for the exchange of data between multi-purpose event generators like Herwig++, Pythia8 or Sherpa [20] and matrix element generators such as MadEvent/MadGraph [21] or dedicated generators like Vbfnlo [22]. Therefore it is possible to use hard processes generated by external matrix element generators to enlarge the variety of parton-level matrix elements.

In this work the matrix element $e^+e^- \to q\bar{q}$ for electron positron annihilation via $Z$ boson or $\gamma$ production to a quark antiquark pair is used.

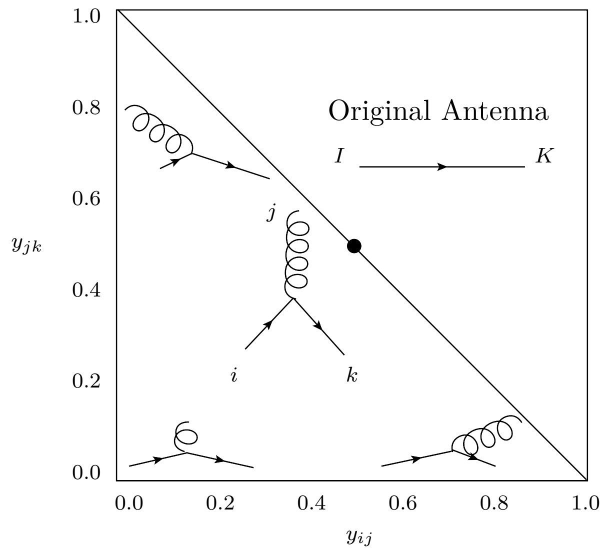


Figure 5.1: Dipole or antenna phase-space for a massless branching $IK \to ijk$ with its triangular shape due to the relation $y_{ij}+y_{jk}+y_{ik}=1$. The sketches illustrate the different phase-space regions. The hardest point in phase-space is marked with a dot. The soft singularities occur for $y_{ij} \to 0$ and $y_{jk} \to 0$, hence in the origin of the plot. The collinear singularities are located along the axes, for either $y_{ij} \to 0$ or $y_{jk} \to 0$

## 5.2 Shower Algorithm

After the weight of an event is calculated according to the hard process, as outlined in the previous section, the remaining coloured partons have to be evolved from the hard scale down to hadronic scales. The parton shower produces these secondary partons via successive parton emissions which re-sum effectively higher orders of perturbation theory. If the incoming particles are hadrons the initial state partons undergo showering as well. The initial state shower is described with a backward evolution. Since this work deals with electron-positron annihilation this is not further discussed. For the theoretical basics of the shower algorithms see Sec. 4.2.

A shower algorithm has to specify the following items [23], see also Sec. 4.2.5 and especially Eqs. (4.19) and (4.23):

1. The perturbative evolution variable.
2. The phase-space mapping $\mathrm{d}\Phi_{n+1}/\mathrm{d}\Phi_n$.
3. The radiation functions as a function of the phase-space variables.
4. The renormalization scale $\mu_R$.
5. Starting and ending scales.

Some of these points will be discussed in the following sections.

The phase-space region (triangle) of a colour dipole is shown in Fig. 5.1 in terms of scaled branching invariants (see Eq. (4.5))

$$y_{ab} = \frac{s_{ab}}{s} \le 1 \tag{5.1}$$

where $s$ is the invariant mass squared of the dipole. The sketches of the $q\bar{q} \to q\bar{q}g$ branchings illustrate the different phase-space regions. The soft singularities occur close to the origin and the collinear branchings take place close to one of the axis. The hardest point in phase-space where the emitted gluon takes most of the energy is marked with a point.

The main difference between the shower models is the type of branching: For parton showers as the angular-ordered shower of HERWIG++ $1 \to 2$ branchings occur whereas the basis of the antenna shower algorithm in VINCIA and the dipole shower of HERWIG++ is a $2 \to 3$ branching.

### 5.2.1 Herwig++ Shower Algorithms

Two different models for the parton shower are implemented in HERWIG++, namely the angular-ordered shower [24], which is used by default, and the dipole shower [25, 26]. As ordering variable for the latter the transverse momentum squared $p^2_{\perp\mathrm{dip}}$ or the virtuality $q^2_{\mathrm{dip}}$ can be chosen.

#### Angular-Ordered Shower

A major success of HERWIG [27], the predecessor to HERWIG++, was the treatment of soft gluon interference effects enabled by the angular ordering of emissions in the parton shower [1]. HERWIG++ uses the coherent branching algorithm (see Sec. 4.2.2) from Ref. [24], which generalizes the one used in HERWIG. Among other advantages and improvements this algorithm preserves the angular ordering property and provides invariance under boosts along the jet axis. The evolution scale from Eqs. 4.6 and 4.18 is here the variable $\tilde{q}$, defined as

$$\tilde{q}^2 = \frac{2E_a^2(1-\cos\theta_{bc})(1+\cos\theta_a)^2}{(1+\cos\theta_b)(1+\cos\theta_c)} \tag{5.2}$$

for time-like branchings $a \to bc$ where $\theta_a$, $\theta_b$ and $\theta_c$ respectively denote the angle between the according parton and the shower progenitor. For small angles the evolution variable reduces to

$$\tilde{q} \approx E_a\theta_{bc}. \tag{5.3}$$

The starting scales of the daughter partons $b$ and $c$ with momentum fractions $z$ and $1-z$ are then $z\tilde{q} \approx E_b\theta_{bc}$ and $(1-z)\tilde{q} \approx E_c\theta_{bc}$. The angular ordering property is thereby automatically implemented since the maximum opening angle of a following branching is $\theta_{bc}$. The use of collinear splitting functions together with the angular ordering property gives a good approximation of the coherent dipole radiation pattern.

To simulate possible radiation from a hard process the initial condition $\tilde{q}_h$, determined by the colour flow in the hard process, has to be chosen propabilisticly. Therefore colour partners are formed from the particles involved in the hard process. This choice is unique as long as no gluons enter the system. If gluons are involved a random choice is made between the two possibilities of the colour flow. As shown in Eq. 4.11 the direction of the colour partner gives the maximum emission angle for QCD radiation and therefore the initial condition for the angular-ordered shower.

The right most diagram in Fig. 5.2 shows the phase-space contours of constant values of the radiation function for the angular-ordered shower. Since this shower is not a dipole-

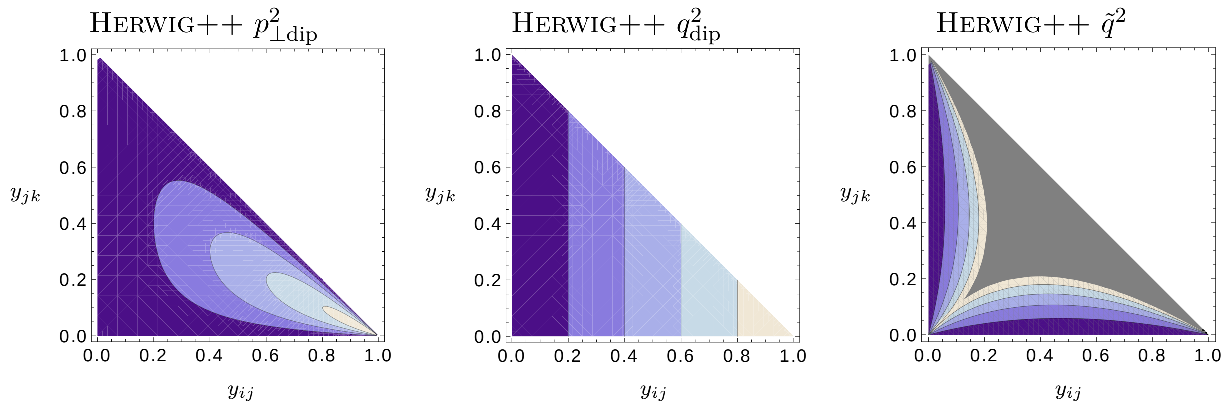


Figure 5.2: The dipole or antenna phase-space with different shower evolution variables of HERWIG++, represented as contours of constant values of the radiation function.

or antenna-based shower two different contours for each of the two emitting partons exist. Note that there are dead regions in the phase-space, indicated with the gray background colour.

Since the parton shower algorithm generates the emission from each particle independently the equation

$$\Delta(\tilde{q}_h, \tilde{q}) = \mathcal{R} \tag{5.4}$$

with random number $\mathcal{R} \in [0, 1]$ is solved for each particle. This gives the probability that the parton evolves from the initial scale $\tilde{q}_h$ down to a scale $\tilde{q}$ without any resolvable branching. In order to solve Eq. (5.4) analytically a crude Sudakov form factor with an overestimated branching probability is used. To get the exact distribution a vetoing procedure is implied. The Sudakov form factor for a branching $a \to b + c$

$$\Delta^{\mathrm{over}}(\tilde{q}_h, \tilde{q}) = \exp\left\{-\int_{\tilde{q}}^{\tilde{q}_h} \mathrm{d}\mathcal{P}_a^{\mathrm{over}}\right\} = \exp\left\{-\int_{\tilde{q}}^{\tilde{q}_h} \frac{\mathrm{d}\tilde{q}'}{\tilde{q}'} \int \mathrm{d}z \frac{\alpha_S^{\mathrm{over}}}{2\pi} P_{a\to b+c}^{\mathrm{over}}(z)\right\} \tag{5.5}$$

contains the overestimated quasi-collinear splitting functions $P^{\mathrm{over}}_{a\to b+c}(z) \geq P_{a\to b+c}(z, \tilde{q}')$ and coupling constant $\alpha_S^{\mathrm{over}} \geq \alpha_S(z, \tilde{q}')$. The splitting functions $P_{a\to b+c}(z, \tilde{q}')$ can be found in Ref. [1]. The equation $\Delta^{\mathrm{over}}(\tilde{q}_h, \tilde{q}) = \mathcal{R}$ can be solved for $\tilde{q}$ as

$$\tilde{q}^2 = \tilde{q}_h^2 \mathcal{R}^{1/r} \qquad \text{with} \qquad r = \frac{\mathrm{d}\mathcal{P}_a^{\mathrm{over}}}{\mathrm{d}\ln\tilde{q}^2}\ . \tag{5.6}$$

After obtaining a value for $\tilde{q}$ an associated $z$ value is generated and these values are rejected if [1]

- the value of $z$ lies outside the true phase-space limits: $p_\perp^2 < 0$
- $\alpha_S(z, \tilde{q}')/\alpha_S^{\mathrm{over}} < \mathcal{R}_1$
- $P_{a\to b+c}(z, \tilde{q}')/P^{\mathrm{over}}_{a\to b+c}(z) < \mathcal{R}_2$

with random numbers $\mathcal{R}_i \in [0, 1]$. If the value of $\tilde{q}$ gets rejected, the whole procedure is repeated where the hard scale $\tilde{q}_h$ is replaced by the new scale $\tilde{q}$. The evolution terminates when there is no phase-space for any further resolvable branching left. This infrared cutoff is expressed in terms of the transverse momentum. At the end of the shower all partons are set on their constituent mass-shell by reshuffeling momenta.

| Parameter | | Description |
|---|---|---|
| $\alpha_{M_Z}$ | AlphaMZ | Strong coupling at the $Z^0$ boson mass |
| $p_{\mathrm{T}}^{\min(f)}$ | pTmin | Shower cutoff for the angular-ordered shower |
| $\mu_{\mathrm{IR},FF}$ | IRCutoff | Infrared cutoff for final-final dipoles for the dipole shower |
| $\mu_{\mathrm{soft},FF}^{(f)}$ | ScreeningScale | Soft scale for final-final dipoles for the dipole shower |

Table 5.1: The main free parameters of the angular-ordered and the dipole shower of Herwig++ are listed. $(f)$ indicates that the parameter exists in different copies for different splitting processes.

**Dipole Shower**

The dipole shower is based on Catani-Seymor subtraction kernels [28], which have originally been derived in the context of the subtraction formalism for NLO calculations. Since the $2 \to 3$ splittings include a spectator parton, all partons are on their constituent mass-shell during the shower evolution. The dipole shower includes the effects of soft gluon coherence, as discussed in Sec. 4.2.2, if the emissions are ordered in transverse momentum.

The evolution of this shower works in principle the same as for the angular-ordered one since the dipoles are partitioned into two dipoles, each corresponding to one of the partons forming the original dipole. The total emission is hence the sum of the two splitting functions, each associated with one leg. From now on a dipole in the context of the Herwig++ dipole shower is meant to be a partitioned dipole whereas in the general case, a dipole describes the same object as an antenna.

After the hard subprocess the partons are sorted in colour singlets which are now evolved independently. For each dipole $I, K$ any possible splitting $I, K \to i, j, k$ is taken into account where parton $I$ acts as emitter and parton $K$ as spectator. Both possible emitter-spectator assignments are included, meaning that $K, I \to k, j, i$ with emitter $K$ and spectator parton $I$ is also considered. The two different assignments correspond to the two partitioned dipoles of each original dipole. The ordering variable for the emission off parton $I$ can be expressed as

$$p_{\perp\mathrm{dip}}^2 = s_{IK}\left(y_{ij}y_{jk}\frac{1-y_{jk}}{1-y_{ij}} - 4\left(\frac{y_{ij}y_{jk}}{1-y_{ij}}\right)^2\right) \tag{5.7}$$

and the dimensionless and normalized form is $4\,p_{\perp\mathrm{dip}}^2/s_{IK}$. The outgoing partons initiate a parton branching where the Sudakov form factor

$$\Delta(p_{\perp\max}^2, p_{\perp\mathrm{dip}}^2) = \exp\left\{-\int_{p_{\perp\mathrm{dip}}^2}^{p_{\perp\max}^2}\frac{\mathrm{d}p_\perp^2}{p_\perp^2}\int \mathrm{d}z P_{I,K\to i,j,k}(p_\perp^2, z)\right\} \tag{5.8}$$

with the hard scale $p_{\perp\max}^2$ associated to the current emitter and the appropriate splitting probabilities $P_{I,K\to i,j,k}(p_\perp^2, z)$. The shower terminates when the evolution variable falls below the infrared cutoff $\mu_{IR}^2$ which is a free parameter of the dipole shower. For a reasonable choice of this variable it is important to keep the fact in mind that perturbative

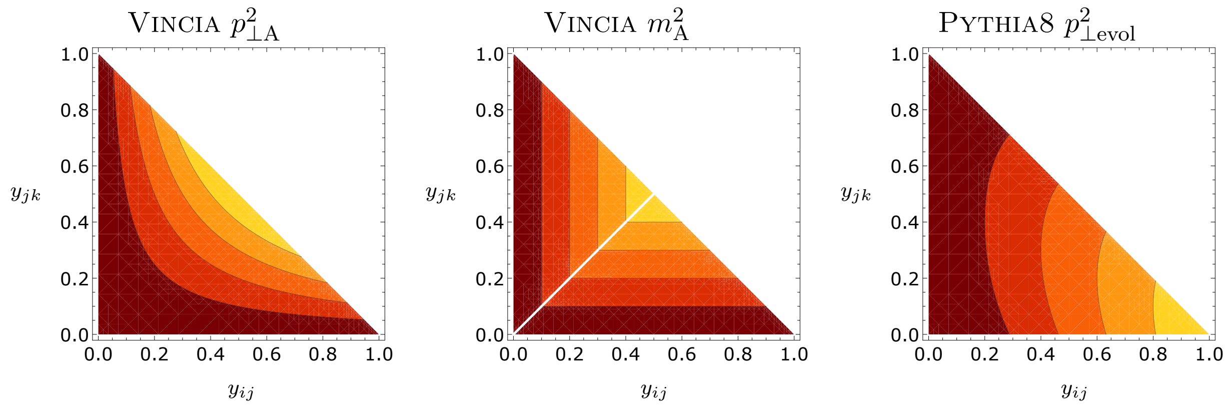


Figure 5.3: The dipole or antenna phase-space with different shower evolution variables of VINCIA and PYTHIA8, represented as contours of constant values of the radiation function.

QCD should still be valid at this energy scale. As a non-coherent alternative of the dipole shower the evolution variable can be chosen to be the virtuality $q^2_{\text{dip}}$.

The two left plots in Fig. 5.2 show the phase-space contours of constant values of the radiation function for the two possible evolution variables of the dipole shower. Since this shower uses partitioned dipoles the evolution of only one of the parent partons is shown.

The main free parameters of the HERWIG++ shower algorithms are listed in Tab. 5.1. The strong coupling constant controls the amount of QCD radiation during the shower and the scale at which the perturbative evolution terminates is the shower cutoff.

### 5.2.2 Vincia Shower Algorithm

VINCIA [23] is a plugin to the PYTHIA8 event generator which replaces the PYTHIA8 parton shower with a shower model based on antenna functions, see Sec. 4.2.4. The Altarelli-Parisi splitting functions in the collinear limit and the eikonal factor in the soft limit are reproduced by these antenna functions. As evolution variable $y_E$ two different choices are implemented, namely the transverse momentum and the mass of the antenna,

$$y_E = \begin{cases} \text{type } \alpha,\ p^2_{\perp\text{A}}\text{-ordering} \quad : \quad y^2_\alpha = 4\dfrac{s_{ij}s_{jk}}{s^2_{IK}} = 4y_{ij}y_{jk} = 4\dfrac{p^2_{\perp\text{A}}}{s_{IK}} \\[2ex] \text{type } \beta,\ m^2_{\text{A}}\text{-ordering} \quad : \quad y^2_\beta = \dfrac{2\min(s_{ij}, s_{jk})}{s_{IK}} = 2\min(y_{ij}, y_{jk}) = \dfrac{2m^2_{\text{A}}}{s_{IK}} \end{cases} \tag{5.9}$$

for a branching $IK \to ijk$. The prefactors, 4 for type $\alpha$ and 2 for type $\beta$, make the maximal value of the evolution variable equal to the dipole invariant mass. The maximal value is reached when the two parents are collinear and back-to-back with the emitted parton, which carries half the total energy. The angular ordering is not explicit included since coherence is an intrinsic property of the antenna functions, hence no additional requirement is needed to enforce it.

Fig. 5.3 shows the dipole phase-space and some evolution variables as contours. The $p^2_{\perp\text{A}}$-ordered dipole shower tends to first produce a hard-collinear branching, a soft branching would occur “later” and vice versa for the mass-ordered shower since the area that has to be filled in order to get to a hard collinear splitting and therefore the “time” to get to this splitting is larger for the $p^2_{\perp\mathrm{A}}$-ordered than for the $m^2_{\mathrm{A}}$-ordered shower.

As radiation functions different antenna sets are implemented, for instance the Gehrmann-Gehrmann-de-Ridder-Glover ones listed in Tab. 4.2. Generally, the differences between different sets can be used to estimate uncertainties. A trial branching for each antenna dipole is found by generating a random number $\mathcal{R} \in [0, 1]$ and solving the equation

$$\hat{\Delta}(y_{\mathrm{start}}, y_{\mathrm{trial}}) = \mathcal{R} \tag{5.10}$$

for $y_{\mathrm{trial}}$. The trial Sudakov form factor

$$\hat{\Delta}(y_{\mathrm{start}}, y_{\mathrm{trial}}) = \exp\left\{ -\int_{y_{\mathrm{trial}}}^{y_{\mathrm{start}}} \mathrm{d}y_{\mathrm{trial}} \int_0^1 \mathrm{d}y_{ij} \int_0^1 \mathrm{d}y_{jk} \delta\left(y_E - y_E(y_{ij}, y_{jk})\right) \frac{\hat{\mathcal{A}}(y_{ij}, y_{jk})}{16\pi^2} \right\} \tag{5.11}$$

contains an overestimate of the antenna function

$$\hat{\mathcal{A}}(y_{ij}, y_{jk}) \equiv s_{IK} \hat{A}(y_{ij}, y_{jk}; s_{IK}, \hat{\alpha}_S(y_E)) > s_{IK} A(y_{ij}, y_{jk}; s_{IK}, \alpha_S(y_E)) \tag{5.12}$$

with the overestimated first-order running trial $\hat{\alpha}_S(y_E) > \alpha_S(y_E)$ depending on the evolution variable $y_E$. After computing the full kinematics of the trial branching it can be vetoed with the probability $1 - A/\hat{A}$. The trial scale becomes the new starting scale if the branching generated from it is not vetoed by the algorithm. The shower terminates when the evolution variable falls below an infrared cutoff, when there is no perturbative evolution space left.

In a strongly-ordered shower the evolution variable $y_E$ of a branching is always smaller than the one of the previous branching: $y_{n+1} < y_n$. Therefore the ordering condition acts like a step function in phase-space $\Theta(y_n - y_{n+1})$. Vincia includes also smooth ordering where a dampening factor

$$\Theta(\tilde{y}_E^2 - y_E^2) \quad \to \quad P_{imp} = \frac{\tilde{y}_E^2}{\tilde{y}_E^2 + y_E^2} \tag{5.13}$$

is used instead of a sharp cutoff at the ordering scale, allowing unordered branchings with a suppressed probability. $y_E$ denotes the scale of the next branching and $\tilde{y}_E$ is the evolution scale evaluated on the pre-branching configuration. If more than one branching history is possible $\tilde{y}_E$ is chosen to be the smallest of the corresponding evolution scales. In the strongly-ordered limit, $y_E^2 \gg \tilde{y}_E^2$, $P_{imp}$ tends to unity, whereas for highly unordered branchings, $y_E^2 \ll \tilde{y}_E^2$, $P_{imp}$ tends to zero. In the ordering threshold, $y_E^2 \sim \tilde{y}_E^2$, $P_{imp}$ is about 1/2, thus allowing weakly unordered branchings to occur.

### 5.2.3 Pythia8 Shower Algorithm

The shower algorithm used by Pythia8 was first introduced in Pythia6 [29], [30] and is a hybrid between the parton shower and the dipole approach. The emissions are associated with the evolution of a single parton, but recoil effects occur inside dipoles. The shower is ordered approximately in the $p_\perp^2$ of a branching where $p_\perp$ is the transverse momentum for each of the two partons remaining after a branching with respect to the direction of the parent parton, in the rest frame of the dipole [29]. The formal definition of the evolution variable is

$$p^2_{\perp\mathrm{evol}} = z(1-z)Q^2 = z(1-z)(m^2 - m_0^2) \tag{5.14}$$

| Parameter | | Description |
|---|---|---|
| $\alpha_S$ | alphaS | Strong coupling at the $Z^0$ boson mass |
| $p_\perp^{2\ \mathrm{min}}$ | cutoffScale | Shower cutoff |

Table 5.2: The table lists the parameters for the shower model of VINCIA and PYTHIA8.

with energy sharing $z$, off- and on-shell mass $m$ and $m_0$ and virtuality $Q^2$ of the branching parton. The dimensionless and normalized ordering variable can be expressed in terms of the branching invariants,

$$4\,\frac{p^2_{\perp\mathrm{evol}}}{s_{IK}} = 4\,\frac{1-y_{jk}}{1-y_{ij}}\left(1-\frac{1-y_{jk}}{1-y_{ij}}\right)y_{ij}\ , \tag{5.15}$$

for a process $IK \to ijk$. The starting scale $p^2_{\perp\mathrm{max}}$ is thereby defined either by the hard process or by the proceeding shower branchings [30]. The evolution equation

$$\mathrm{d}\mathcal{P}_a = \frac{\mathrm{d}p^2_{\perp\mathrm{evol}}}{p^2_{\perp\mathrm{evol}}}\frac{\alpha_s(p^2_{\perp\mathrm{evol}})}{2\pi}P_{a\to bc}(z)\mathrm{d}z\Delta(p^2_{\perp\mathrm{max}},p^2_{\perp\mathrm{evol}}) \tag{5.16}$$

is used to find trial branchings $a \to bc$. The parton with the largest transverse momentum undergoes the first branching. The shower continues by iterating towards lower $p^2_{\perp\mathrm{evol}}$ until the cutoff scale $p^2_{\perp\mathrm{min}}$ is reached.

The right most diagram of Fig. 5.3 shows the phase-space contours of constant values of the radiation function for the PYTHIA8 parton shower. Since this shower is not a dipole- or antenna-based shower the evolution of only one of the parent partons is shown.

The main free parameters of the shower model of VINCIA and PYTHIA8, the strong coupling constant and the infrared shower cutoff, are listed in Tab. 5.2.

## 5.3 Matching

Matching describes the improvement in the description of the shower by combining fixed order calculations with the shower approximation. Different strategies for the matching procedure exist, such as phase space slicing, subtraction and universality. Fig. 5.4 shows the coefficients of the perturbative series, see Sec. 4.1, represented as boxes for specific numbers of additional legs $k$ and loops $l$. Thus the Born cross section for the hard process is represented by the coefficient $\sigma_0^{(0)}$. Green boxes indicate that the exact matrix element is used for this coefficient and yellow denotes the use of the shower approximation. The upper left plot in Fig. 5.4 shows the accuracy of the coefficients when no matching is used. Thus LO accuracy for the Born cross section is obtained and the shower approximation resums all higher orders.

In the slicing approach the phase space is separated by the matching scale into two regions, one that is mainly described by the matrix element and the other one by the shower. This approach was first used in HERWIG to include higher order corrections for the first emission after the hard process [31, 32]. The shower is set to zero above a certain matching scale, either by vetoing any emissions above that scale or due to dead zones in the shower, as in HERWIG and HERWIG++. The result is shown in the upper right diagram in Fig. 5.4.

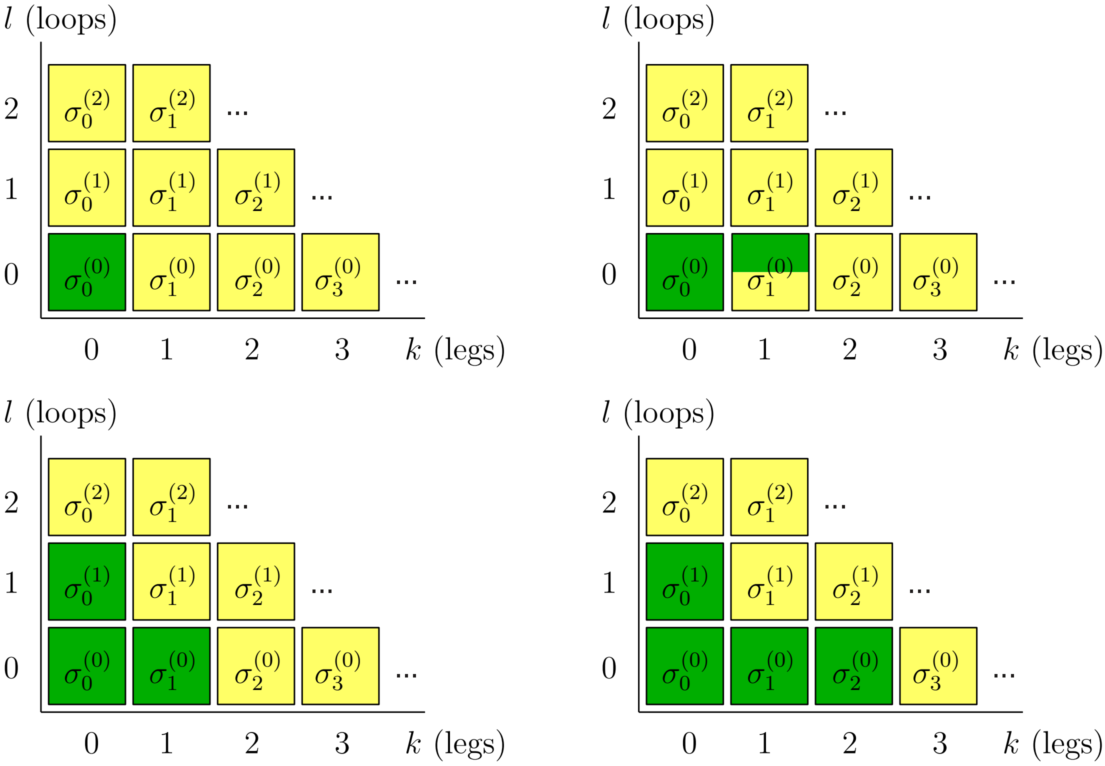


Figure 5.4: Coefficients of the perturbative series, see Sec. 4.1. The upper left diagram shows the coverage when no matching is used, the upper right plot for the matching that will be used in the angular-ordered shower of Herwig++. The lower left diagrams shows the coverage for the NLO dipole shower of Herwig++ and default Pythia8. When referred to Vincia with additional matching the accuracy shown in the lower right diagram is obtained.

Above the matching scale the accuracy of the exact matrix element can be obtained. The angular-ordered shower of Herwig++ includes correction by default and is used solely with this accuracy.

In the subtraction scheme, used to obtain NLO accuracy with the dipole shower of Herwig++, see Ref. [26], the shower approximation is subtracted from the NLO calculation and this is added to shower approximation. This approach is also used by strategies like Mc@nlo [33,34] and was implemented in Herwig++ [35]. The lower left diagram in Fig. 5.4 shows the resulting accuracy, NLO for the hard process and LO for the first emission. When referring to the NLO Herwig++ dipole shower this accuracy is obtained. The dipole shower is used with LO accuracy, as illustrated in the upper left diagram, by default in this work, unless otherwise indicated.

Pythia8 with default settings uses matrix-element corrections. Starting with the Born level process the shower generates the first emission which is correct to the exact matrix element by using a multiplicative factor given by the ratio of the matrix element to the shower approximation. The correction for the $\sigma_0^{(1)}$ coefficient is included as well since, for the process $e^+e^- \to Z^0 \to q\bar{q}$, this corresponds a factor $1 + \alpha_S/\pi$ correcting the total $Z^0$ decay rate. When normalizing to the total rate, this factor just drops out. Therefore default Pythia8 includes NLO accuracy for the hard process and LO for the first emission, as sketched in the lower left diagramm of Fig. 5.4.

Since the matching in PYTHIA8 is included in the default settings, VINCIA inherits this as well. If not otherwise indicated, this accuracy is used for VINCIA. To include LO accuracy for the fourth jet as well, the first emission after the hard process is corrected to the exact matrix element, as described for PYTHIA8. The first virtual correction is obtain by using unitarity[1] of the shower and also corrected to the matrix element. The procedure is repeated by correcting the second shower emission to the exact matrix element leading to the accuracy shown in the lower right diagram of Fig. 5.4. The hard process results in NLO accuracy and the first and second additional emissions are obtained with LO accuracy.

## 5.4 Hadronization

In order to transfer the partons produced the shower, into the observed hadrons a non-perturbative hadronization model has to be implemented. For the different approaches see Sec. 4.3. Depending on the Monte Carlo generator a different model is used: HERWIG++ applies the cluster hadronization model described in Sec. 4.3.3 that groups the remaining partons together into clusters. The hadronization model of PYTHIA8 is based solely on the Lund string fragmentation framework, see Sec. 4.3.2.

### 5.4.1 Cluster Model in Herwig++

The gluons at the end of the parton shower have to split non-perturbativly into quark-antiquark pairs which is why a constituent mass is given to them. After the decays of the gluon, only colour connected (di)quarks and anti-(di)quarks exist, which colour singlets. Then clusters are formed by the colour singlets with the momentum given by the sum of the momenta of the constituent partons. Heavy clusters first have to split into lighter clusters before they decay into hadrons, since the cluster mass spectrum is peaked at low masses and clusters can be regarded as excited hadron resonances. A heavy cluster of mass $M$ splits into two lighter clusters if the condition

$$M^{\mathrm{Cl_{pow}}} \geq \mathrm{Cl}_{\mathrm{max}}^{\mathrm{Cl_{pow}}} + (m_1 + m_2)^{\mathrm{Cl_{pow}}} \tag{5.17}$$

holds, where $m_{1,2}$ are the masses of the constituent partons of the heavy cluster. $\mathrm{Cl_{max}}$ is the maximum cluster mass above which clusters containing light, charm or bottom quarks[2] respectively undergo cluster fission. The exponent $\mathrm{Cl_{pow}}$ controls whether these clusters undergo cluster fission or not. If a cluster is needed to be splitt, a $q\bar{q}$ pair is popped from the vacuum with the probability $\mathrm{P_{wt}}$ for the different flavours. The mass distributions of the two new clusters are given by

$$M_1 = m_1 + (M - m_1 - m_q)\mathcal{R}_1^{1/\mathrm{P_{split}}} \quad \text{and} \tag{5.18}$$

$$M_2 = m_2 + (M - m_2 - m_q)\mathcal{R}_2^{1/\mathrm{P_{split}}} \tag{5.19}$$

with the mass $m_q$ of the parton popped from the vacuum and random numbers $\mathcal{R}$. At last the cluster are decayed into pairs of hadrons whose momenta are smeared through an angle according to a Gaussian distribution

$$\cos\theta_{\mathrm{smear}} = 1 + \mathrm{Cl_{smr}} \log \mathcal{R} \ . \tag{5.20}$$

[1] The virtual correction plus the integral of the real emission have to add up to a finite factor due to probability conservation.

[2] $\mathrm{Cl_{max}}$ exists, as $\mathrm{Cl_{pow}}$, $\mathrm{Cl_{smr}}$ and $\mathrm{P_{split}}$, in three different copies for the different flavours: $(f) = (u, d, s), c, b$.

| Parameter | | Description |
|---|---|---|
| $m_{g,c}$ | ConsituentMass | Gluon mass |
| $\mathrm{Cl}^{(f)}_{\mathrm{max}}$ | ClMaxLight, ClMaxCharm, ClMaxBottom | Maximum cluster mass |
| $\mathrm{Cl}^{(f)}_{\mathrm{pow}}$ | ClPowLight, ClPowCharm, ClPowBottom | Cluster mass exponent |
| $\mathrm{Cl}^{(f)}_{\mathrm{smr}}$ | ClSmrLight, ClSmrCharm, ClSmrBottom | Smearing parameter |
| $P^{(f)}_{\mathrm{split}}$ | PSplitLight, PSplitCharm, PSplitBottom | Mass exponent for daughter clusters |

Table 5.3: The table lists the main free parameters for the Herwig++ cluster hadronization model. The ones indicated by the superscript $(f)$ exist in three copies for the different flavours: $(f) = (u, d, s), c, b$.

The relative weights for producing singlet and decuplet baryons respectively in the decay process are given by $W_{\mathrm{sng}}$ and $W_{\mathrm{dec}}$. Due to a small fraction of clusters that are too light to decay into two hadrons clusters containing charm or bottom quarks are allowed to produce two hadrons which decay into a single hadron with the mass

$$M < M_{\mathrm{limit}} = (1 + \mathrm{SHL})M_{\mathrm{threshold}} \tag{5.21}$$

Therefore the single hadron limits (SHL) for charm and bottom quarks control the limit on the production of single clusters for charm and bottom clusters respectively.

To provide an overview of the main free parameters of the cluster hadronization model, that will be used in following chapters, Tab. 5.3 lists these parameters.

## 5.4.2 Lund String Model in Pythia8

As mentioned above the hadronization model implemented in Pythia8 is based solely on the Lund string fragmentation framework. The online documentation of Pythia8 provides detailed information about the parameters of the string model. Thus additional information to the following recap can be found there.

**Fragmentation functions**

The fraction $z$ of the longitudinal momentum of the quark at the endpoint of the strings carried by the created hadron has to be chosen with the help of fragmentation functions. The so-called Lund symmetric fragmentation function is

$$f(z) = \frac{1}{z}(1-z)^{a_{\mathrm{L}}} \exp\left(-\frac{b_{\mathrm{L}} m_T^2}{z}\right) \tag{5.22}$$

with transverse mass $m_T$ and the two main free parameters $a_{\mathrm{L}}$ and $b_{\mathrm{L}}$ where in principle $a_{\mathrm{L}}$ can be flavour-dependent and $b_{\mathrm{L}}$ is universal, meaning common for all flavours. For heavy quarks an extra factor $\left(\frac{1}{z}\right)^{r_Q b_{\mathrm{L}} m_Q^2}$ with the multiplicative factor $r_Q$ for quark type $Q$ is introduced which leads to a fragmentation function of

$$f(z) = \left(\frac{1}{z}\right)^{1+r_Q b_{\mathrm{L}} m_Q^2} (1-z)^{a_{\mathrm{L}}} \exp\left(-\frac{b_{\mathrm{L}} m_T^2}{z}\right) . \tag{5.23}$$

| Parameter | | Description |
|---|---|---|
| $a_{\mathrm{L}}$ | aLund | Parameter of the Lund symmetric fragmentation function |
| $b_{\mathrm{L}}$ | bLund | Parameter of the Lund symmetric fragmentation function |
| $a_{\mathrm{ED}}$ | aExtraDiquark | $a$ parameter for diquarks, with total $a = a_{\mathrm{L}} + a_{\mathrm{ED}}$ |
| $\sigma$ | PTsigma | Total width of the fragmentation $p_{\perp}$ |

Table 5.4: The table lists the main free parameters for the PYTHIA8 Lund string hadronization model.

Although $b_{\mathrm{L}}$ is universal, it is possible to set both parameters flavour-dependent ($a_{\mathrm{L},Q}$ and $b_{\mathrm{L},Q}$) leading to a general expression of Eq. (5.23). For diquarks relative to normal quarks the shape

$$f(z) = \frac{1}{z} z^{a_{\mathrm{L},i}} \left(\frac{1-z}{z}\right)^{a_{\mathrm{L},j}} \exp\left(-\frac{b_{\mathrm{L}} m_T^2}{z}\right) \tag{5.24}$$

for going from an old flavour $i$ to a new one $j$ is implemented. This allows a larger $a$ parameter for diquarks, with total $a = a_{\mathrm{L}} + a_{\mathrm{ED}}$ where ED stands for ExtraDiquark.

### Fragmentation $p_T$

If a string breaks, the according quark and antiquark receive opposite and compensating $p_T$ kicks. Thereby $p_x$ and $p_y$ are distributed separately via a Gaussian distribution with width $\sigma_q$:

$$d(\mathrm{Prob}) = \exp\left(-\frac{p_x^2 + p_y^2}{2\sigma_q^2}\right) . \tag{5.25}$$

Then the total squared width is

$$\langle p_T^2 \rangle = \langle p_x^2 \rangle + \langle p_y^2 \rangle = 2\sigma_q^2 = \sigma^2 \tag{5.26}$$

with parameter $\sigma$ for the width in the fragmentation process. Since hadrons receive $p_T$ contributions from one string break on each side, they therefore have $\langle p_x^2 \rangle_{\mathrm{had}} = \langle p_y^2 \rangle_{\mathrm{had}} = \sigma^2$, and thus $\langle p_T^2 \rangle_{\mathrm{had}} = 2\sigma^2$.

### Flavour Selection

During the fragmentation process new flavours have to be chosen and depending on the flavour of the quarks specific hadrons are produced. These choices are made by a separate PYTHIA8 class with a large number of additional parameters for the relative production rate of different particle species.

To provide an overview of the main free parameters of the string hadronization model of PYTHIA8, that will be used in following chapters, Tab. 5.3 lists these parameters. Many flavour dependent parameters exist in addition, but they are not listed here since they will not be used throughout this thesis.

## 5.5 The Rivet Analysis Tool

RIVET [36] is a generator validation system which provides the tools for analyzing simulations of collisions at high energies. RIVET is generator independent since it makes use of the data format HepMC [37], which contains all information of an event except the used generator. For the validation of an event generator it is crucial to compare its predictions to real data. Therefore RIVET includes a library with published and unpublished data stored in histograms which have the exact same properties as the histograms used to analyze the generator events. In the course of this work RIVET was used to write new analyses and some of the included analyses were used in the tuning process.

## 5.6 The Professor Tuning System

PROFESSOR [38] is a tuning tool for Monte Carlo event generators which is used to tune model parameters to experimental data. The simulation results are thereby obtained by using RIVET which was described in the previous section.

The aim of the tuning process is to define a goodness of fit function between the generated predictions and reference data, and then to minimize that function [39]. The first step is to generate multiple generator runs at different parameter-space points where the randomly distributed parameter points are created with prof-sampleparams. Then a general parameterization function for the Monte Carlo generator response has to be chosen: PROFESSOR has polynomials of different orders to choose from. The output of prof-interpolate is a set of functions $f^{(b)}(\vec{p})$, which model the true Monte Carlo response, $\mathrm{MC}_b$, of each observable bin $b$ to changes in the $P$-element parameter vector $\vec{p}$ [39]. For example a polynomial of second order looks like

$$\mathrm{MC}_b(\vec{p}) \approx f^{(b)}(\vec{p}) = \alpha_0^{(b)} + \sum_i \beta_i^{(b)} p_i' + \sum_{i \geq j} \gamma_{ij}^{(b)} p_i' p_j' \tag{5.27}$$

with the shifted parameter vector $\vec{p}' \equiv \vec{p} - \vec{p}_0$. The actual choice of $\vec{p}_0$ is irrelevant, since the function remains the same and only the coefficients are redefined.

For a polynomial of order $n$ with $P$ parameters the number of coefficients to be calculated is

$$N_n^{(P)} = \sum_{i=0}^{n} \frac{1}{i!} \prod_{j=0}^{i-1} (P+j) \ . \tag{5.28}$$

The number of generator runs is determined by the number of coefficients to be calculated. Theoretically the two numbers could be exactly the same but in order to get reasonable and robust results for the coefficients one should oversample with at least a factor 2. The interpolation is performed for a certain run combination which acts as anchor point for the polynomial parameterization of the Monte Carlo response function. A run combination contains an amount of the Monte Carlos runs and the total number of these combinations should be about

$$N_{\mathrm{rc}} = \frac{4}{3} N_n^{(P)} \ . \tag{5.29}$$

After the interpolation PROFESSOR provides various methods to plot the sensitivity of the model parameters to the observables.

The next step is to calculate the GoF with the definition

$$\chi^2(\vec{p}) = \sum_{\mathcal{O}} w_{\mathcal{O}} \sum_{b\in\mathcal{O}} \frac{(f^{(b)}(\vec{p}) - \mathcal{R}^{(b)})^2}{{\Delta^{(b)}}^2} \tag{5.30}$$

with the reference value $\mathcal{R}^{(b)}$ and the total error ${\Delta^{(b)}}^2$ of the data per bin $b$ and observable $\mathcal{O}$. In order to give for example observables with only one bin higher importance weights $w_{\mathcal{O}}$ are used for each observable. These weights also used for the calculation of the number of degrees of freedom,

$$N_{\mathrm{dof}} = \sum_{\mathcal{O}} w_{\mathcal{O}} |b \in \mathcal{O}| \ . \tag{5.31}$$

In the final stage prof-tune minimizes the GoF in Eq. (5.30) numerical and provides the corresponding parameter values. The minimization is performed for the run combinations used in the interpolation step.

# 6. Analyses for the Simulation

To investigate properties such as QCD colour coherence or the emission of soft jets, observables reflecting these properties are required. The way how colour coherence is included in the shower approximation depends on the generator that is used. Therefore observables that tell the different shower models apart, can be used to validate the shower properties. As described in the previous chapter six different models will be examined: The default angular-ordered parton shower and the dipole shower of HERWIG++, of which the latter is used with ordering in transverse momentum $p^2_{\perp\text{dip}}$ as well as with ordering in virtuality $q^2_{\text{dip}}$, the $p^2_{\perp\text{evol}}$-ordered parton shower of PYTHIA8 with angular vetos and the antenna-based shower of VINCIA, used with ordering in transverse momentum $p^2_{\perp\text{A}}$ of the antenna or in antenna mass $m^2_{\text{A}}$. The events are generated with the matrix element

$$e^+e^- \to q\bar{q} \quad \text{for 5 flavours } (u,\ d,\ c,\ s,\ b) \tag{6.1}$$

at the $Z^0$ pole, with a center-of-mass energy of 91.2 GeV. In order to focus on the pure shower properties and make the models more directly no higher order matching[1] is included and VINCIA is used with strong ordering. The events are analyzed using the RIVET framework, described in Sec. 5.5.

In the first section some basic ingredients for the analyses are described. The adjoining sections dwell on the analyses themselves and reveal some results.

## 6.1 Basics: Jet Algorithms

This section gives a short overview on the way how the hadrons of the final states are formed into jets. FASTJET [40], a C++ package for jet finding in *pp*- and $e^+e^-$-collisions, provides two algorithms for the latter: The $k_t$ [41] and the generalized $k_t$ algorithm that will be described in the following.

### $k_t$ Algorithm for $e^+e^-$ Collisions

The $k_t$ algorithm has only the single distance measure

$$d_{ij} = 2 \cdot \min\left(E_i^2, E_j^2\right)(1 - \cos\theta_{ij}) \ . \tag{6.2}$$

[1]Correction of the first real emission in the angular-ordered shower, LO accuracy for the dipole shower of HERWIG++ and the default matching in PYTHIA8 for VINCIA and PYTHIA8.

**Exclusive algorithm.** The following steps are conducted in order to obtain exclusive jets [42]:

1. Calculate all the distances $d_{ij}$ according to Eq. (6.2).
2. Find the minimum $d_{\min}$ of the distances $d_{ij}$.
3. If $d_{\min}$ is below some cutoff $d_{\text{cut}}$, recombine $i$ and $j$ and return to step 1.
4. Otherwise, all remaining particles are declared to be jets and the iteration stops.

The corresponding dimensionless cutoff $y_{\text{cut}}$ is defined as

$$y_{\text{cut}} = \frac{d_{\text{cut}}}{Q^2} \tag{6.3}$$

with the center-of-mass energy $Q$. The $n \to n+1$ clustering scale $y_{n\to n+1}$ is the $y_{\min}$ corresponding to the recombination that went from $n+1$ to $n$ jets.

### Generalized $k_t$ Algorithm for $e^+e^-$ Collisions

The generalized $k_t$ algorithm has two distances

$$d_{ij} = \begin{cases} \min\left(E_i^{2p}, E_j^{2p}\right) \dfrac{1-\cos\theta_{ij}}{1-\cos R} & \text{for } 0 \leq R < \pi \\[2ex] \min\left(E_i^{2p}, E_j^{2p}\right) \dfrac{1-\cos\theta_{ij}}{3+\cos R} & \text{for } \pi \leq R < 3\pi \end{cases} \tag{6.4}$$

$$d_{iB} = E_i^{2p} \tag{6.5}$$

with energy $E_i$ of particle $i$, angle $\theta_{ij}$ between the particles $i$ and $j$ and the two free parameters $p$ and $R$. For $\pi \leq R < 3\pi$ the distance $d_{iB}$ does not contribute since there is always a $d_{ij}$ which is smaller than the beam distance $d_{iB}$.

**Inclusive algorithm.** The following steps are conducted in order to obtain inclusive jets [42]:

1. Calculate all the distances $d_{ij}$ and $d_{iB}$ according to Eqs. (6.4) and (6.5).
2. Find the minimum of the distances $d_{ij}$ and $d_{iB}$.
3. If a $d_{ij}$ is smallest, recombine $i$ and $j$ and return to step 1.
4. If a $d_{iB}$ is smallest, call $i$ a (final-state) jet and remove it from the particle list.
5. Stop if all particles are clustered.

Thus all particles are part of a final-state jet and there is neither a beam-jet nor a cutoff parameter. This algorithm is only used in the inclusive sense here.

### Recombination schemes

The recombination scheme used for the following analyses is the $E$-scheme which is also the most widespread one. Since the 4-vectors of two particles are added in order to combine them, the scheme is called 4-vector recombination scheme as well.


Figure 6.1: The sketch on the left shows the event topology resulting from the cuts and the one on the right shows the observable $\alpha^*$.

## 6.2 Analysis on Parton Level

As a starting point the analysis described in Ref. [25] for investigating coherence properties is used. In order to obtain partonic final states[2] hadronization and hadronic decays in Herwig++ are switched off. Events with exactly four partons are chosen and these partons are then ordered in energy with the first parton referring to the hardest. However, to select exactly four partons is not physical in the sense that this cannot be reproduced in an experiment. To obtain special event topologies the angles between the partons are constrained. The second and third parton are supposed to form a collinear pair, thus a cut on the angle between these partons,

$$\alpha_{23} < \pi/8, \tag{6.6}$$

is implied. Due to energy-momentum conservation the collinear parton pair is balanced by a very hard first parton, see left sketch of Fig. 6.1. From this three-parton system the emission of a soft fourth parton, where the softness is ensured with the cut

$$E_4 < E_{\text{tot}}/10 \ , \tag{6.7}$$

is investigated. In order to be sensitive to colour coherence the fourth parton is required to be emitted by the second parton:

$$\alpha_{24} < \pi/2 \ . \tag{6.8}$$

The observable $\alpha^*$ is the difference in opening angles and defined as

$$\alpha^* = \alpha_{24} - \alpha_{23} \ . \tag{6.9}$$

On the right-hand side of Fig. 6.1 the observable $\alpha^*$ is sketched. To illustrate its geometrical meaning, cones of the third and fourth parton around the second parton are drawn to reflect the angles $\alpha_{24}$ and $\alpha_{23}$. The difference between the opening angles of these two cones is expressed by $\alpha^*$. Thus if the observable is smaller than zero the fourth parton lies within the cone formed by the third around the second parton and outside the cone if the value of $\alpha^*$ is greater than zero.

Fig. 6.2 shows the normalized distribution of $\alpha^*$ for the Herwig++ shower models; the left plot is taken from Ref. [25] to confirm the result found there. The shapes of all shower models clearly coincide in the two plots. An enhancement at about $\alpha^* \gtrsim 0$, where the third and fourth parton are emitted off parton two at nearly the same angle, shows up for the $p^2_{\perp\text{dip}}$- and for the angular-ordered shower. The enhancement is not exactly at $\alpha^* = 0$

[2] Parton level is the final state in the generated events consisting of quarks and gluons after the termination of the parton shower.

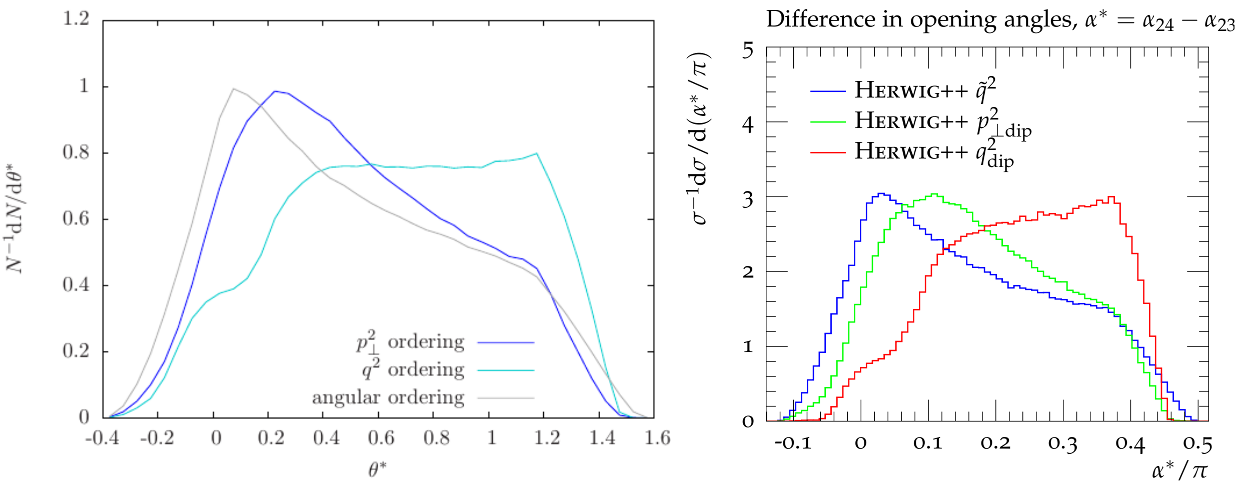


Figure 6.2: Normalized distributions of the observable $\alpha^*$ on parton level for the different showers of Herwig++: Herwig++ $\tilde{q}^2$ and angular ordering refer to the angular-ordered default shower and Herwig++ $p^2_{\perp\mathrm{dip}}$ or $q^2_{\mathrm{dip}}$ shower and $p^2_\perp$ or $q^2_{\mathrm{dip}}$ ordering refer to the $p^2_{\perp\mathrm{dip}}$- or $q^2_{\mathrm{dip}}$-ordered dipole shower respectively. The left plot is taken from Ref. [25].

since the singularity is screened by the Sudakov form factor. For emissions at large angles, the soft parton cannot resolve the colour sub structure of the collinear parton pair. Hence the soft parton is emitted as if there were only two hard partons. If $\alpha_{23}$ is very small, the angle between the soft parton and its emitter is $\alpha^*$, explaining the drop down from $\alpha^* = 3\pi/8$ until $\alpha^* = \pi/2$. The prediction of the $q^2_{\mathrm{dip}}$-ordered shower looks different in shape, compared to the two other shower models. Since this shower is non-coherent a different behaviour was expected.

## 6.3 Influence of Hadronization

To compare the simulation results with data, events on hadron level[3] are necessary. Instead of partons, jets on hadron level are selected now, since can be done in experiment and leads to proper observables. By clustering the final states into jets the hadron level events are mapped back to the partonic system after the shower termination. This section aims at finding a suitable jet algorithm and cuts for the event selection to define the mapping as precise as possible. The same analysis applies for events on hadron and parton level to investigate the influence of hadronization. Since other disruptive effects can be evoked by $B$ decays the comparison with events where all hadrons containing a $b$ quark are set stable, is performed as well. In order to take statistical uncertainties into account, samples of $5 \cdot 10^5$ events are used.

### 6.3.1 Observables

The events are clustered into either two or four jets using the $k_t$ jet algorithm. Events with four jets are investigated with angular observables, whereas the masses of jets or hemispheres are used as observables for events with two jets. A first selection of events is made with a cut for the jet algorithm. The jets are ordered in energy, thus the first jet refers to the hardest. For some of the observables additional cuts are used:

[3] In OPAL particles with a lifetime smaller than 300 ps are decaying. This is compatible with the default values for the lifetimes of both Monte Carlo generators, Herwig++ and Pythia8, verified by explicitly checking the lifetimes of unstable particles.

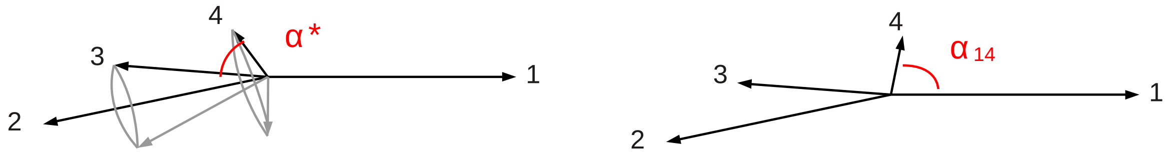


Figure 6.3: The sketch on the left shows the observable $\alpha^*$ and the one on the right shows the angle between the first and fourth jet $\alpha_{14}$.

| Observable | Jets | Cuts | | |
|---|---|---|---|---|
| $\alpha_{14}$ | 4 | Jet Algorithm Cut | and | $\alpha_{12/13} > 2\pi/3$, $\alpha_{23} < \pi/6$ |
| | | | or | $E_4 < E_{\text{tot}}/10$, $\alpha_{23} < \pi/8$ |
| $\alpha^*$ | 4 | Jet Algorithm Cut | and | $\alpha_{12/13} > 2\pi/3$, $\alpha_{23} < \pi/6$, $\alpha_{24} < \pi/2$ |
| | | | or | $E_4 < E_{\text{tot}}/10$, $\alpha_{23} < \pi/8$, $\alpha_{24} < \pi/2$ |
| $M_L^2/M_H^2$ | 2 | Jet Algorithm Cut | and | $y_{3\to4} > y_{2\to3}/2$ |

Table 6.1: The table denotes the different observables, the number of jets the events are clustered in and the associated cuts used in the analyses.

- $\alpha_{12} > 2\pi/3$ and $\alpha_{13} > 2\pi/3$ to achieve that the first and second jet and the first and third jet respectively are back-to-back. Since the values for the two cuts are always the same it will be referred to as $\alpha_{12/13}$ in the following.
- $\alpha_{23} < \pi/8$ or $\pi/6$ to achieve that the second and third jet are collinear.
- $\alpha_{24} < \pi/2$ to achieve that the fourth jet is emitted by the second jet.
- $E_4 < E_{\text{tot}}/10$ to achieve that the fourth jet is soft.
- $y_{3\to4} > y_{2\to3}/2$ with the $3 \to 4$ and $2 \to 3$ clustering scales $y_{3\to4}$ and $y_{2\to3}$ to force a "compressed" scale hierarchy to be more sensitive to the ordering condition.

The starting points are the observables $\alpha^*$ proposed in Ref. [25], $\alpha_{14}$ and $M_L^2/M_H^2$ proposed in Sec. 11.3 of Ref. [43]. The former two, $\alpha^*$ and $\alpha_{14}$, are designed to be sensitive to the coherent emission of a soft fourth jet from a three-parton state. The difference in opening angles $\alpha^*$ was already introduced in Sec. 6.2. For this observable and for the angle between the first and fourth jet, $\alpha_{14}$, as well, the events are clustered into exclusive or inclusive[4] four-jet states. Similar cuts as for $\alpha^*$ are used for $\alpha_{14}$ as well, except that no restriction on the angle of the fourth jet is implied. This results in event topologies as sketched on the right side of Fig. 6.3. The ratio of jet or hemisphere masses $M_L^2/M_H^2$, defined as the invariant mass squared of the lighter jet divided by the invariant mass squared of the heavier jet, is sensitive to the effective description of $1 \to 3$ splittings, as will be discussed in Sec. 6.4.

For all observables the percentage of events, also referred to as event rates, which passed the cuts for this observable is investigated as well. Tab. 6.1 provides an overview of the observables and associated cuts. Two different choices for the cuts on angles and energy are included whereof one will be chosen in the following analyses.

[4]Exclusive means exactly this and only this state, defined at a certain resolution scale. Inclusive means this state, plus "everything else", defined at a certain resolution scale.

| Analysis 1 $y_{\text{cut}}$ | Analysis 2 $y_{3\to4,\text{cut}}$ | Analysis 3 $p_t^{\text{min}}$ in GeV | Cuts for all Analysis | | |
|---|---|---|---|---|---|
| 0.0035 | 0.0035 | 1.6 | | $\alpha_{12/13} > 2\pi/3$ | $\alpha_{23} < \pi/6$ |
| 0.0035 | 0.0035 | 1.6 | $E_4 < E_{\text{tot}}/10$ | | $\alpha_{23} < \pi/8$ |
| 0.0040 | 0.0040 | 1.8 | | $\alpha_{12/13} > 2\pi/3$ | $\alpha_{23} < \pi/6$ |
| 0.0040 | 0.0040 | 1.8 | $E_4 < E_{\text{tot}}/10$ | | $\alpha_{23} < \pi/8$ |
| 0.0045 | 0.0045 | 2.0 | | $\alpha_{12/13} > 2\pi/3$ | $\alpha_{23} < \pi/6$ |
| 0.0045 | 0.0045 | 2.0 | $E_4 < E_{\text{tot}}/10$ | | $\alpha_{23} < \pi/8$ |
| 0.0050 | 0.0050 | 2.2 | | $\alpha_{12/13} > 2\pi/3$ | $\alpha_{23} < \pi/6$ |
| 0.0050 | 0.0050 | 2.2 | $E_4 < E_{\text{tot}}/10$ | | $\alpha_{23} < \pi/8$ |
| 0.0055 | 0.0055 | 2.4 | | $\alpha_{12/13} > 2\pi/3$ | $\alpha_{23} < \pi/6$ |
| 0.0055 | 0.0055 | 2.4 | $E_4 < E_{\text{tot}}/10$ | | $\alpha_{23} < \pi/8$ |
| 0.0060 | 0.0060 | 2.6 | | $\alpha_{12/13} > 2\pi/3$ | $\alpha_{23} < \pi/6$ |
| 0.0060 | 0.0060 | 2.6 | $E_4 < E_{\text{tot}}/10$ | | $\alpha_{23} < \pi/8$ |
| 0.0065 | 0.0065 | 2.8 | | $\alpha_{12/13} > 2\pi/3$ | $\alpha_{23} < \pi/6$ |
| 0.0065 | 0.0065 | 2.8 | $E_4 < E_{\text{tot}}/10$ | | $\alpha_{23} < \pi/8$ |

Table 6.2: Definition of the different sets of cuts for analysis 1, 2 and 3. The first three columns list the cutoff scales for the jet algorithms used in the respective analysis.

### 6.3.2 Analysis 1: $k_t$ Algorithm with $y_{\text{cut}}$

For this analysis the $k_t$ algorithm for $e^+e^-$ collisions with different dimensionless cutoff distances $y_{\text{cut}}$ is used. The events are clustered into jets for a specific scale $y_{\text{cut}}$ and rejected if the number of jets in the event is not four, leading to exclusive four-jet states at the resolution scale $y_{\text{cut}}$. For calculating the mass ratio the chosen events are clustered back into two jets. Tab. 6.2 lists the different cutoff distances together with the two choices of cuts on angles and energy for the angular observables. Since the results of this analysis are similar to the ones of the second analysis, the discussion can be found in the next section.

### 6.3.3 Analysis 2: $k_t$ Algorithm with $y_{3\to4,\text{cut}}$

This analysis follows the analysis in Sec. 11.3 of Ref. [43] and uses the $k_t$ algorithm for $e^+e^-$ collisions. The $3 \to 4$ clustering scale $y_{3\to4}$ is required to be higher than a specific value $y_{3\to4,\text{cut}}$ where the latter is varied in the analysis. Events not rejected by this criterion are clustered either into four jets for the angular observables or into two jets for the mass ratio. The same cuts as for the first analysis are used, they can be found in Tab. 6.2. On the basis of this procedure inclusive two-jet and four-jet states are obtained at the resolution scale $y_{3\to4,\text{cut}}$.

The only noteworthy difference between the analysis in Sec. 6.3.2, using exclusive four-jet states, and the analysis of this section is the number of events passing the resolution cut of the jet algorithm. Since this number is slightly higher for the second analysis with the resolution cut $y_{3\to4,\text{cut}}$, this analysis is chosen. Therefore only the plots obtained by the second analysis are shown here since no appreciable differences in the distributions of the observables appear. An important issue due to the limited amount of data that will be analyzed, is the remaining statistics of the event samples after applying all cuts. The

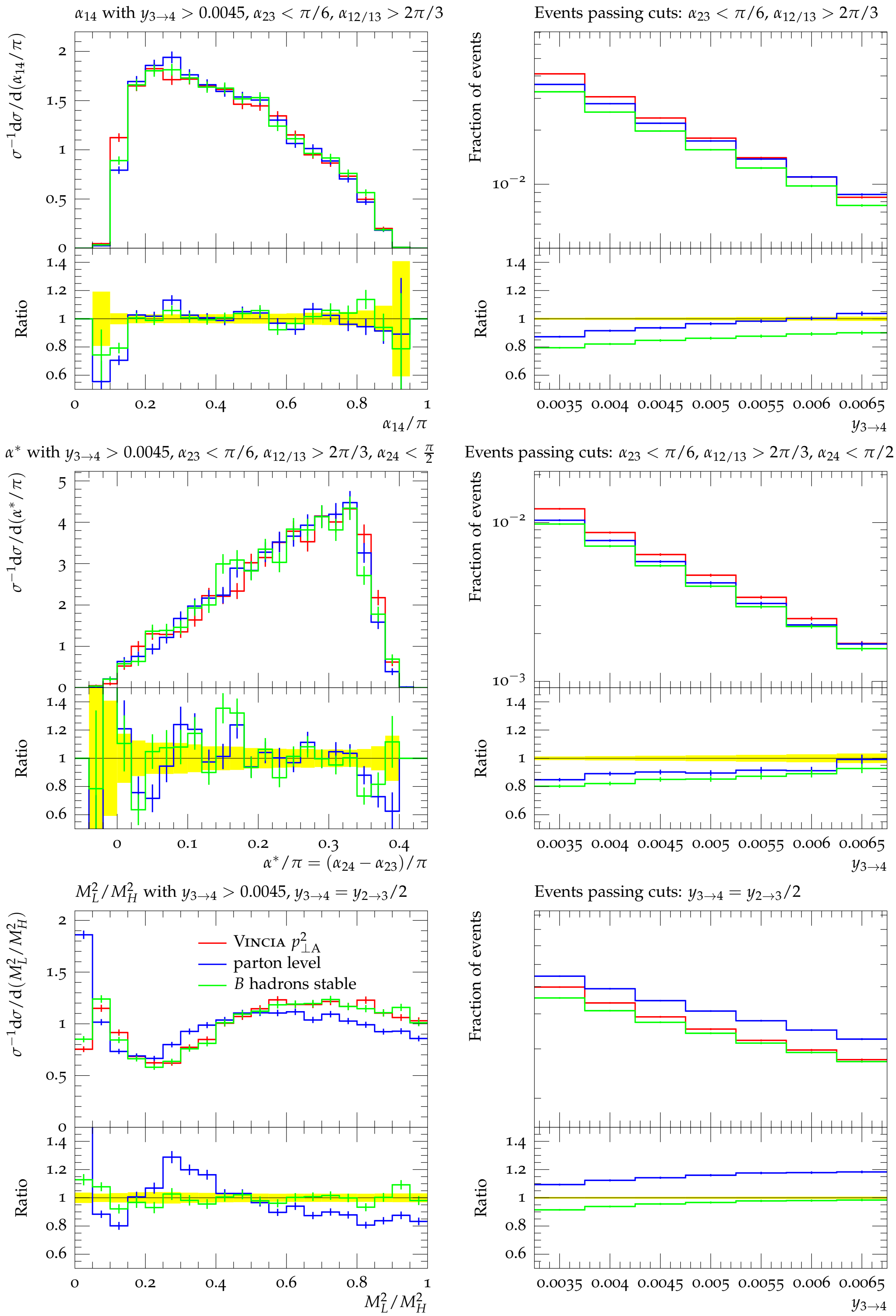


Figure 6.4: Results of analysis 2 for the $p^2_{\perp A}$-ordered shower of VINCIA: The left plots show the normalized distributions of the angular observables, $\alpha_{14}$ and $\alpha^*$, and the mass ratio, $M_L^2/M_H^2$. On the right the fraction of events that passed the cuts, used to obtain the observable, are plotted for different $y_{3\to4,\text{cut}}$. A comparison between the observables on hadron level (red), parton level (blue) and without decays of $B$ hadrons (green) is shown. The ratio plots show the deviation with respect to the observable on hadron level and the error bars are the statistical Monte Carlo errors.

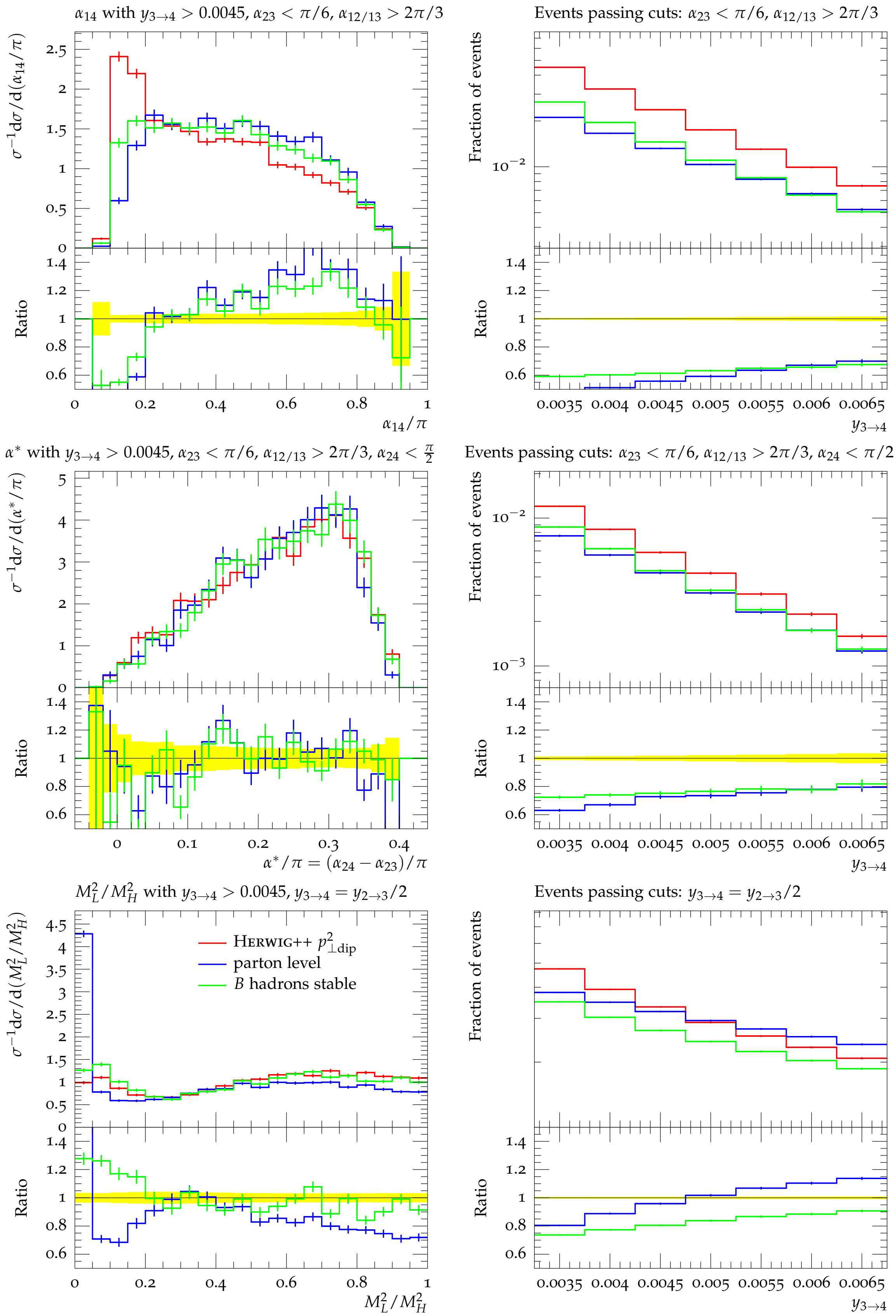


Figure 6.5: Results of analysis 2 for the $p_{\perp\mathrm{dip}}^2$-ordered dipole shower of HERWIG++: The left plots show the normalized distributions of the angular observables, $\alpha_{14}$ and $\alpha^*$, and the mass ratio, $M_L^2/M_H^2$. On the right the fraction of events that passed the cuts, used to obtain the observable, are plotted for different $y_{3\to4,\mathrm{cut}}$. A comparison between the observables on hadron level (red), parton level (blue) and without decays of $B$ hadrons (green) is shown. The ratio plots show the deviation with respect to the observable on hadron level and the error bars are the statistical Monte Carlo errors.

tighter cuts, $E_4 < E_{\text{tot}}/10$ and $\alpha_{23} < \pi/8$, reject about four to five times more events than the looser cuts, $\alpha_{12/13} > 2\pi/3$ and $\alpha_{23} < \pi/6$. Hence the latter ones are the appropriate choice to gain more statistics and will be used for all further investigations.

As an example for the PYTHIA8 / VINCIA event generator group, Fig. 6.4 shows the result of the analysis for the $p_{\perp\text{A}}$-ordered shower of VINCIA. On the left the normalized distributions of the angular observables and the mass ratio $M_L^2/M_H^2$ are shown. The plots on the right show the fraction of events that passed the cuts for the observable. The same plots can be found in Fig. 6.5 for the $p_{\perp\text{dip}}$-ordered dipole shower of HERWIG++. The results presented in the following can be generalized to the other shower models.

For VINCIA small corrections due to hadronization and $B$ decays show up in the event rates with a maximum amount of about 20%. The possibility to minimize hadronization effects on the mass ratio are limited due to the massless partons at the end of the shower. If a jet consists of only one massless parton its invariant mass is zero leading to the enhancement at small values for the mass ratio. Therefore, a correction with about a factor 1/2 due to hadronization occurs for the first bin in the normalized distribution of the mass ratio. For the angular observables the hadronization correction gets smaller when increasing the value of $y_{3\to4,\text{cut}}$. The event rates on the other hand decrease when using a higher cutoff. Hence, picking a specific value for $y_{3\to4,\text{cut}}$ is a compromise between the need for enough statistics and minimizing the non-perturbative influences. The resolution scale of the jet algorithm is chosen to be $y_{3\to4} > 0.0045$, corresponding to about 6 GeV.

For HERWIG++ higher effects due to the hadronization show up in the event rates of the angular observables. These effects range from about 20% up to 50%. In order to decrease these disruptive influences a very high cut on $y_{3\to4}$ would be required. Since this would reject too many events it is not possible to get only small effects of hadronization and $B$ decays for HERWIG++ on the event rates. As for VINCIA, a large hadronization correction occurs in the first bin in the normalized distribution of the mass ratio. Furthermore the normalized distribution of $\alpha_{14}$ shows a very large hadronization effect for small values, common to both HERWIG++ showers, the angular-ordered parton shower and the dipole shower with both ordering variables. The power of this enhancement depends on the values of the parameters of the cluster hadronization model. Since these parameters are going to be changed within the tuning process, this analysis is repeated after the tuning and the main changes in the results are presented in Sec. 7.2.1.

### 6.3.4 Analysis 3: Anti-$k_t$ Algorithm

For this analysis the generalized $k_t$ algorithm for $e^+e^-$ collisions is used for inclusive jets where the parameters of the algorithm are chosen to be $p = -1$ and $R = \pi/16$. Thus the distance measures are

$$d_{ij} = \min\left(E_i^{-2}, E_j^{-2}\right) \frac{1 - \cos\theta_{ij}}{1 - \cos(\pi/16)} \tag{6.10}$$

$$d_{iB} = E_i^{-2} \ . \tag{6.11}$$

Due to the negative energy exponent this algorithm is also called anti-$k_t$ jet algorithm. All particle pairs $i$ and $j$ with an opening angle $\theta_{ij}$ smaller than $\pi/16$ are recombined and the opening half-angle of the resulting jets is $\pi/16$. As resolution criterion for this algorithm a cut on the transverse momentum of the jets is used. Hence jets with a transverse momentum higher than $p_t^{\min}$ are taken into account. Events that do not consist of exactly

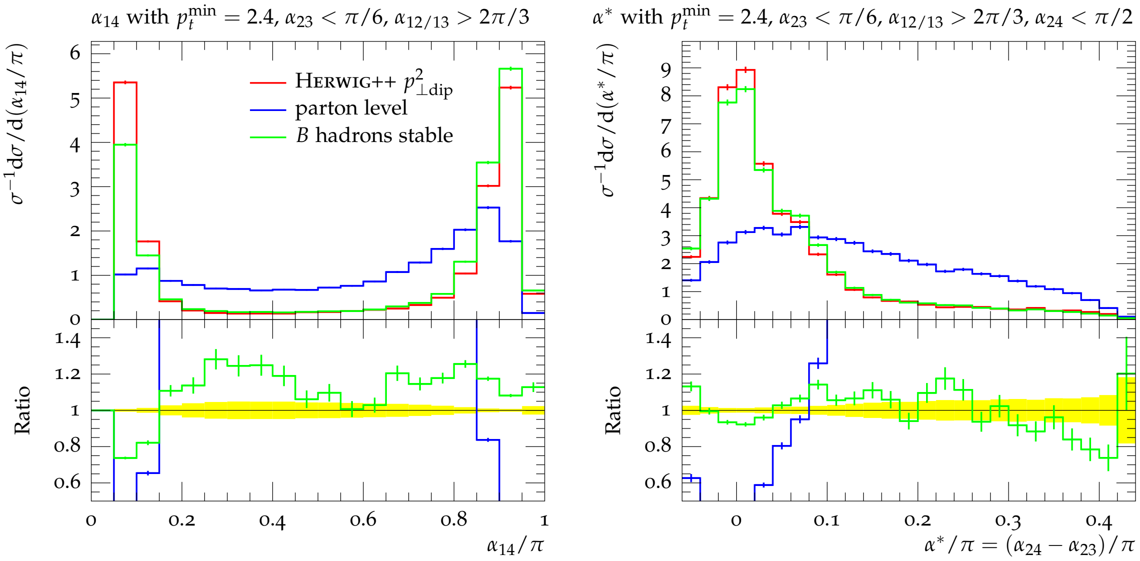


Figure 6.6: Results of analysis 3 for the $p^2_{\perp\mathrm{dip}}$-ordered dipole shower of HERWIG++: The plots show the normalized distributions of the angular observables $\alpha_{14}$ and $\alpha^*$, A comparison between the observables on hadron level (red), parton level (blue) and without decays of $B$ hadrons (green) is shown. The ratio plots show the deviation with respect to the observable on hadron level and the error bars are the statistical Monte Carlo errors.

four jets are rejected. Tab. 6.2 lists the cutoffs $p_t^{\mathrm{min}}$ together with the two choices of cuts on angles and energy for the observables.

Fig. 6.6 shows the normalized distributions of the angular observables $\alpha_{14}$ and $\alpha^*$ for the $p_{\perp\mathrm{dip}}$-ordered dipole shower of HERWIG++. For both distributions large differences between the results on hadron and parton level show up. This hadronization influence does not depend on the cuts and hence can not be minimized for this jet algorithm. The conclusions drawn for the generalized $k_t$ algorithm with $p = -1$ hold for the other shower models as well. Thus this algorithm will not be used for further analysis due to the smearing after hadronization and decays.

### 6.3.5 Conclusions

The aim of this section was a precise mapping of the hadronic final state to the partonic system after the shower termination. By using the $k_t$ jet algorithm with a resolution criterion of $y_{3\to4} > 0.0045$ a compromise between the need for enough statistics for the data analysis and minimizing disruptive effects of hadronization and $B$ decays was found. For VINCIA and PYTHIA8 this value for the jet algorithm cutoff works very well for the angular observables, leaving only small effects due to hadronization. For HERWIG++ slightly larger hadronization effects show up in the event rates for all observables. Furthermore an enhancement for small values of $\alpha_{14}$ occurs which can be reduced partly throughout the tuning process. Thus, Sec. 7.2.1 deals with the influence of hadronization as well. For all shower models a large correction due to hadronization shows up in the first bin of the mass ratio. Massless partons at the end of the shower can lead to massless jets and therefore to the population of very small values of the mass ratio. To conclude, the observables, especially the ratio of jet masses, show sensitivity to non-perturbative effects which cannot be reduced completely. As cuts on the angles between the jets for the angular observables the looser ones, $\alpha_{12/13} > 2\pi/3$ and $\alpha_{23} < \pi/6$, will be used since much more events are rejected when using the tighter cuts.

| Observable | Jets | Cuts |
|---|---|---|
| $\alpha^*$ | 4 | $y_{3\to 4} > 0.0045,\quad \alpha_{12/13} > 2\pi/3,\quad \alpha_{23} < \pi/6,\quad \alpha_{24} < \pi/2$ |
| $\alpha_{14}$ | 4 | $y_{3\to 4} > 0.0045,\quad \alpha_{12/13} > 2\pi/3,\quad \alpha_{23} < \pi/6$ |
| $M_L^2/M_H^2$ | 2 | $y_{3\to 4} > 0.0045,\quad y_{3\to 4} > y_{2\to 3}/2$ |

Table 6.3: Observables, number of jets the event is clustered in and associated cuts used in the analysis.

## 6.4 Asymmetries

After settling the resolution criterion for the jet algorithm and the cuts used to obtain the observables in the last section, this analysis compares the different shower models in terms of the observables listed in Tab. 6.3. An important aim is to find ways to compare the shower models efficiently, for instance by reducing the observables to easier variables allowing clear statements about the emission properties of the shower. As in the previous section $5 \cdot 10^5$ hadronic events are used to take statistical uncertainties into account.

To get a clear and simple observable discriminating between the showers the asymmetry of the histograms with respect to a vertical axis $x_0$ through a certain observable value is used. The asymmetry is used for all observables and here defined as

$$\frac{N_{\text{left}}}{N_{\text{right}}} = \frac{\sum\limits_{x<x_0} y(x)}{\sum\limits_{x>x_0} y(x)} \tag{6.12}$$

with the observable $x$ and the histogram entries $y(x)$. The axis $x_0$ is defined around the intersection of the curves for the different showers. In analogy other ratios are build for the angle $\alpha_{14}$, where two different regions of a histogram are divided by each other:

$$AS(x) = \frac{\sum\limits_{x_1<x<x_2} y(x)}{\sum\limits_{x_3<x<x_4} y(x)}\ . \tag{6.13}$$

The asymmetries can simply be calculated by summing and dividing the histogram entries of the normalized distribution. The statistical errors are calculated with sums in quadrature. In the following the six shower models, introduced in Sec. 5.2, will be compared in terms of the observables listed in Tab. 6.3. A more detailed comparison of the Monte Carlo event generators with OPAL data will follow in Chap. 9.

### Difference in Opening Angles: $\alpha^*$

The normalized distribution of the difference in opening angles $\alpha^*$ and the corresponding asymmetry are shown in Fig. 6.7. Due to the additional cut on the angle between the second and fourth jet, $\alpha_{24}$, the event rate decreases, for instance in comparison with $\alpha_{14}$, and as a result the statistical errors grow. Therefore the power to tell the different models apart is limited for this observable. The asymmetry of $\alpha^*$, as shown on the right in Fig. 6.7, suggests that a marginal possibility to distinguish the shower models exists. However it is not possible to tell the two different ordering variables of VINCIA apart since they lead to nearly the exact same values for the asymmetry. Therefore it is more appropriate to use an observable for which less cuts are necessary to tell the theory models apart.

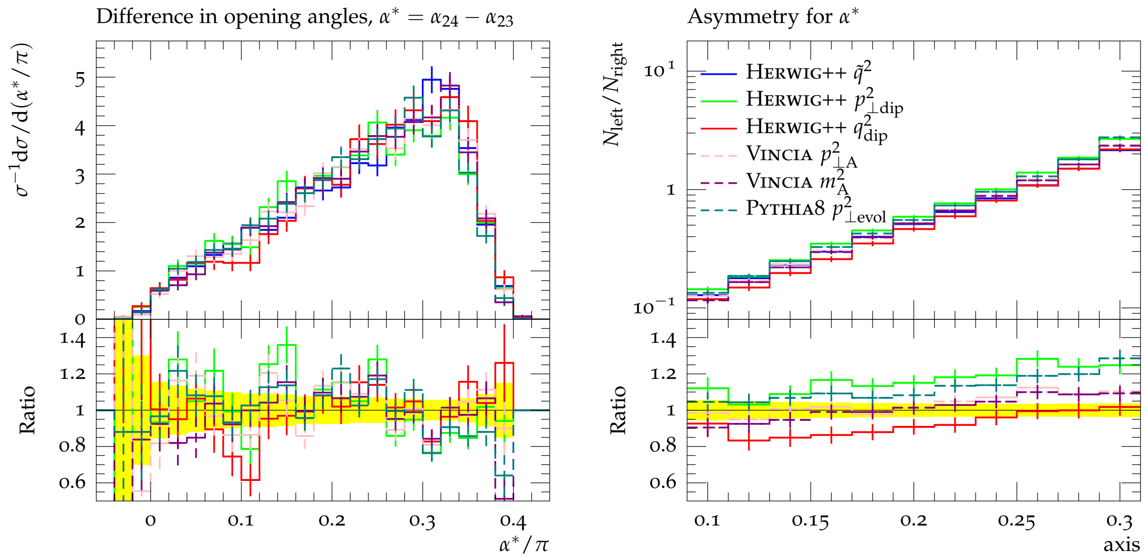


Figure 6.7: The left plot shows the normalized distribution of the difference in opening angles $\alpha^*$ and its asymmetry according to Eq. (6.12) for different axis is shown in the right plot. The following description of line style and colour holds from now on for all plots in this section. The solid curves refer to the Herwig++ showers, the angular-ordered default shower in blue, the $p^2_{\perp\mathrm{dip}}$-ordered in green and the $q^2_{\mathrm{dip}}$-ordered dipole shower in red respectively. The dashed lines refer to the Vincia shower with mass-ordering in violet and $p^2_{\perp\mathrm{A}}$-ordering in pink and to the Pythia8 shower in teal. The ratio plots show the deviation of the showers with respect to the Herwig++ angular-ordered default shower. The error bars are the statistical Monte Carlo errors.

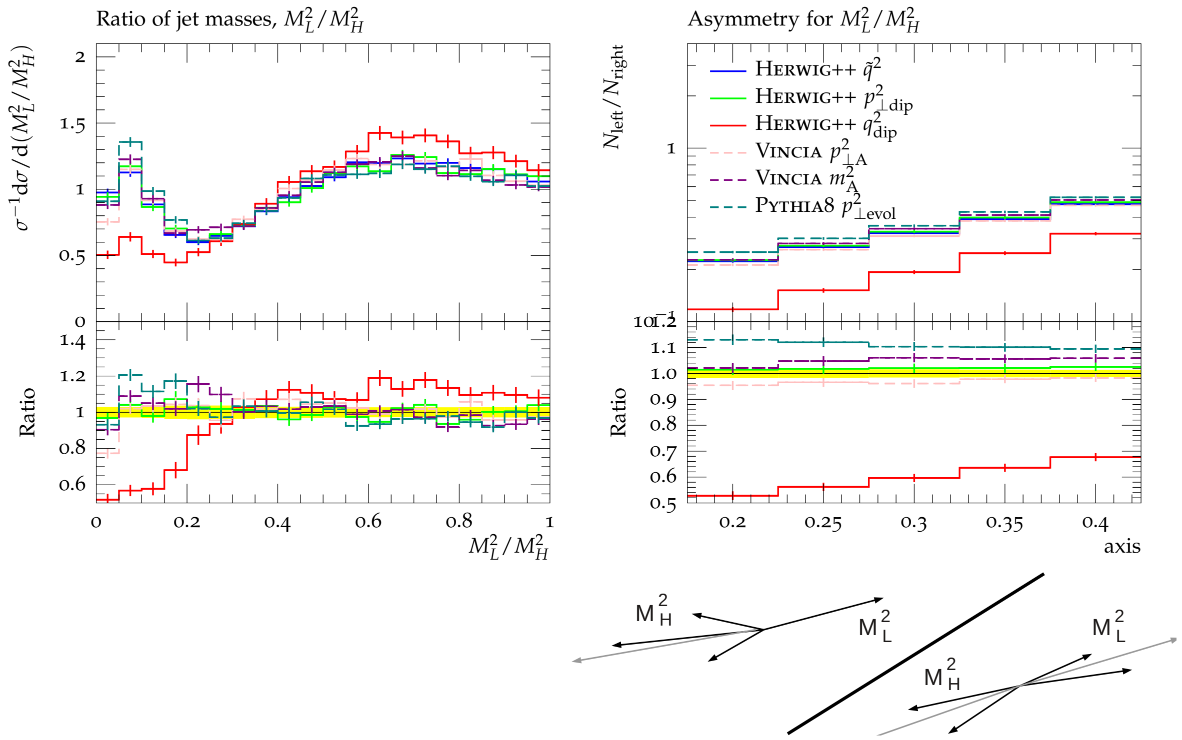


Figure 6.8: The left plot shows the normalized distribution of the mass ratio $M_L^2/M_H^2$ and its asymmetry according to Eq. (6.12) for different axes is shown in the right plot. The sketch illustrates the meaning of the asymmetry in terms of the amount of different event topologies.

| | | Central/Towards | Central/Away | Towards/Away |
|---|---|---|---|---|
| # | Central Region | Towards Region | Away Region | Towards region |
| 1 | $0.4 < \alpha_{14}/\pi < 0.6$ | $\alpha_{14}/\pi < 0.3$ | $\alpha_{14}/\pi > 0.6$ | $\alpha_{14}/\pi < 0.3$ |
| 2 | $0.4 < \alpha_{14}/\pi < 0.6$ | $\alpha_{14}/\pi < 0.2$ | $\alpha_{14}/\pi > 0.7$ | $\alpha_{14}/\pi < 0.3$ |
| 3 | $0.4 < \alpha_{14}/\pi < 0.6$ | $\alpha_{14}/\pi < 0.4$ | $\alpha_{14}/\pi > 0.8$ | $\alpha_{14}/\pi < 0.3$ |
| 4 | $0.45 < \alpha_{14}/\pi < 0.55$ | $\alpha_{14}/\pi < 0.3$ | $\alpha_{14}/\pi > 0.6$ | $\alpha_{14}/\pi < 0.2$ |
| 5 | $0.45 < \alpha_{14}/\pi < 0.55$ | $\alpha_{14}/\pi < 0.2$ | $\alpha_{14}/\pi > 0.7$ | $\alpha_{14}/\pi < 0.2$ |
| 6 | $0.45 < \alpha_{14}/\pi < 0.55$ | $\alpha_{14}/\pi < 0.4$ | $\alpha_{14}/\pi > 0.8$ | $\alpha_{14}/\pi < 0.2$ |
| 7 | $0.35 < \alpha_{14}/\pi < 0.65$ | $\alpha_{14}/\pi < 0.3$ | $\alpha_{14}/\pi > 0.6$ | $\alpha_{14}/\pi < 0.4$ |
| 8 | $0.35 < \alpha_{14}/\pi < 0.65$ | $\alpha_{14}/\pi < 0.2$ | $\alpha_{14}/\pi > 0.7$ | $\alpha_{14}/\pi < 0.4$ |
| 9 | $0.35 < \alpha_{14}/\pi < 0.65$ | $\alpha_{14}/\pi < 0.4$ | $\alpha_{14}/\pi > 0.8$ | $\alpha_{14}/\pi < 0.4$ |

Table 6.4: Definition of the different regions for the asymmetry of $\alpha_{14}$. Columns two to five specific the limits for the regions and the first column contains the numbering. The ratio of the central to towards region is build with the second and third column, central to away with the second and fourth and towards to away uses the fourth and fifth column.

### Mass Ratio: $M_L^2/M_H^2$

The normalized distribution of the mass ratio $M_L^2/M_H^2$ is shown on the left side in Fig. 6.8. The ratio plot for the normalized distribution on the left, showing the deviation of the shower models with respect to Herwig++ with angular ordering, confirms that the different theory models give different predictions for this observable. On the right the asymmetry is shown where the different shower models give again different results for the ratio of small to high values of the mass ratio.

The sketch below the plots illustrate the event topologies resulting in small and high ratio of jet masses. If the masses are distributed very asymmetrically, leading to one very high and one very small mass, the clustering of the next jets happens within the same hemisphere. To sketch this the heavier jet in the original topology is coloured gray. If the event gets clustered with a smaller resolution the heavier jet would be clustered into more jets, coloured in black. For higher values of the mass ratio the events are more symmetric and the clustering of the next jets would happen on opposite sides. Therefore the asymmetry shown on the right side in Fig. 6.8 corresponds to the relative amount of same-side to opposite-side events. The virtuality-ordered shower of Herwig++ produces much less events with small mass ratios compared to the angular-ordered shower. A less strong effect is visible for Vincia with $p_{\perp\mathrm{A}}$-ordering. Pythia8 tends to do the opposite, produce more events where the clustering happens inside one jet, compared to the angular-ordered shower of Herwig++.

### Angle between first and fourth Jet: $\alpha_{14}$

In order to predict the amounts of a specific kind of radiation, for instance collinear or wide-angle emission, the values of the angle between the first and fourth jet, $\alpha_{14}$, are divided into three different regions. The so-called towards region includes small values of $\alpha_{14}$ and thus events where the fourth jet is collinear to the first jet. The central region is defined in a way that it contains events where the fourth jet origins in a wide-angle emission and is hence about perpendicular to the first jet. The last region is the so-called

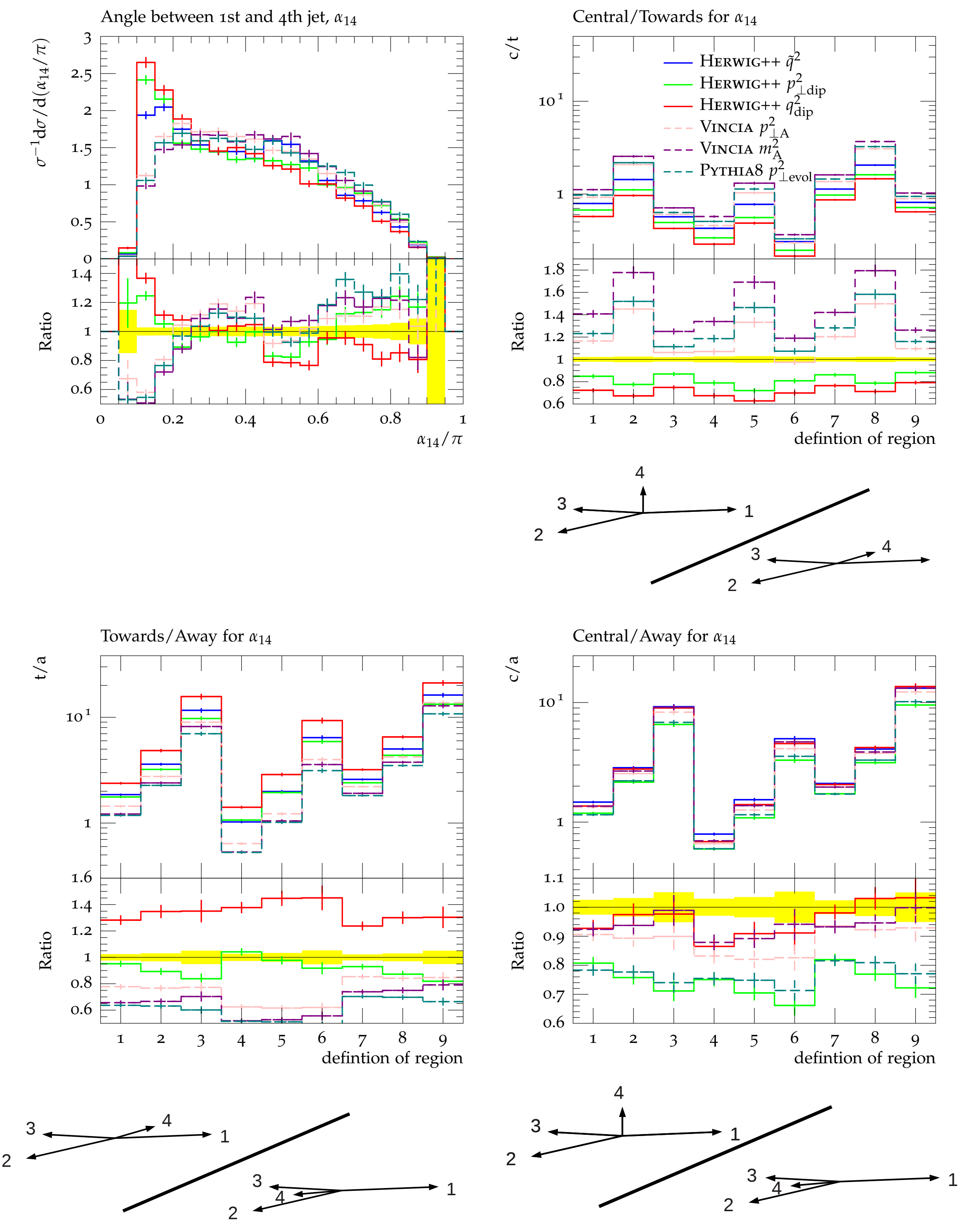


Figure 6.9: The upper left plot shows the normalized distribution of the angle $\alpha_{14}$ and the upper right plot the ratio of the central to towards region according to Eq. (6.13). The lower plots show the central over away and towards over away region. The different definitions used for these asymmetries can be found in Tab. 6.4. The sketches below the plots illustrate the meaning of the regions.

away region and characterizes events where the fourth jet lies back-to-back to the first jet. The various limits of these regions are defined in Tab. 6.4. These regions are used to build several asymmetries according to Eq. (6.13).

The upper left plot in Fig. 6.9 shows the normalized distribution of $\alpha_{14}$. The ratio plot, showing the deviation of the shower models with respect to the angular-ordered shower of Herwig++, confirms that the different theory models give different predictions for this observable. This is verified by the additional plots in Fig. 6.9, showing the different ratios according to Eq. (6.13). All asymmetries show a high sensitivity to the shower model used for the prediction. The sketches below the plots of the asymmetries illustrate their meaning, for instance the central over towards region predicts the amount of wide-angle radiation with respect to the emissions where the fourth jet is collinear to the first jet. This asymmetry states that all Herwig++ showers produce a smaller ratio of wide-angle to collinear emission compared with Pythia8 and Vincia. The differences between the showers reach up to a factor 2 for the different ratios. Since the enhancement for small values of $\alpha_{14}$ due to hadronization effects showed up for the Herwig++ showers the central over away region can be used to not take the enhancement into account. This ratio is shown in the lower right plot in Fig. 6.9. The mass-ordered shower of Vincia and the virtuality-ordered shower of Herwig++ produce about the same amount of radiation here and also Pythia8 and the $p_{\perp\mathrm{dip}}$-ordered dipole shower of Herwig++ give similar predictions. In total about up to 30% deviation between the different shower models can be found for this asymmetry. The summarized result of the plots for $\alpha_{14}$ includes the possibility to tell the different shower models apart within the statistical errors.

## 6.5 Experimental Resolution

In order to take the experimental detector resolution for measuring angles of jets into account a resolution of $\delta\phi$ for the azimuth and polar angles of the jets is supposed. The analysis is performed exemplarily for the angle between the first and fourth jet, $\alpha_{14}$, which can be expressed in terms of azimuth and polar angles $\theta_i$ and $\varphi_i$ of the first and fourth jet as

$$\cos\alpha_{14} = \frac{\vec{p}_1 \cdot \vec{p}_4}{|\vec{p}_1| \cdot |\vec{p}_4|} \quad \text{with} \quad \vec{p}_i = |\vec{p}_i| \begin{pmatrix} \sin\theta_i \cos\varphi_i \\ \sin\theta_i \sin\varphi_i \\ \cos\theta_i \end{pmatrix} \tag{6.14}$$

$$\Rightarrow \quad \alpha_{14} = \arccos\left(\sin\theta_1 \sin\theta_4 \cos(\varphi_1 - \varphi_4) + \cos\theta_1 \cos\theta_2\right) \ . \tag{6.15}$$

$\alpha_{14}$ is smeared with a Gaussian distribution for different values of the resolution $\delta\phi$ where the uncertainty for $\alpha_{14}$ is calculated via propagation of uncertainty. In order to rather overestimate the effect of the experimental resolution the uncertainties on azimuth and polar angles are not summed in quadrature, but summed with the absolute value,

$$\delta\alpha_{14} = \sum_{i=1,4} \left( \left| \frac{\partial\alpha_{14}}{\partial\theta_i} \right| + \left| \frac{\partial\alpha_{14}}{\partial\varphi_i} \right| \right) \delta\phi \tag{6.16}$$

$$\begin{aligned} &= \frac{\delta\phi}{\sin\alpha_{14}} \Big( \left|\cos\theta_1 \sin\theta_4 \cos(\varphi_1 - \varphi_4) - \sin\theta_1 \cos\theta_2\right| \\ &\qquad + \left|\sin\theta_1 \cos\theta_4 \cos(\varphi_1 - \varphi_4) - \cos\theta_1 \sin\theta_2\right| \\ &\qquad + \left|\sin\theta_1 \sin\theta_4 \sin(\varphi_1 - \varphi_4) + \cos\theta_1 \cos\theta_2\right| \\ &\qquad + \left|-\sin\theta_1 \sin\theta_4 \sin(\varphi_1 - \varphi_4) + \cos\theta_1 \cos\theta_2\right| \Big) \ . \end{aligned} \tag{6.17}$$

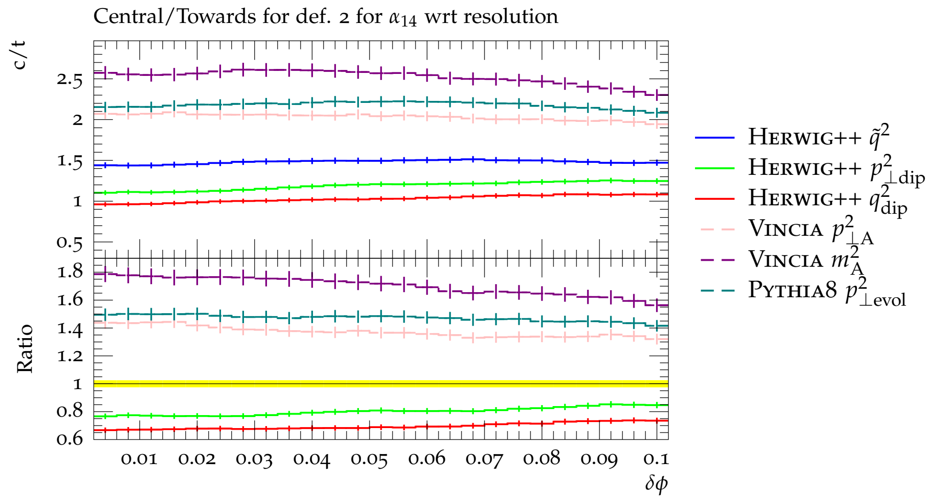


Figure 6.10: The plot shows the asymmetry of $\alpha_{14}$ for the second definition of the regions (see Tab. 6.4) with respect to the resolution $\delta\phi$. To obtain this plot $\alpha_{14}$ is smeared with a Gaussian distribution with resolution $\delta\phi$.

Fig. 6.10 shows the results: The asymmetry of $\alpha_{14}$ according to Eq. (6.13) for the second definition of the regions (see Tab. 6.4) is shown with respect to the resolution $\delta\phi$. Even for a value of 0.1 for the resolution[5] it is still possible to distinguish between the showers within the limits of the statistical Monte Carlo errors.

## 6.6 Conclusions

In the previous sections the influence of hadronization and $B$ decays has been narrowed as well as possible by choosing the right resolution scale for the jet algorithm and applying different cuts. At the same time it was necessary to choose scales and cuts not too tight in order to remain with enough statistics. Despite the observables are designed to be sensitive to the parton shower, there is still some sensitivity to non-perturbative effects left. Especially the ratio of jet masses show a large correction due to hadronization for very small values in the predictions of all shower models.

With the help of observables like the angle between jets, $\alpha_{14}$, and the ratio of jet masses, $M_L^2/M_H^2$, the possibility of telling the different shower models apart within the statistical errors exists. Since the aim is a comparison of predictions of the theory models with OPAL data the experimental resolution for the measurement of angles has to be taken into account.

[5] $\delta\phi = 0.1$ is more than the actual experimental resolution for the OPAL detector.

# 7. Tuning

The observables proposed in the last chapter provide power in telling the different shower models apart. In order to ensure a fair comparison of the models this chapter aims at a description of existing LEP measurements on the same input level by all theory models. Therefore the parameters of the shower algorithm and the non-perturbative hadronization model have to be readjusted. Constraining the free parameters of theoretical models by using existing experimental data is referred to as generator tuning. The same LEP data set for all shower models will be used here. Thus, it is possible to make a statement if each shower model is able to describe the data with the same quality.

As in the previous chapter the focus lies on the pure shower properties and on comparing the shower models as directly as possible. Hence higher order matching[1] is used throughout the tuning and VINCIA is used solely with strong ordering.

In order to tune HERWIG++ or PYTHIA8 and VINCIA respectively the PROFESSOR Monte Carlo tuning system is used, see Sec. 5.6 for a short description of the program and the basic tuning process. In the following Sec. 7.1 the different parameters and the observables used in the tuning are described. The results of the tuning process are presented in Sec. 7.2.

## 7.1 Input for the Tuning

This section deals with the basic elements for the tuning. The free parameters of the shower and hadronization models that will be readjusted are briefly described, followed by the set of observables used for the readjustment. At last an overview of the tuning process is given.

### 7.1.1 Parameters

The free parameters of the shower models can be found in Tab. 5.1 for the HERWIG++ shower algorithms and in Tab. 5.2 for PYTHIA8 and VINCIA. VINCIA offers the possibility to use other types of variables for the shower cutoff, such as a cutoff in the evolution

[1] Correction of the first real emission in the angular-ordered shower, LO accuracy for the dipole shower of HERWIG++ and the default matching in PYTHIA8 for VINCIA and PYTHIA8.

variable of the PYTHIA8 shower $p^2_{\perp\mathrm{evol}}$, but here for the $p^2_{\perp\mathrm{A}}$- as well as for the mass-ordered shower a cutoff in the transverse momentum $p^2_{\perp\mathrm{A}}$ is chosen.

The main free parameters of the HERWIG++ cluster hadronization model are listed Tab. 5.3. A more detailed discussion of these parameters can be found there. The parameters of the Lund string model of PYTHIA8, that will be used in the tuning, are denoted in Tab. 5.4. For a more detailed discussion of the parameters see the respective section.

### 7.1.2 Observables

To include a wide range of observables different groups are used: Event shapes, identified particle spectra, jet rates, mean particle multiplicities and $b$ quark fragmentation functions, provided by the ALEPH [44,45], DELPHI [46] and OPAL [47] experiments and by the Particle Data Group PDG [48]. The observables and their weights can be found in Tabs. A.1-A.5 in Appendix A. Observables, such as mean multiplicities, with only one bin are given a higher weight to increase the possibility of a good description.

Two tunes with different observable weights are performed of which the first[2] uses all observables and is hence very extensive. In order to put the emphasis on event shapes and jet rates, the most important observables in the context of studies of the structure of multi-jet events, a second tune[3] was performed. Multiplicities are given zero weight in this tune and event shapes and jet rates are significantly weighted up.

### 7.1.3 Tuning Procedure

The amount of coefficients for the interpolation polynomial, which defines the minimal number of Monte Carlo runs that has to be performed for the tuning, increases strongly with the number of parameters, see Eq. (5.28) and Sec. 5.6. Therefore the parameters of HERWIG++ that exist in copies for the different flavours are varied with the same value for all flavours in order to save time and computing capacity. In the context of a study of coherence properties the contributions of specific flavours are also only of minor interest.

The goodness of fit, see Sec. 5.6, for real Monte Carlo runs is defined as

$$\frac{\chi^2}{N_{\mathrm{dof}}} = \frac{\sum\limits_{\mathcal{O}} w_{\mathcal{O}} \sum\limits_{b\in\mathcal{O}} \left(\mathrm{MC}^{(b)}(\vec{p}) - \mathcal{R}^{(b)}\right)^2 / \Delta^{(b)2}}{\sum\limits_{\mathcal{O}} w_{\mathcal{O}} |b \in \mathcal{O}|} \tag{7.1}$$

and provides information about how well data measurements are described by the predictions of Monte Carlo event generators. Considering an observable with only a single bin, a value smaller than unity corresponds to predictions that lie within the error band of the data.

The default parameter values of the Monte Carlo generators are usually obtained by previous tunes. VINCIA uses a tune called jeppsson5, see Ref. [49], and the parameters of the HERWIG++ dipole shower were obtained in the tune of Ref. [26]. PYTHIA8 uses by default a tune to a wide selection of LEP data within the RIVET and PROFESSOR framework. After performing a first tune with HERWIG++ flat distributions in $\chi^2$ are obtained for two parameters, the soft scale $\mu_{\mathrm{soft},FF}$ and the smearing parameter $\mathrm{Cl}_{\mathrm{smr}}$.

[2]From now on referred to as Tune 1.
[3]From now on referred to as Tune 2.

Therefore $\mathrm{Cl}_{\mathrm{smr}}$ is kept at its default value and $\mu_{\mathrm{soft},FF}$ is set to zero to increase the value of the shower cutoff. This approach leads to slightly smaller values in the goodness of fit values since the minimization works better due to the reduction of the dimensionality of the parameter space.

To get a good description of the Monte Carlo response by the interpolation with Professor, a fourth order polynomial is used. Due to fixing the parameters with flat distributions in $\chi^2$, as explained above, six parameters for each combination of shower and hadronization model are left. The number of coefficients for the polynomial according to Eq. (5.28) is 210, defining the minimal possible number of Monte Carlo runs needed for the tuning. To get reasonable results oversampling of about a factor 3 is performed, leading to 650 Monte Carlo runs with different randomly selected values of the parameters that are tuned. 500 randomly selected runs are then used 300 times to interpolate the generator response. The quality of the interpolation was checked by comparing the $\chi^2$ of the interpolation response with real Monte Carlo runs at certain parameter values. The quality is increased by removing parameter regions where the interpolation did not work sufficiently well. Unfortunately not all bad regions are removed for Herwig++ since the values of some observables are not a smooth function of the gluon mass in the region where the Monte Carlo predictions fit the data well. This is backed by the possibility of new splitting processes for higher gluon masses. 300 run combinations are used again in the tuning step where the goodness of fit is minimized in order to obtain the parameters that describe the observables best. Afterwards real Monte Carlo runs are performed for these slightly different parameter sets and the one that leads to the smallest $\chi^2/N_{\mathrm{dof}}$ value is used for further work.

## 7.2 Results

This section presents the results of the tuning process, starting with a short overview in terms of the total $\chi^2/N_{\mathrm{dof}}$ values for the different shower models. In order to validate the results of the tuning different analysis tools have been applied. The results for the $p^2_{\perp\mathrm{dip}}$-ordered dipole shower are presented as an example for Herwig++ and for the $p^2_{\perp\mathrm{A}}$-ordered shower as an example for Vincia.

**Quality of the Overall Description**

The goodness of fit function per degree of freedom, $\chi^2/N_{\mathrm{dof}}$, is listed in Tab. 7.1 for the different shower models. The previous tunes of Vincia and Pythia8 already describe the existing LEP measurements very well. The description of the LEP data by the angular-ordered shower of Herwig++ without a new tune is fine as well. Therefore only small improvements in the quality of the description of LEP data is achieved. It is noteworthy that this shower model is the only one that describes the mean particle multiplicities better than the other observables. This leads to a smaller value of $\chi^2/N_{\mathrm{dof}}$ for the tune to all observables compared to the tune with emphasis on event shapes and jet rates. For the Herwig++ dipole shower, for ordering in transverse momentum as well as for ordering in virtuality, a great improvement in fitting the LEP data was achieved by the tuning. The goodness of fit values are reduced by factors 3 up to 17. Here, the theory models can be told apart in terms of how well they are able to describe existing LEP measurements. Vincia with ordering in transverse momentum fits the data the best for both tunes, followed by Pythia8 standalone and Vincia with mass-ordering. All LEP measurements use Pythia6 [50] or Jetset [50] to generate Monte Carlo event samples for the detector

| | Default Parameters | | Tuned Parameters | |
|---|---|---|---|---|
| | Tune 1 | Tune 2 | Tune 1 | Tune 2 |
| Herwig++ $\tilde{q}^2$-Ordered Shower | 20.2 | 26.2 | 16.9 | 21.4 |
| Herwig++ $p^2_{\perp\mathrm{dip}}$-Ordered Dipole Shower | 348.5 | 59.4 | 23.0 | 21.9 |
| Herwig++ $q^2_{\mathrm{dip}}$-Ordered Dipole Shower | 358.2 | 109.5 | 25.3 | 17.4 |
| Vincia $p^2_{\perp\mathrm{A}}$-Ordered Shower | 9.1 | 8.0 | 7.0 | 4.4 |
| Vincia $m^2_{\mathrm{A}}$-Ordered Shower | 14.6 | 17.1 | 9.3 | 8.5 |
| Pythia8 $p^2_{\perp\mathrm{evol}}$ Shower | 8.0 | 6.3 | 7.4 | 5.7 |

Table 7.1: The total $\chi^2/N_{\mathrm{dof}}$ values for the different shower models, for the default values values and the best tunes. The first tune uses all observables and the second tune puts the emphasis on the event shapes and jet rates.

correction. Herwig event samples are used as well as a contribution to the systematic uncertainty. Therefore, the experiments claim that the observable distributions are independent of the underlying Monte Carlo generator for the detector corrections within the experimental systematics. Nevertheless, the use of a generator similar to Pythia6 would lead to a better performance and smaller $\chi^2/N_{\mathrm{dof}}$ value than the use of Herwig, if Pythia6 predicts exactly the values of the data and the predictions of Herwig lie within the error bars of the data. Since all three Monte Carlo programs, Pythia6, Pythia8 and Vincia, use the Lund string hadronization model, these generators might gain advantage over Herwig++ in fitting the LEP measurements.

**Goodness of Fit per Observable**

To gain knowledge about the quality of the description of the single observables, Tabs. A.7 - A.18 in Appendix A list the $\chi^2/N_{\mathrm{dof}}$ values for all observables for the shower used with the default parameter values and with the two new tunes. Since Vincia and Pythia8 already fit the data very well before the tuning, there are no significant changes in the description of the single observables. The jet rates are described best by these two Monte Carlo programs compared to the other observable. Particle spectra and event shapes are also described well. For the latter some observables come with a very small and some with a rather high $\chi^2/N_{\mathrm{dof}}$ value. Herwig++ with angular ordering describes particle multiplicities and particle spectra best of all observables leading to a higher compatibility with existing LEP measurements for the tune to all observables. The dipole shower describes, for both evolution variables, jet rates best of all observables and the $b$ quark fragmentation functions worst. To describe the latter more precisely it would be necessary to take mass effects of $b$ quarks into account.

By using specific observables the Herwig++ showers can be told apart from the other shower models due to high differences in $\chi^2/N_{\mathrm{dof}}$. A more difficult task is discriminating Pythia8 from Vincia and also Vincia with ordering in mass and transverse momentum since the distribution of the observables used in the tuning look very much alike. Therefore the discriminating power of the observables proposed in Sec. 6.3.1 is a useful tool for this task.

As an example for the improvement in describing LEP data Fig. 7.1 shows the planarity $P$ for the default value and the best tune to all observables. The distributions for the $p^2_{\perp\mathrm{dip}}$-ordered dipole shower of Herwig++ and the $p^2_{\perp\mathrm{A}}$-ordered shower of Vincia are

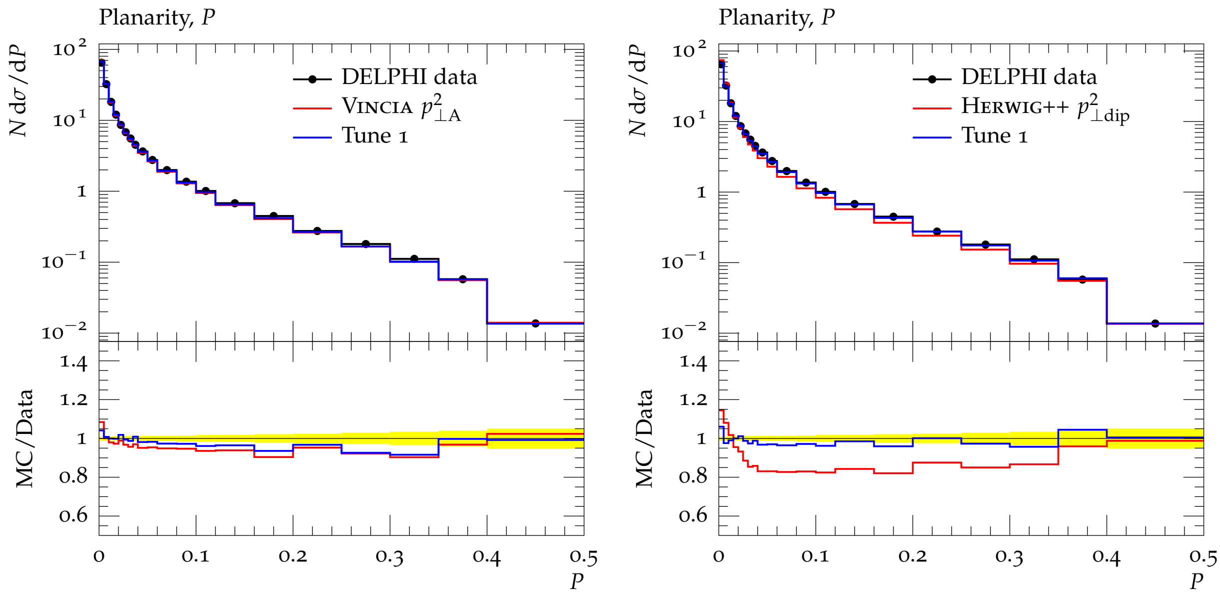


Figure 7.1: The planarity $P$ is plotted for the $p^2_{\perp \mathrm{dip}}$-ordered dipole shower of HERWIG++ on the right and for the $p^2_{\perp \mathrm{A}}$-ordered shower of VINCIA on the left. To compare the results of the Monte Carlo generators before and after the tuning, the predictions with the default values of the parameters (red) and the best tune (blue) are shown. The values for the latter are obtained by the tune to all observables.

included. For both examples an improvement in the description of the data is clearly visible in the ratio plot.

### Parameter Values

The parameter values obtained by the best tune for the two different tuning processes are listed in Tab. A.6 in the appendix. In addition, the default values and the scanned range are shown for the different parameters. The parameter values for the two tunes do not differ significantly from each other besides the following exceptions for the $q^2_{\mathrm{dip}}$-ordered dipole shower of HERWIG++. The cluster mass exponent $\mathrm{Cl}_{\mathrm{pow}}$ changes with a factor 5 due to a rather flat distribution in $\chi^2/N_{\mathrm{dof}}$. The constituent mass of the gluon, $m_g$, also changes with more than a factor 2 since the small value is driven mostly by mean multiplicities and particle spectra. Event shapes prefer a higher value that will be chosen when this group of observables is significantly weighted up.

When comparing the values of the strong coupling $\alpha_{M_Z}$ for the $q^2_{\mathrm{dip}}$- and $p^2_{\perp \mathrm{dip}}$-ordered dipole shower of HERWIG++ it transpires that the value for ordering in $p^2_{\perp \mathrm{dip}}$ is more physical[4]. This matches to the fact that the $q^2_{\mathrm{dip}}$-ordered shower is non-coherent and therefore ordering in $p^2_{\perp \mathrm{dip}}$ is the more physical choice.

### Validation

The distribution of the 300 tunes based on 500 randomly selected runs at different parameter points are plotted in Figs. 7.2 and 7.3 for two parameters for the HERWIG++ $p^2_{\perp \mathrm{dip}}$-ordered dipole shower and for VINCIA with ordering in $p_{\perp \mathrm{A}}$. Narrow distributions indicate that the observables are very sensitive to this parameter. Broader distributions are obtained if either the observables are less sensitive to a parameter or, as for the Lund parameters $a_L$ and $b_L$, if two parameters are highly correlated.

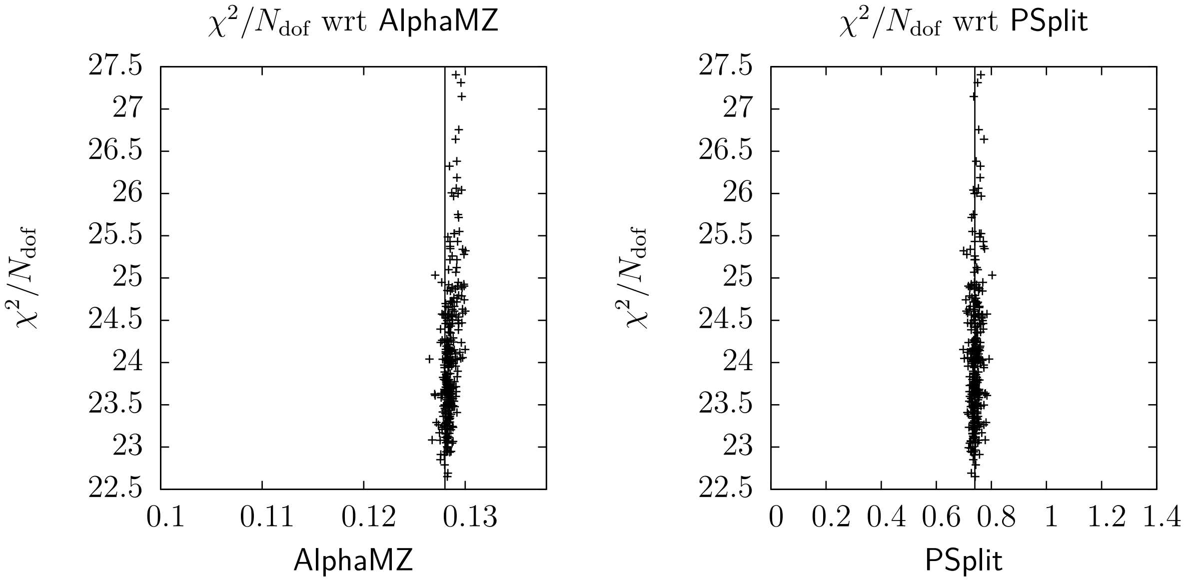


Figure 7.2: Scatterplots for AlphaMZ and PSplit with real Monte Carlo runs for the Herwig++ $p^2_{\perp\mathrm{dip}}$-ordered dipole shower. The plots show the $\chi^2/N_{\mathrm{dof}}$ values with respect to the parameter value. The crosses mark the results of the 300 different run combinations, as obtained in the tune to all observables. The vertical line indicates the parameter value of the best tune and the plot boundaries are chosen to be equal to the scanned range of the parameter.

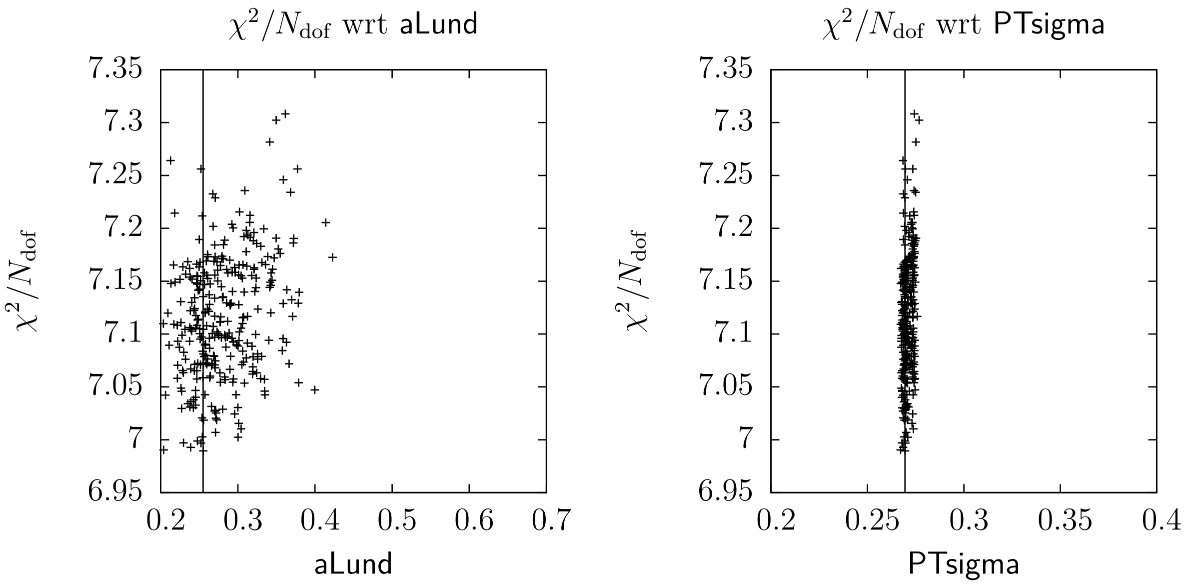


Figure 7.3: Scatterplots for AlphaMZ and PSplit with real Monte Carlo runs for the Vincia $p_{\perp\mathrm{A}}$-ordered shower. The plots show the $\chi^2/N_{\mathrm{dof}}$ values with respect to the parameter value. The crosses mark the results of the 300 different run combinations, as obtained in the tune to all observables. The vertical line indicates the parameter value of the best tune and the plot boundaries are chosen to be equal to the scanned range of the parameter.

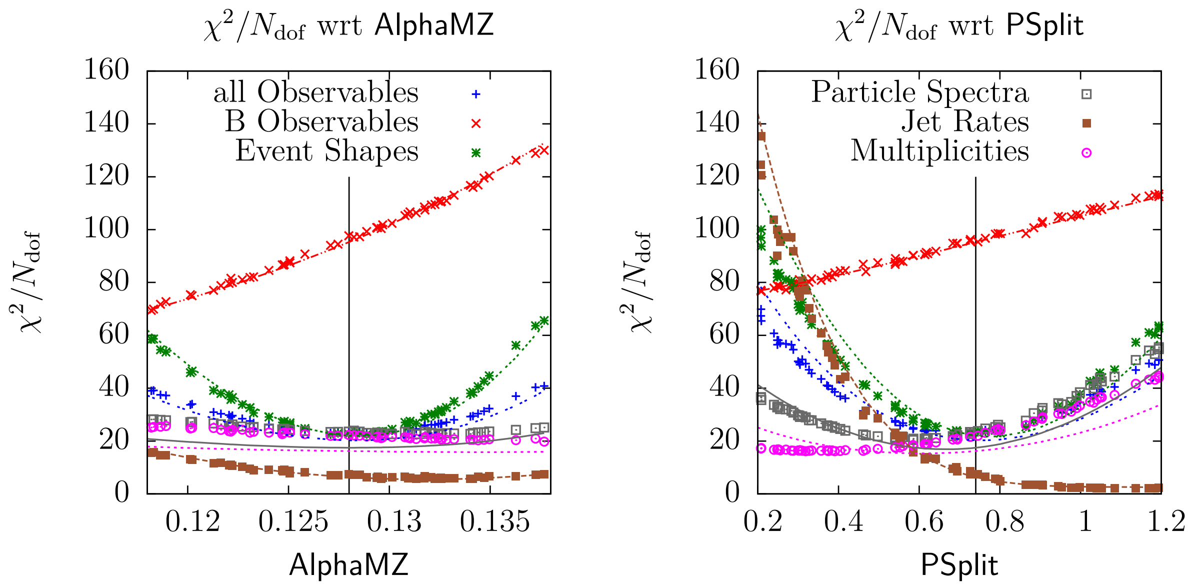


Figure 7.4: A scan of AlphaMZ and PSplit with real Monte Carlo runs and interpolation result of PROFESSOR for the HERWIG++ $p_{\perp\text{dip}}^2$-ordered dipole shower. The other parameters are fixed at their new tuned value determined by the tune to all observables. The vertical line indicates the value of the scanned parameter PROFESSOR that was found in the minimization step. The curves show the $\chi^2/N_{\rm dof}$ for the different types of observables and the blue curve the combination of all observables. Points correspond to the real Monte Carlo and lines to the interpolation result.

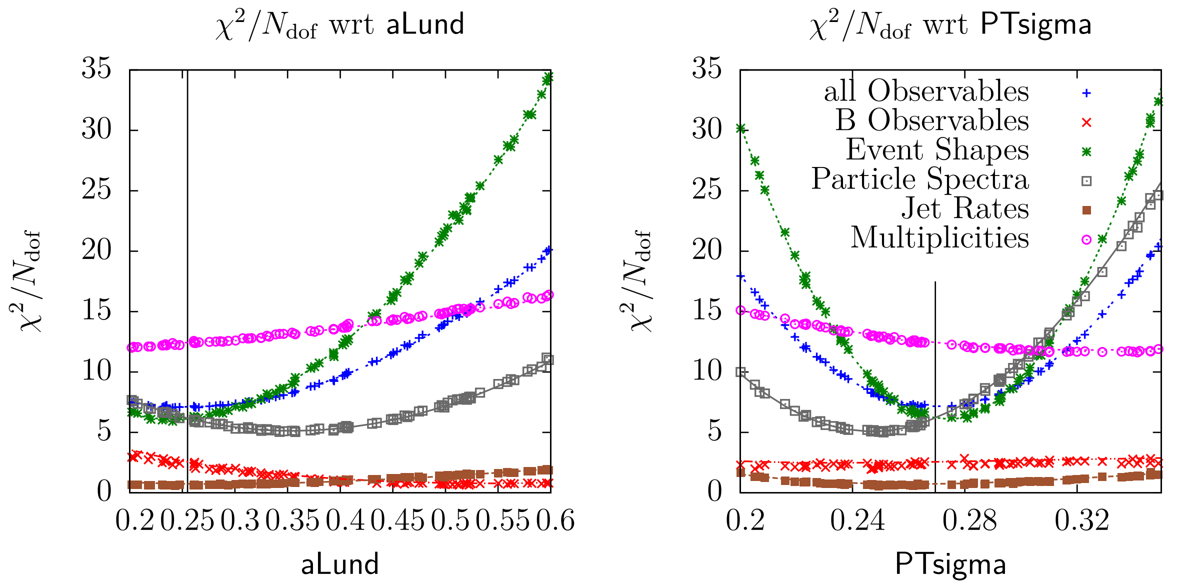


Figure 7.5: A scan of aLund and PTsigma with real Monte Carlo runs and interpolation result of PROFESSOR for the VINCIA $p_{\perp\text{A}}$-ordered shower. The other parameters are fixed at their new tuned value determined by the tune to all observables. The vertical line indicates the value of the scanned parameter PROFESSOR that was found in the minimization step. The curves show the $\chi^2/N_{\rm dof}$ for the different types of observables and the blue curve the combination of all observables. Points correspond to the real Monte Carlo and lines to the interpolation result.

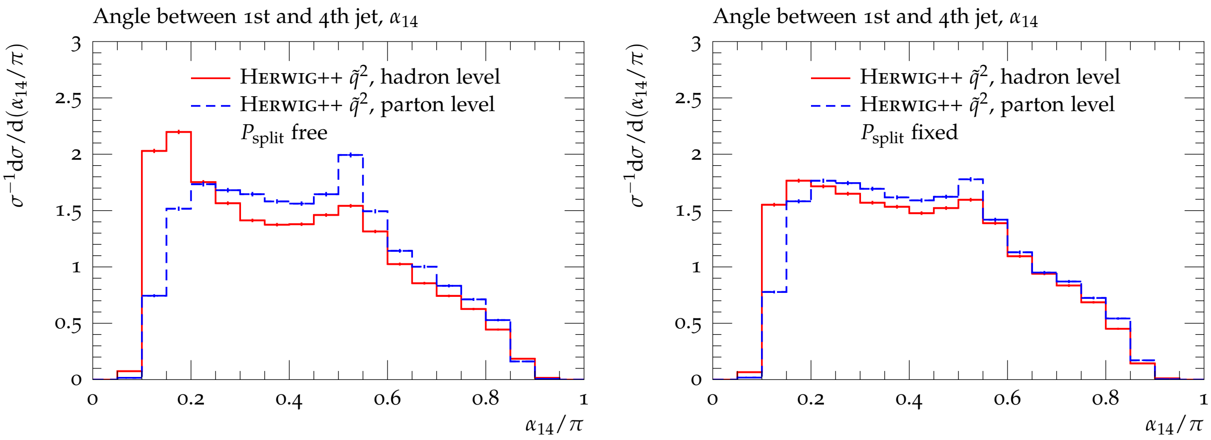


Figure 7.6: A comparison between hadron level (red solid) and parton level (blue dashed) for the normalized distribution of $\alpha_{14}$ for the HERWIG++ angular-ordered shower. The right plot corresponds to keeping $P_{\text{split}}$ fixed during the tuning and the left one to the result when no constraints are put on that parameter during the tuning. To obtain these plots the parameter values of the tune to all observables are used.

In order to verify the result of the generator tuning with PROFESSOR real Monte Carlo runs are performed where only one parameter is changed with randomly distributed values and the other parameters are set to their new tuned value. The histograms are reproduced at the same parameter points again by using the interpolation function PROFESSOR calculated. The distribution of the goodness of fit is shown with respect to two parameters for the HERWIG++ $p^2_{\perp\text{dip}}$-ordered dipole shower and for VINCIA with ordering in $p^2_{\perp\text{A}}$ in Figs. 7.4 and 7.5. The $\chi^2/N_{\text{dof}}$ value is split for the different groups of observables where the lines correspond to the interpolation result and the points to the real Monte Carlo runs. Therefore it is possible to evaluate the quality of the interpolation functions. Fig. 7.4 shows that the parameter values of the best tunes, marked by vertical line, are clearly favoured, mostly driven by event shapes. As mentioned above, not all regions where the interpolation did not work sufficiently well are removed leading to the different $\chi^2/N_{\text{dof}}$ values for interpolation and Monte Carlo runs. Since the quality of the interpolation is disrupted by the possibility for new splitting process for higher gluon masses, especially identified particle spectra and mean multiplicities can not be described very well. This affects of course also the other parameters. The interpolation worked better for VINCIA, shown in 7.5 where interpolation and generator response agree perfectly.

Some parameters show flat distributions in $\chi^2/N_{\text{dof}}$ and others prefer to be at the limit of the scanned range as occurring for example for $\alpha_S$ within the tuning of PYTHIA8 and VINCIA. This is consistent with using only LO accuracy for the hard process and the shower approximation for resumming all higher orders.

### 7.2.1 Hadronization Effects

The influence of hadronization and $B$ decays on the new observables was investigated in Sec. 6.3.3. The normalized distribution of the angular observable $\alpha_{14}$ in Fig. 6.4 showed an enhancement for small values due to hadronization for the HERWIG++ shower models when used with their default parameter values. This enhancement reduced mostly for the dipole shower due to changing the values of the hadronization parameters throughout

[4]The strong coupling has been measured to be about 0.12 at the $Z^0$-pole.

the tuning, but unfortunately did not for the angular-ordered shower. By checking the influence of the hadronization parameters on the shape of the distribution of $\alpha_{14}$, the mass exponent for daughter clusters $P_{\text{split}}$ is identified as the cause of the enhancement. By keeping it fixed at a value of 0.6 during the tuning a better agreement between hadron level and parton level for the normalized distributions of $\alpha_{14}$ is achieved. Fig. 7.6 shows these distribution for keeping $P_{\text{split}}$ fixed on the right and for no constraints on the left. The histograms that the influence of hadronization is reduced strongly by keeping the parameter fixed, but still leaving corrections due to non-perturbative effects.

### 7.2.2 Eigentunes

In order to predict the uncertainty in the Monte Carlo predictions in connection with changing the parameter values during the tuning, so-called eigentunes are performed. The parameters are varied along the eigenvectors in parameter space where the eigenvectors are obtained by certain changes, $\Delta\chi^2/N_{\text{dof}}$, in $\chi^2/N_{\text{dof}}$. For each parameter two eigenvectors, one in $+$ and one in $-$ direction, exist. If the goodness of fit is supposed to be distributed as a true $\chi^2$ function $\Delta\chi^2/N_{\text{dof}} = 1$ would correspond to a one sigma deviation and $\Delta\chi^2/N_{\text{dof}} = 4$ to a two sigma deviation.

Unfortunately it was not possible to construct all eigenvectors with Professor for each shower and tune, hence in most cases only ten instead of twelve eigenvectors are used. Since this might slightly underestimate the tuning error the two sigma deviation will be used.

### 7.2.3 New Observables and Experimental Resolution

To validate that the new observables can tell the shower models apart when the Monte Carlo generators are used with tuned shower and hadronization parameters, the normalized distribution of the angle $\alpha_{14}$ and the ratio of jet masses $M_L^2/M_H^2$ are shown in Fig. 7.7 with the tuned parameters. In order to take the tuning error into account the envelopes for a two sigma deviation at 100% confidence level are included. The lower left plot of Fig. 7.7, showing the asymmetry of $\alpha_{14}$, validates that this observables can still distinguish between some of the shower models within the limits of the tuning error and between all shower models within only the statistical.

To check the experimental detector resolution for measuring angles of jets, the same plot as on the right side in Fig. 6.10 is shown here again in the lower right side of Fig. 7.7. The tuning error is again taken into account by using the envelopes for a two sigma deviation at 100% confidence level. The plot confirms mostly the result of Sec. 6.5: Even for a value of 0.1 for the resolution, which is more than the actual experimental resolution, it is still possible to tell the showers apart.

## 7.3 Conclusions

Due to the tuning effort the main parameters of hadronization and shower model have been readjusted in a way that the different shower models describe existing LEP data as effectively as possible. Even with taking the detector resolution and the tuning error into account it is still possible to use the new observables for telling the different shower models apart. Although Herwig++ and Pythia8 or Vincia respectively can already be told apart by using existing measurements the discriminating power of the observables proposed in Sec. 6.3.1 is still of great value concerning the differentiation of Pythia8 and Vincia. Therefore the next step is the measurement of these observables with LEP data in order to make a statement about how well the shower models fit to real measurements.

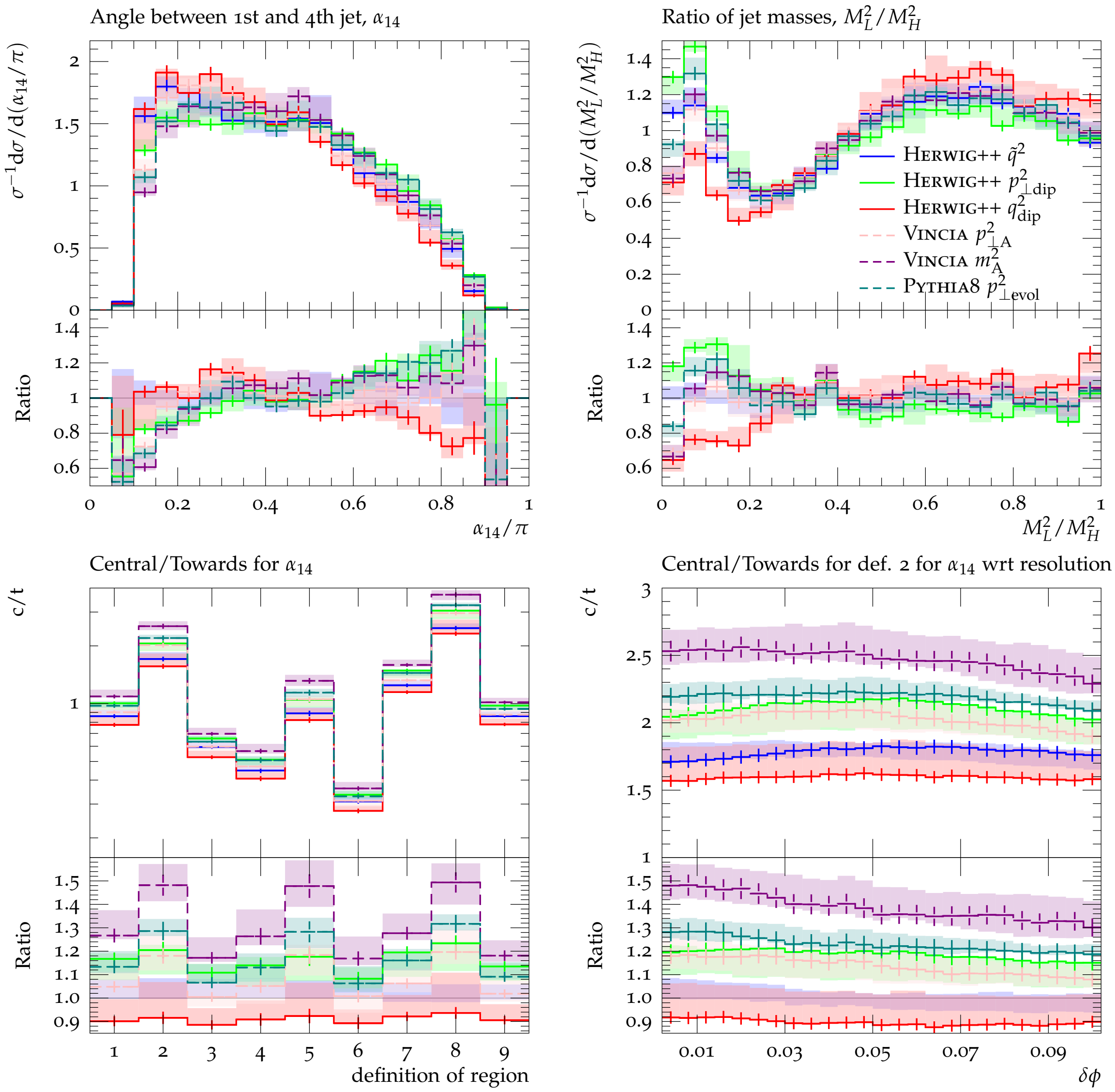


Figure 7.7: The upper plots show the normalized distributions of the angle $\alpha_{14}$ and the mass ratio $M_L^2/M_H^2$. The asymmetry for different definitions according to Eq. (6.13) for $\alpha_{14}$ is shown in the lower left plot whereas the lower right plot shows the asymmetry for the second definition of the regions (see Tab. 6.4) with respect to the resolution $\delta\phi$. The ratio plot shows the deviation of the showers with respect to the Herwig++ angular-ordered default shower. The error bars are the statistical Monte Carlo errors and the error bands show the envelopes for 100% confidence level for $\Delta\chi^2/N_{\mathrm{dof}} = 4$ (two sigma deviation).

# 8. Data Analysis

In the last chapter the different shower models have got a similar and fair treatment by readjusting the main parameters of hadronization and shower model. Thus they now describe existing LEP measurement in the best possible way. To validate which shower approach and therefore which shower characteristics and properties are able to describe nature best, LEP data will be analyzed in terms of the observables proposed in Sec. 6.3.1.

For this purpose an already existing framework for the reconstruction, correction and analysis of OPAL data, as for example used and described in Ref. [51], was applied. Sec. 8.1 describes how the event samples are selected. The following sections provide a more detailed discussion of certain aspects of the measurement using the angular observables, $\alpha^*$ and $\alpha_{14}$, and the ratio of jet masses, $M_L^2/M_H^2$.

## 8.1 Selection of Events

The data set used in Ref. [51] covers the whole data recorded with the OPAL detector within the LEP2 run, see Sec. 3.1 and 3.2. During this high energy run, calibration runs were taken at the $Z^0$-peak, at a center-of-mass energy of 91.2 GeV. The data used for measuring the observables proposed in Sec. 6.3.1, corresponds to the calibration runs, providing about 400 000 event at the $Z^0$-peak. Therefore only details of the reconstruction and cuts on the events that are important for this specific center-of-mass energy are described.

To select hadronic decays of the $Z^0$ boson, different criteria on the energy clusters in the electromagnetic calorimeter and the charged track multiplicity are imposed. A detailed documentation of these cuts can be found in Ref. [52]. In order to take only events into account that hit the detector acceptance, the so-called containment cut is used. This cut on the angle of the thrust axis with respect to the beam axis, $|\cos\theta_T| < 0.9$, removes events with lots of activity centered around the beam axis.

## 8.2 Reconstruction and Correction

To correct observables calculated with the LEP data from detector level down to hadron level, event samples generated with the Monte Carlo event generator Pythia6 are used.

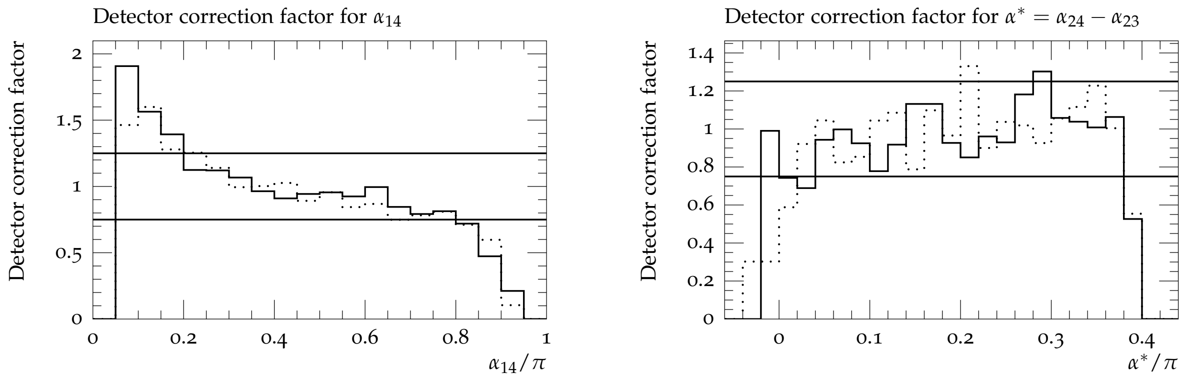


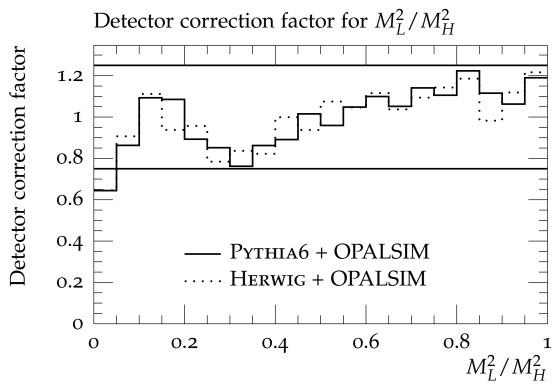


Figure 8.1: The plots show the detector correction factor for the angular observables, $\alpha^*$ and $\alpha_{14}$, and the mass ratio, $M_L^2/M_H^2$. The solid lines correspond to the ratios obtained with Pythia6 and the dotted lines with Herwig event samples plus a full simulation of the OPAL detector. The horizontal lines indicate the $\pm 25\%$ variance of the corrections factors to being unity.

The Monte Carlo events are processed through a full simulation of the OPAL detector [53] and then reconstructed in the same way as the real data, by using the energy flow algorithm. This algorithm matches the tracks of charged particles emerging in the track chambers with the energy clusters of the electromagnetic calorimeter of the detector. Since the tracks provide the more reliable measured information all tracks and only the clusters that are not matched with tracks are used for the calculation of the observables. A detector correction factor for each bin and observable is calculated by building the ratio of the observable on hadron level to the corresponding value on detector level for the Monte Carlo event samples. This ratio is multiplied to the real data to correct the observables down to hadron level.

Fig. 8.1 shows the detector correction factors for the angle between the first and fourth jet, $\alpha_{14}$, the difference in opening angles, $\alpha^*$, and the mass ratio $M_L^2/M_H^2$. In order to obtain a reliable measurement the detector correction factor should be of the order one. Therefore the vertical lines in Fig. 8.1 mark the $\pm 25\%$ variance. For the mass ratio this criteria is fulfilled for all except the first bin, which is the bin where a hadronization effect showed up for all shower models. For the angular observable $\alpha_{14}$ large correction factors appear for small values and small factors for high values of this observable leading to a more unreliable measurement for small and high values of $\alpha_{14}$. Therefore, statements concerning these regions have to be done with caution and with keeping in mind that these regions are not measured very reliable. The part with small values of $\alpha_{14}$ is as well the region where hadronization effects show up for Herwig++. The detector correction factors for $\alpha^*$ fulfill mostly the $\pm 25\%$ criterion. Only for very small and very large values of $\alpha^*$ the correction factor gets very small. This example also shows that the systematic uncertainties scale with statistics since the difference in the correction factors for Herwig and Pythia6 contributes to the systematic error, as will be discussed in the next section.

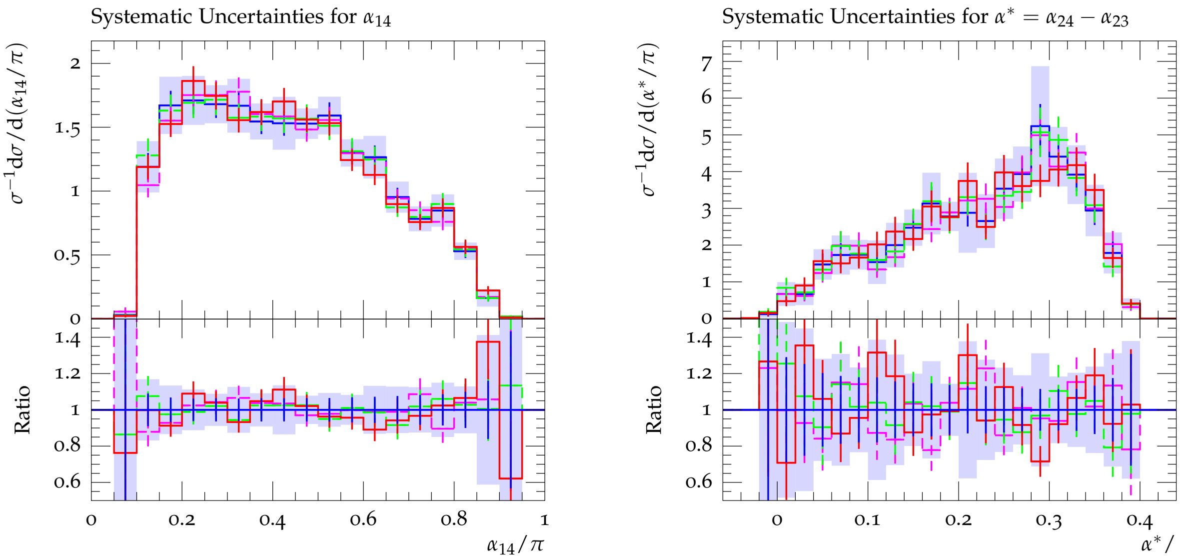


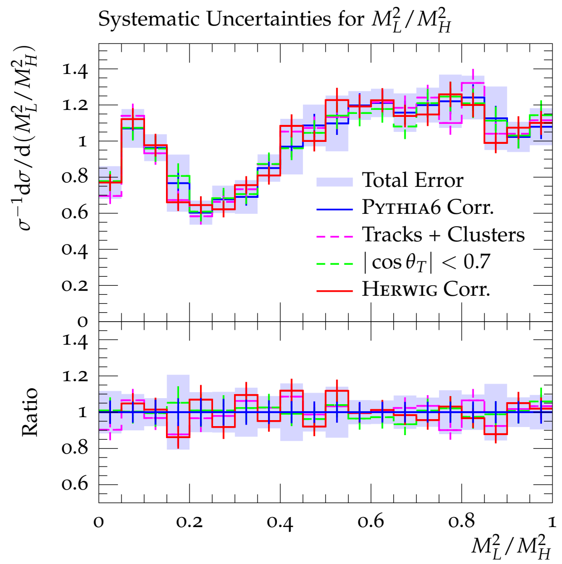


Figure 8.2: The plots show different contributions to the systematic uncertainties for $\alpha_{14}$, $\alpha^*$ and $M_L^2/M_H^2$. The solid blue line corresponds to the standard procedure for reconstruction and correction. The solid red line is obtained by using HERWIG instead of PYTHIA6 for the detector correction. The dashed green line corresponds to a tightening of the containment cut and the dashed magenta line to using all tracks and calorimeter clusters during the reconstruction. The error bars show the statistical errors for the different contributions and the blue band the total, statistic and systematic, error. The ratio plot shows the deviation to the standard procedure.

For $\alpha^*$ only about half as many events, compared to $\alpha_{14}$, enter and hence higher deviations between the two curves in the upper right plot in Fig. 8.1 occur.

## 8.3 Systematic Uncertainties

The systematic errors are calculated by repeating the analysis with varied cuts for the selection of events and varied reconstruction procedures. For a center-of-mass energy of 91.2 GeV the contributions to the systematic uncertainties are the following:

- Variation of the cut on the polar angle of the thrust axis: $|\cos\theta_T| < 0.7$
- The detector correction is calculated using HERWIG instead of PYTHIA6.
- Variation of the reconstruction procedure: All tracks and clusters are taken into account. In this case the detector correction takes care of the double counting.

The systematic error is calculated with the sum of quadrature of the different contributions above. The total error of the data is obtained by the sum of quadrature of the systematic error and the statistical error of the standard event selection and reconstruction procedure.

The effect of the different contributions to the systematic uncertainty for the angles $\alpha_{14}$ and $\alpha^*$ and the mass ratio $M_L^2/M_H^2$ can be found in Fig. 8.2. For all observables the largest effect on the systematic error is obtained by using HERWIG instead of PYTHIA6 whereas the variation of the containment cut has the smallest influence. These statements are correct for the plots as total, but of course the effect of the different contributions to the systematic errors changes for each bin.

# 9. Comparison of LEP Data with Monte Carlo Event Generators

As described in the previous chapter, all observables listed in Tab. 9.1 are measured with OPAL data in this work. A comparison between the different theory models for the shower and LEP data is now possible. In Sec. 6.4, a comparison among the Monte Carlos with their default parameter values[1] can be found for the angular variables, $\alpha_{14}$ and $\alpha^*$, and the ratio of jet masses, $M_L^2/M_H^2$. An overview of the observables, that were not introduced in the previous chapters is given in Sec. 9.1. In the following, Sec. 9.2 deals with a general comparison of the different shower models with OPAL data. All Monte Carlo generators are used with the values for the parameters obtained by the best tune to all observables in the previous chapter. However, a short section, dealing with the results of both tunes, is included. For these comparisons all of the observables, described in Sec. 9.1, will be used. For the sections hereafter only a few observables will be used to support the main statements, which will be only of qualitative nature. A comparison between the two ordering conditions in Vincia, strong and smooth ordering, is applied in Sec. 9.3 and Sec. 9.4 brings the NLO dipole shower of Herwig++ and Vincia with matrix-element correction into focus.

## 9.1 Observables

All observables used for the comparison between OPAL data and the Monte Carlo event generators are listed in Tab. 6.3 together with the event selection cuts. The angular variables, $\alpha_{14}$ and $\alpha^*$, and the ratio of jet masses, $M_L^2/M_H^2$ were already introduced in Sec. 6.3.1.

In order to get a wider range of observables, different ratios of energy correlations, as proposed in Ref. [54], are used. The $N$-point energy correlation function (ECF), as defined in Ref. [54], is

$$\mathrm{ECF}(N,\beta) = \sum_{i_1<i_2<\ldots<i_N} \left(\prod_{a=1}^{N} E_{i_a}\right) \left(\prod_{b=1}^{N-1} \prod_{c=b+1}^{N} \theta_{i_b i_c}\right)^{\beta} , \tag{9.1}$$

[1] or previous tunes

| Observable | Jets | Cuts | | | |
|---|---|---|---|---|---|
| $\alpha^*$ | 4 | $y_{3\to4} > 0.0045$, | $\alpha_{12/13} > 2\pi/3$, | $\alpha_{23} < \pi/6$, | $\alpha_{24} < \pi/2$ |
| $\alpha_{14}$ | 4 | $y_{3\to4} > 0.0045$, | $\alpha_{12/13} > 2\pi/3$, | $\alpha_{23} < \pi/6$ | |
| $C(2, 0.2)$ | 4 | $y_{3\to4} > 0.0045$, | $\alpha_{12/13} > 2\pi/3$, | $\alpha_{23} < \pi/6$ | |
| $C(2, 2.0)$ | 4 | $y_{3\to4} > 0.0045$, | $\alpha_{12/13} > 2\pi/3$, | $\alpha_{23} < \pi/6$ | |
| $M_L^2/M_H^2$ | 2 | $y_{3\to4} > 0.0045$, | $y_{3\to4} > y_{2\to3}/2$ | | |
| $C_s(1, 0.2)/C_h(1, 0.2)$ | 2 | $y_{3\to4} > 0.0045$, | $y_{3\to4} > y_{2\to3}/2$ | | |
| $C_s(1, 2.0)/C_h(1, 2.0)$ | 2 | $y_{3\to4} > 0.0045$, | $y_{3\to4} > y_{2\to3}/2$ | | |

Table 9.1: Observables, number of jets the event in clustered in and associated cuts used in the analysis.

where the sum runs either over all jets in events with four jets or over the particles of a jet in two-jet events. Thus $\theta_{i_1 i_2}$ denotes the angle between either jets or particles $i_1$ and $i_2$ . These correlation functions are used to build double ratios

$$C(N, \beta) = \frac{\mathrm{ECF}(N+1, \beta)\mathrm{ECF}(N-1, \beta)}{(\mathrm{ECF}(N, \beta))^2} \,. \tag{9.2}$$

For the analysis values of $\beta = 0.2$ and $\beta = 2.0$ are chosen to be sensitive to either soft or collinear configurations. For events with two jets, selected with the same cuts as the events for the mass ratio, the 1-point double ratio

$$C(1, \beta) = \frac{\sum\limits_{i<j\in J} E_i E_j \theta_{ij}^{\beta}}{\left(\sum\limits_{i\in J} E_i\right)^2} \tag{9.3}$$

is calculated for both jets. In order to get information about the relative amount of radiation in the two hemispheres, a ratio is build by dividing the double ratio with the smaller value by the one with the higher value,

$$\frac{C_s(1, \beta)}{C_h(1, \beta)} = \frac{\sum\limits_{i<j\in J_s} E_i E_j \theta_{ij}^{\beta}}{\left(\sum\limits_{i\in J_s} E_i\right)^2} \cdot \frac{\left(\sum\limits_{i\in J_h} E_i\right)^2}{\sum\limits_{i<j\in J_h} E_i E_j \theta_{ij}^{\beta}} \,. \tag{9.4}$$

For $\beta = 2.0$ Eq. (9.4) is approximately the second order expansion of the mass ratio since the invariant mass squared of a particle pair is defined as

$$M_{ij}^2 = E_i E_j (1 - \cos\theta_{ij}) \approx E_i E_j \theta_{ij}^2/2 \tag{9.5}$$

$$\text{with} \quad \cos\theta_{ij} \approx 1 - \theta_{ij}^2/2 \,. \tag{9.6}$$

Small values of $C(1, 2.0)$ refer to collinear emissions inside the jet whereas soft wide-angle emissions lead to higher values. When building the ratio of the double ratios of the two jets, small values refer to asymmetric events where one hemisphere is dominated by collinear and the other by soft wide-angle emissions. Events with same amounts of emission in both hemispheres lead to high values of $C_s(1, 2.0)/C_h(1, 2.0)$. For $\beta = 0.2$

all angles are weighted relatively equal. Hence $C(1, 0.2)$ is small for jets containing very asymmetric particles, for example one very soft and one very hard particle. A jet that contains many soft particles leads to high values. Building the ratio of two double ratios $C(1, 2.0)$ and obtaining high values, means that both hemispheres are dominated by the same type of emission.

For event topologies which underlie for instance the measurement of the angle $\alpha_{14}$, the 2-point double ratio

$$C(2,\beta) = \frac{\sum\limits_{j_1<j_2<j_3} E_{j_1}E_{j_2}E_{j_3}(\theta_{j_1j_2}\theta_{j_1j_3}\theta_{j_2j_3})^\beta}{\left(\sum\limits_{j_1<j_2} E_{j_1}E_{j_2}\theta^\beta_{j_1j_2}\right)^2} \cdot E_{\mathrm{vis}} \tag{9.7}$$

is used, where the sum runs over the four jets. The events for this observable are selected with the same cuts as for the angle between the first and fourth jet, $\alpha_{14}$, leading to the same event topologies. The second and third jet build a collinear pair due to the cut on their opening angle. Therefore, these events look like three-jet systems to the observables. The three-jet event contains two hard jets, jet 1 and jet 23[2], lying back-to-back and a third soft jet, jet 4. With this notation Eq. (9.7) can approximately be written as

$$C(2,\beta) \approx \frac{E_1E_{23}E_4(\theta_{1\,23}\theta_{14}\theta_{23\,4})^\beta}{(E_1E_{23}\theta^\beta_{1\,23} + E_1E_4\theta^\beta_{14} + E_{23}E_4\theta^\beta_{23\,4})^2} \cdot E_{\mathrm{vis}}\ . \tag{9.8}$$

Since the fourth jet is soft, its energy $E_4$ is small compared to the other energies in the event. The angle between jet 1 and jet 23 is large, $\theta_{1\,23} > 2\pi/3$, due to the event selection cuts. Therefore, the denominator in Eq. (9.8) can be reduced to its first term, leading to

$$C(2,\beta) \approx \frac{E_4(\theta_{14}\theta_{23\,4})^\beta}{E_1E_{23}\theta^\beta_{1\,23}} \cdot E_{\mathrm{vis}}\ . \tag{9.9}$$

The angle $\theta_{1\,23}$ is about fixed due to the cuts on opening angles. This leaves only the angles relative to the fourth jet and the energies as free parameters. For $\beta = 2.0$, where wide angles are given greater weight, $C(2, 2.0)$ is small, if the fourth jet is either collinear to the first jet or to the pair of the second and third jet. Higher values for the double ratio $C(2, 2.0)$ are obtained for jet configurations where the fourth jet is approximately perpendicular to the other jets. For $\beta = 0.2$ all angles are weighted relatively equal and hence $C(2, 0.2)$ is proportional to the energy of the fourth jet, relative to the remaining energy of the event.

## 9.2 General Comparison

This section presents the comparison between the Monte Carlo predictions and the LEP data, starting with a general qualitative comparison for the different observables. All shower models with the different evolution variables are used with the parameter values that are obtained by the tune to all observables. At the end, a shape compatibility test is performed for all observables to compare the shower models quantitatively. The plots for the observables, which are not shown here, can be found in Appendix B.

[2]The combination of the second and third jet.

### Angle between first and fourth Jet: $\alpha_{14}$

The normalized distribution of $\alpha_{14}$ and the ratio of the central to towards region are shown in Fig. 9.1. The distributions are separated for Herwig++ and the Pythia8 / Vincia Monte Carlo group for reasons of clarity and comprehensibility. The histograms for the normalized distribution contain the $\chi^2/N_{\mathrm{dof}}$ value as additional information. All shower models are able to describe this distribution very well, leading to $\chi^2/N_{\mathrm{dof}}$ values smaller than one, except for the $q^2_{\mathrm{dip}}$-ordered dipole shower of Herwig++. However, the value for the latter is still very small. Due to the large error bars of the data the ratio plots for the normalized distribution show at most about up to one sigma deviations for the individual bins. Only few exceptions give rise to effects of about two sigma.

Below the histograms for the ratio of the central to towards region a sketch illustrates the meaning of the ratio. The regions of $\alpha_{14}$ correspond to specific types of emissions and event topologies. This ratio reflects the relative amount of wide-angle to collinear emissions. The limits for the regions that lead to the different definitions are listed in Tab. 6.4. As for the normalized distribution the ratio plots show only small deviations. Most notably are the effects for the $q^2_{\mathrm{dip}}$-ordered dipole shower of Herwig++ and the mass-ordered shower of Vincia. The predictions of the latter are too high. When the antenna mass is used as evolution variable, soft wide-angle emissions are preferred over collinear ones, as shown in the contour plot of the phase-space in Fig. 5.3. This leads to higher values for the relative amount of wide-angle to collinear emissions. For Herwig++ $\alpha_{14}$ showed enhancements for small values due to influences of hadronization and $B$ decays. This effect has been reduced throughout the tuning. However, the non-perturbative effects are still visible in the towards region, leading to undersized values for the ratio of the central to towards for the $q^2_{\mathrm{dip}}$-ordered dipole shower. For the angular-ordered shower of Herwig++, similar effects are only visible, if the limits of the towards region are very tight. However, these effects are not significant. The predictions for the ratio of the central to towards region of all other shower models agree with the data very well.

The other ratios of $\alpha_{14}$ are shown in Fig. 9.1 together with a sketch of their meaning. The histograms with the ratio of the towards to away region confirm that the amount of events, where the fourth jet is collinear to the first jet, is overestimated by the $q^2_{\mathrm{dip}}$-ordered dipole shower and the angular-ordered shower of Herwig++. The ratio of the central to away region provides the best information about the perturbative effects due to leaving out the towards region, which is influenced by non-perturbative effects. Most notably is the deviation between the $q^2_{\mathrm{dip}}$-ordered dipole shower of Herwig++ and the OPAL data. This shower model predicts too many events where the fourth jet origins in a wide-angle emission, compared to events where the first jet lies back-to-back to all other jets. The dipole shower with $p^2_{\perp\mathrm{dip}}$-ordering and Pythia8 tend to predict the ratio of the central to away and towards to away region too small, although this effect is not significant. The predictions of Vincia, for ordering in transverse momentum as well as for ordering in antenna mass, lie within the error bars for both of these ratios.

To take the cross section of $\alpha_{14}$ into account, Fig. 9.6 shows the distribution of $\alpha_{14}$, scaled with the fraction of events that passed the event selection cuts for this observable. The result is the cross section, differentially in the observable, times the same arbitrary factor for all shower models, with respect to the observable. For Herwig++ the quality of the overall description remains about the same, compared to the normalized distribution. No significant differences are visible for the angular- and the $p^2_{\perp\mathrm{dip}}$-ordered shower since the prediction of the fraction of events that passed the selection cuts agrees with the data.

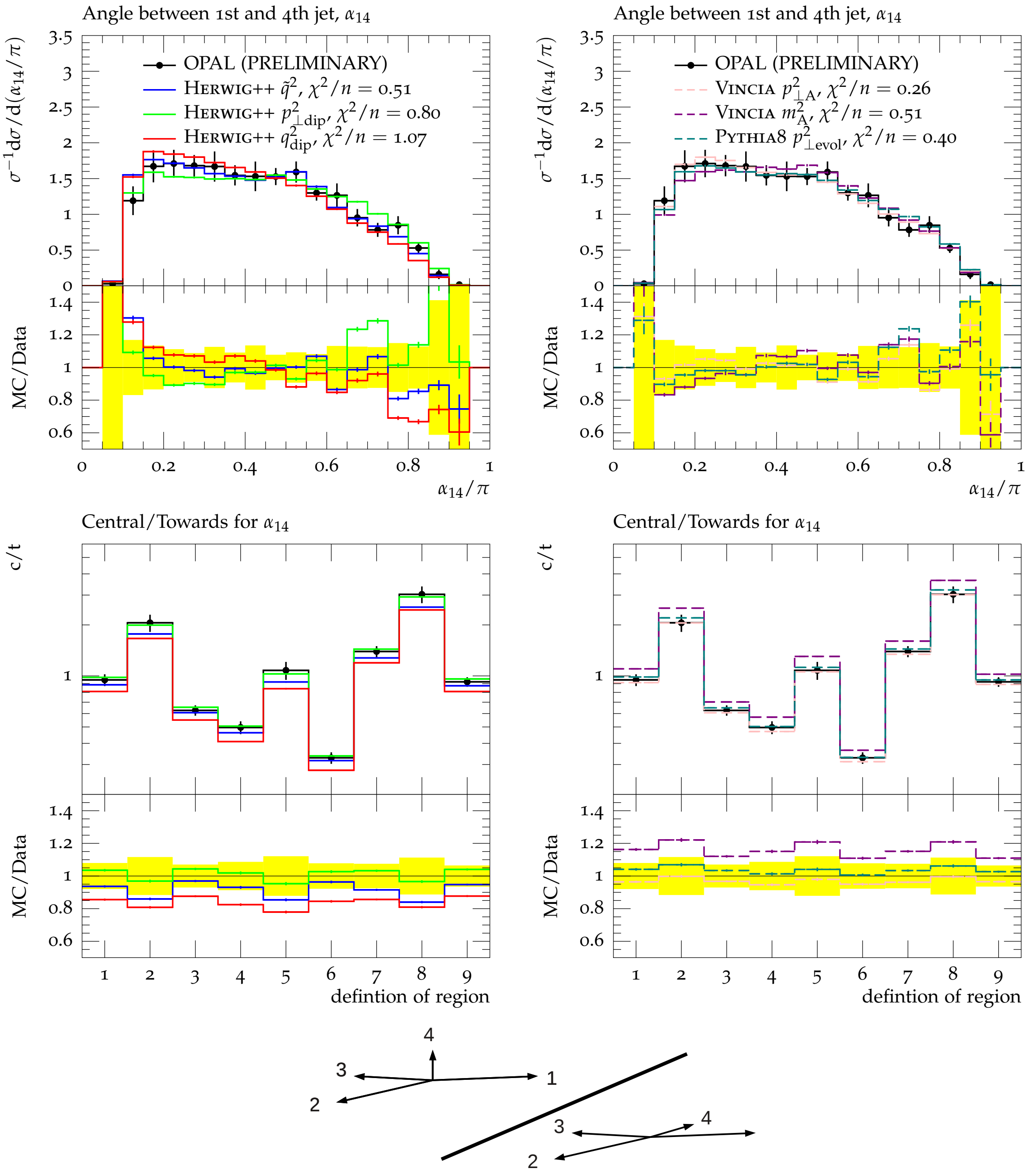


Figure 9.1: The plots show the normalized distribution of the angle $\alpha_{14}$ and the ratio of the central to towards region. The plots on the left hand side show the results for the HERWIG++ shower models, the angular-ordered shower (blue) and the dipole shower with ordering in $p^2_{\perp\text{dip}}$ (green) and $q^2_{\text{dip}}$ (red). The predictions of PYTHIA8 (teal) and VINCIA with ordering in $p^2_{\perp\text{A}}$ (pink) and antenna mass (violet) are shown on the right. The ratio plot shows the deviation of the Monte Carlos with respect to the data.

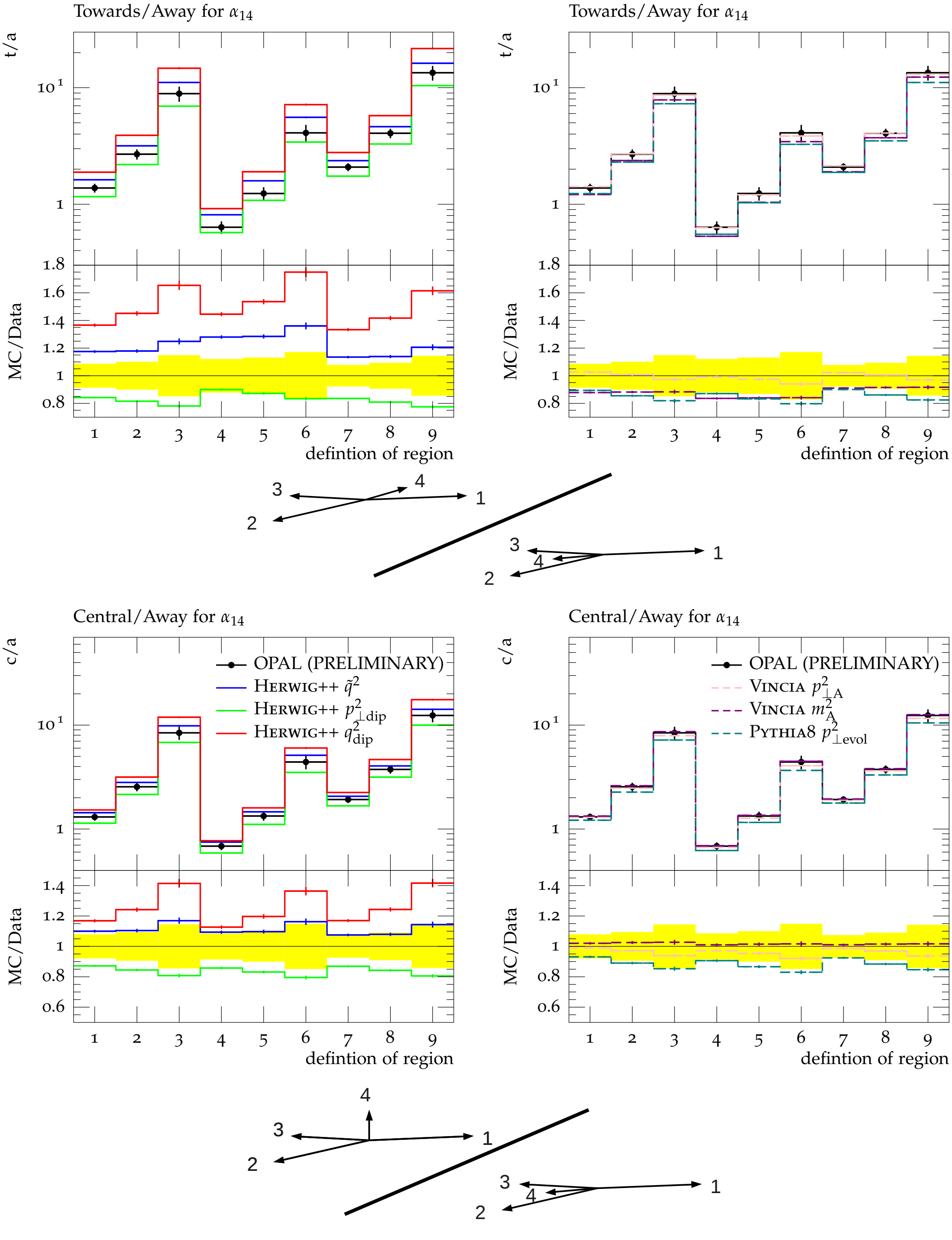


Figure 9.2: The plots show the ratios of the towards to away and the central to away region for the angle $\alpha_{14}$. The plots on the left hand side show the results for the Herwig++ shower models, the angular-ordered shower (blue) and the dipole shower with ordering in $p^2_{\perp\mathrm{dip}}$ (green) and $q^2_{\mathrm{dip}}$ (red). The predictions of Pythia8 (teal) and Vincia with ordering in $p^2_{\perp\mathrm{A}}$ (pink) and antenna mass (violet) are shown on the right. The ratio plot shows the deviation of the Monte Carlos with respect to the data.

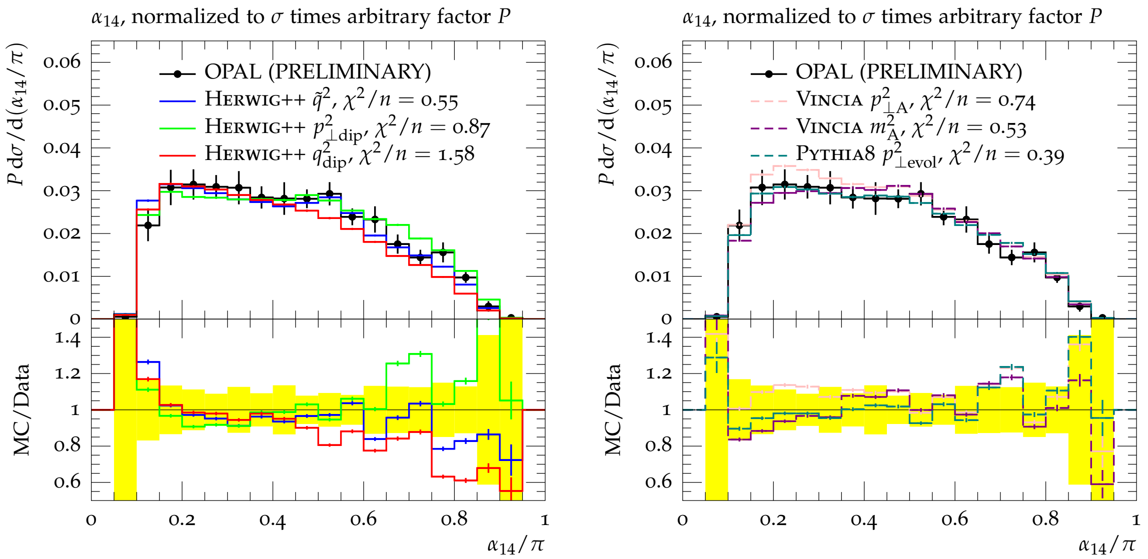


Figure 9.3: The plots show the distribution of the angle $\alpha_{14}$, normalized to the cross section times the same arbitrary factor for each theory model. The plots on the left hand side show the results for the HERWIG++ shower models, the angular-ordered shower (blue) and the dipole shower with ordering in $p^2_{\perp\mathrm{dip}}$ (green) and $q^2_{\mathrm{dip}}$ (red). The predictions of PYTHIA8 (teal) and VINCIA with ordering in $p^2_{\perp\mathrm{A}}$ (pink) and antenna mass (violet) are shown on the right. The ratio plot shows the deviation of the Monte Carlos with respect to the data.

For the $q^2_{\mathrm{dip}}$-ordered shower the description of the towards region improves, whereas up to two sigma deviations are visible in the away region. The only noteworthy conclusion, following the comparison of the normalized and scaled distributions of $\alpha_{14}$ for PYTHIA8 and VINCIA, is the change in $\chi^2/N_{\mathrm{dof}}$ for the $p^2_{\perp\mathrm{A}}$-ordered shower of VINCIA. The value increased by more than a factor 2, best visible in the region $\alpha_{14} \in (0.15, 0.35)$. This shower model predicts the event rate for $\alpha_{14}$ too high, leading to the difference between the scaled and the normalized distribution.

In summary the Monte Carlo generators provide a mostly good and consistent description of the data with only small deviations. Non-perturbative effects are visible in the region where the fourth jet is collinear to the first jet. By using only the central and away regions the focus lies on the perturbative effects. The $q^2_{\mathrm{dip}}$-ordered shower of HERWIG++ shows the trend to underestimate the away region leading to predictions containing too few effective $1 \to 3$ splittings instead of two $1 \to 2$ splittings each. A converse, but not significant effect shows of for PYTHIA8 and the $p^2_{\perp\mathrm{dip}}$-ordered dipole shower.

As mentioned in Sec. 8.2, the towards and away region of $\alpha_{14}$ have to be treated carefully due to very small and very large detector correction factors. Therefore the results of observables like the mass ratio are more reliable.

## 2-Point Double Ratio: $C(2, 0.2)$

The normalized distribution of the 2-point double ratio $C(2, 0.2)$ and the asymmetry are plotted in Fig. 9.4. The plots again separated for Herwig++ and Pythia8 / Vincia. Small values for the double ratio are obtained by a very soft fourth jet, if the angles are weighted relatively equal as they are for the chosen value $\beta = 0.2$. If the fourth jet carries more energy, the value for the double ratio increases. Therefore, the asymmetry of the 2-point double ratio gives the amount of events, where the fourth jet is very soft, with respect to the events with a fourth jet carrying more energy.

The histograms for the normalized distribution contain the $\chi^2/N_{\mathrm{dof}}$ value as additional information. As for the angle $\alpha_{14}$, all shower models are able to describe this distribution very well, leading to $\chi^2/N_{\mathrm{dof}}$ values of order one. Only small deviations between Monte Carlo predictions and LEP data are visible.

The differences are worked out with the help of the asymmetry. The $q^2_{\mathrm{dip}}$-ordered dipole shower tends to underestimate the the asymmetry, hence predicting too few events with a very soft fourth jet. In contrast, Vincia with mass ordering predicts too many very soft emissions, which can again be explained with the phase-space population of this shower. The preference of soft wide-angle emissions over harder collinear ones leads to higher values for the ratio of the 2-point double ratio $C(2, 0.2)$.

Since the same event selection cuts are applied to this observable and to the angle $\alpha_{14}$, the conclusions for both variables are similar, as expected.

## Mass Ratio: $M_L^2/M_H^2$

The normalized distribution of the ratio of hemisphere masses, the according asymmetry and a sketch of the illustration of the asymmetry are shown in Fig. 9.5. The values of $\chi^2/N_{\mathrm{dof}}$, added in the legend of the normalized distribution, confirm that the event generators provide good descriptions of this observable. The predictions of all theory models lead to goodness of fit values close to unity or even less.

The ratio plots of the normalized distribution show that the prediction of high values of the mass ratio lies within the error bars for all shower models. In the region of small mass ratios, deviations between the Monte Carlos and the data are visible. The asymmetry can be used to bring the difference between the regions for small and high mass ratios to mind. As discussed in Sec. 6.3, a large correction due to hadronization shows up in the first bin of the normalized distribution. The correction factor of the data for this bin is small, see Sec. 8.2, which means that the measurement is not reliable. Therefore, this bin is excluded for the for the calculation of the asymmetry in order to decrease the influence of non-perturbative effects and increase the reliability of the measurement at the same time. Excluding this bin is equivalent to a cut in phase-space along a contour of constant mass ratios. As indicated by the sketch in Fig. 9.5, the asymmetry divides the amount of events, where the clustering of the next jets happens within one hemisphere, by the amount of opposite-side events. In the latter the clustering of the next jets happens inside both hemispheres.

The histograms containing the asymmetry for the mass ratio with respect to different asymmetry axes show that the $p^2_{\perp\mathrm{dip}}$-ordered shower of Herwig++ produces too many same-side events and too few events where the next clustering of the next jets happens in both hemisphere. For Herwig++ with $q^2_{\mathrm{dip}}$-ordering, the results are reversed. Here,

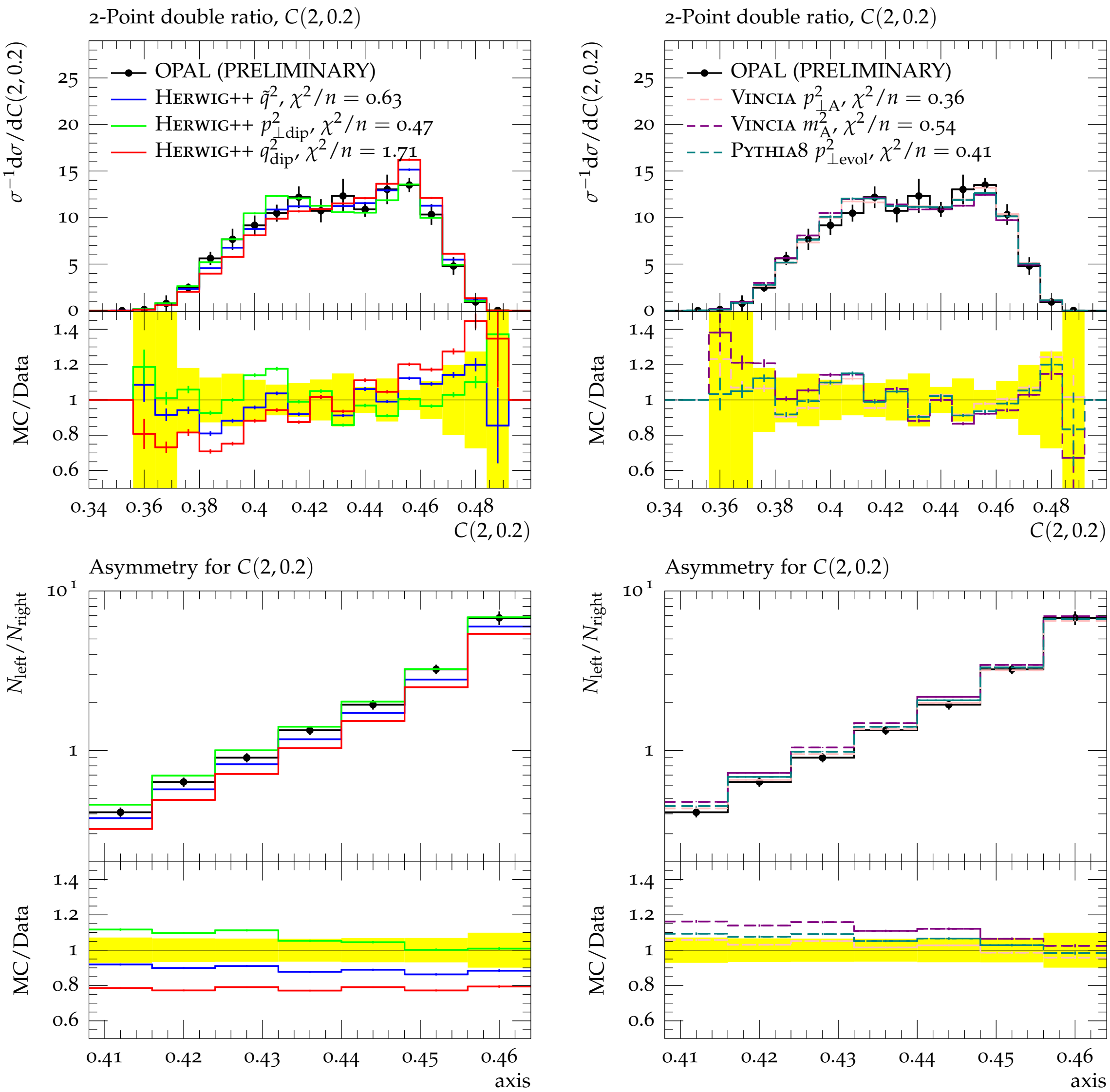


Figure 9.4: The plots show the normalized distribution of the 2-point double ratio and the according asymmetry for sensitivity to the energy of the fourth jet. The plots on the left hand side show the results for the HERWIG++ shower models, the angular-ordered shower (blue) and the dipole shower with ordering in $p^2_{\perp\text{dip}}$ (green) and $q^2_{\text{dip}}$ (red). The predictions of PYTHIA8 (teal) and VINCIA with ordering in $p^2_{\perp\text{A}}$ (pink) and antenna mass (violet) are shown on the right. The ratio plot shows the deviation of the Monte Carlos with respect to the data.

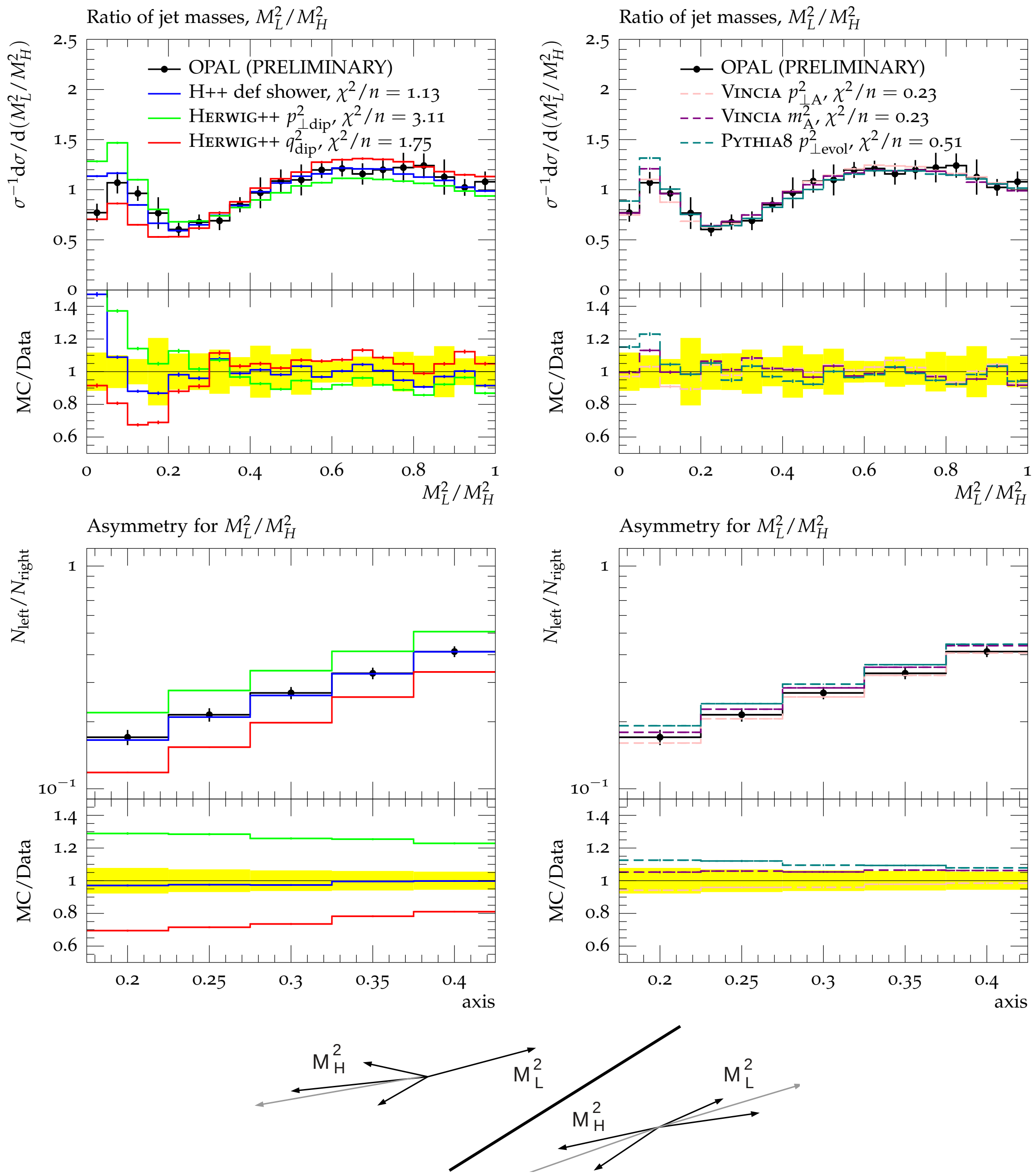


Figure 9.5: The plots show the normalized distribution of the mass ratio and the according asymmetry, where the first bin is excluded. The plots on the left hand side show the results for the HERWIG++ shower models, the angular-ordered shower (blue) and the dipole shower with ordering in $p^2_{\perp\mathrm{dip}}$ (green) and $q^2_{\mathrm{dip}}$ (red). The predictions of PYTHIA8 (teal) and VINCIA with ordering in $p^2_{\perp\mathrm{A}}$ (pink) and antenna mass (violet) are shown on the right. The ratio plot shows the deviation of the Monte Carlos with respect to the data.

the shower produces too many opposite-side and too few same-side events. An interesting feature in HERWIG++ is the preservation of the order of the shower models. Compared to the other shower models, the $p^2_{\perp\mathrm{dip}}$-ordered shower predicts the highest values for the asymmetry of the mass ratio on hadron level as well as on parton level. Corresponding to that, the shower with $q^2_{\mathrm{dip}}$-ordering always predicts the smallest values. Of special interest is the fact that the deviation between the two different evolution variables of the dipole shower is the same for the asymmetry on hadron and on parton level. Therefore, the cluster hadronization model changes the asymmetry of the mass ratio for both ordering variables with the same amount. The predictions of the angular-ordered shower of HERWIG++ for the asymmetry of the ratio of hemisphere masses agree with the data perfectly.

The shower of PYTHIA8 tends to produce too many events with effective $1 \to 3$ splittings. Thus the value of the asymmetry of the ratio of hemisphere masses is high, compared to the data. However, this effect is very small. The predictions of VINCIA lie within the error bars of the data.

The result of the rate of events with effective $1 \to 3$ splittings compared to two $1 \to 2$ splittings each agree for the angular observable $\alpha_{14}$ and for the ratio of jet masses. For both observables non-perturbative effects are visible. The influence of hadronization has been reduced and the reliability of the measurement improved for the mass ratio by excluding the first bin for the calculation of the asymmetry.

## Statistical Tests

To compare the Monte Carlo predictions quantitatively with the OPAL measurements, the Kolmogorov test, a statistical test of compatibility in shape between two histograms, is performed in ROOT [55] for all observables in Tab. 9.1. In addition, the $\chi^2$ test was performed, leading to similar trends as the Kolmogorov test. In this case the $p$-value can be interpreted as the probability that the prediction of the Monte Carlo generators are in conformity with the data. Tab. 9.2 lists the $p$-value for the different shower models for all observables, including both tunes. As discussed in the last section, the effect of hadronization can be reduced and the reliability of the measurement improved by excluding the first bin of the normalized distribution of the mass ratio. Therefore two columns are included for this observable.

The angular-ordered shower of HERWIG++ provides for most parts very good descriptions of the LEP measurements. As discussed before, a parameter of the cluster hadronization model had to be kept fixed throughout the tuning in order to decrease the enhancement for small angles $\alpha_{14}$. These hadronization effects lead to smaller $p$-values for the observables $\alpha_{14}$, $C(2, 0.2)$ and $C(2, 2.0)$, especially for the tune with emphasis on event shapes and jet rates. The ratio of jet masses is described perfectly by this HERWIG++ shower, if the first bin is excluded and thus hadronization effects decreased. The $p$-values for the $p^2_{\perp\mathrm{dip}}$-ordered HERWIG++ dipole shower for the two tunes differ from each other for some observables, but there is no clear trend that one tune is able to describe the LEP measurements better. The angular observables, $\alpha^*$ and $\alpha_{14}$, and 2-point double ratios, which describe the same event topologies as the angular observables, are described well. In contrast, the predictions of the other observables, as for instance the mass ratio, are less compatible with the data. For the $q^2_{\mathrm{dip}}$-ordered HERWIG++ dipole shower the $p$-values of all observables increase when the parameter values of the tune with emphasis on event shapes and jet rates are used. This is consistent with the result of the tuning where the goodness of fit for the event shapes improved considerably for the second tune, compared

| | | $\alpha^*$ | $\alpha_{14}$ | $C(2{,}0.2)$ | $C(2{,}2.0)$ | $M_L^2/M_H^2$ all bins | $M_L^2/M_H^2$ w/o bin1 | $\frac{C_s(1,0.2)}{C_h(1,0.2)}$ | $\frac{C_s(1,2.0)}{C_h(1,2.0)}$ |
|---|---|---|---|---|---|---|---|---|---|
| H++ $\tilde{q}^2$ | T 1 | 0.85 | 0.55 | 0.30 | 0.53 | 0.38 | 1.00 | 0.55 | 0.85 |
| | T 2 | 0.89 | 0.26 | 0.19 | 0.29 | 0.52 | 1.00 | 0.68 | 0.86 |
| H++ $p^2_{\perp\mathrm{dip}}$ | T 1 | 1.00 | 0.22 | 0.54 | 1.00 | 0.00 | 0.01 | 0.00 | 0.00 |
| | T 2 | 1.00 | 0.73 | 1.00 | 0.68 | 0.00 | 0.06 | 0.01 | 0.00 |
| H++ $q^2_{\mathrm{dip}}$ | T 1 | 0.26 | 0.12 | 0.02 | 0.21 | 0.02 | 0.02 | 0.00 | 0.18 |
| | T 2 | 0.54 | 0.95 | 0.16 | 0.51 | 0.04 | 0.08 | 0.01 | 0.35 |
| V $p^2_{\perp\mathrm{A}}$ | T 1 | 1.00 | 0.99 | 1.00 | 1.00 | 1.00 | 1.00 | 1.00 | 1.00 |
| | T 2 | 1.00 | 1.00 | 1.00 | 1.00 | 1.00 | 1.00 | 0.97 | 1.00 |
| V $m^2_{\mathrm{A}}$ | T 1 | 0.97 | 0.24 | 0.15 | 1.00 | 0.95 | 0.98 | 0.34 | 0.82 |
| | T 2 | 0.96 | 0.37 | 0.21 | 1.00 | 0.97 | 0.96 | 0.56 | 0.87 |
| Pythia8 | T 1 | 1.00 | 0.59 | 0.63 | 1.00 | 0.52 | 0.82 | 0.08 | 0.55 |
| | T 2 | 1.00 | 0.75 | 0.68 | 1.00 | 0.41 | 0.72 | 0.09 | 0.44 |

Table 9.2: The table lists the $p$-value of the Kolmogorov test. Herwig++ is abbreviated with H++, Vincia with V. The first lines correspond to the result of the tunes to all observables and the second correspond to the tune with emphasis on event shapes and jet rates. For the mass ratio two columns are included, one where all bins are taken into account and for the other the first bin is excluded.

to the tune to all observables. This groups of observables reflects the structure of multi-jet events, as do the observables investigated here. The $p$-values indicate that the shower with $q^2_{\mathrm{dip}}$-ordering provides good predictions for some observables.

For the $p^2_{\perp\mathrm{A}}$-ordered shower of Vincia all $p$-values are unity or very close to unity. Thus, the predictions of this shower model are perfectly compatible with the LEP measurements for all observables. The mass-ordered shower of Vincia describes the LEP measurements for the majority of observables very well, whereas the predictions of other observables are less compatible with the LEP measurements. The $p$-values of the two tunes do not significantly differ and there is no clear trend that one tune provides a better description of the data. The $p$-values for Pythia8 do not significantly differ between the two tunes. This shower models provides good predictions for all observables, except the ratio $C_s(1,0.2)/C_h(1,0.2)$. The description of the mass ratio is improved when the first bin is excluded.

As an example for the comparison of the two different tunes, the normalized distribution and the ratio of the central to away region of $\alpha_{14}$ are plotted in Fig. 9.6 for Pythia8 and the angular-ordered shower of Herwig++ for both tunes obtained in the last chapter. The plots show that there are no significant changes in the predictions of the two tunes. The enhancement at small angles $\alpha_{14}$ for the angular-ordered shower is more distinct for the tunes with emphasis on event shapes and jet rates, leading to lower values for the ratio of the central to towards region. However, for the ratio where the towards region is not taken into account, the results for both tunes are nearly the same.

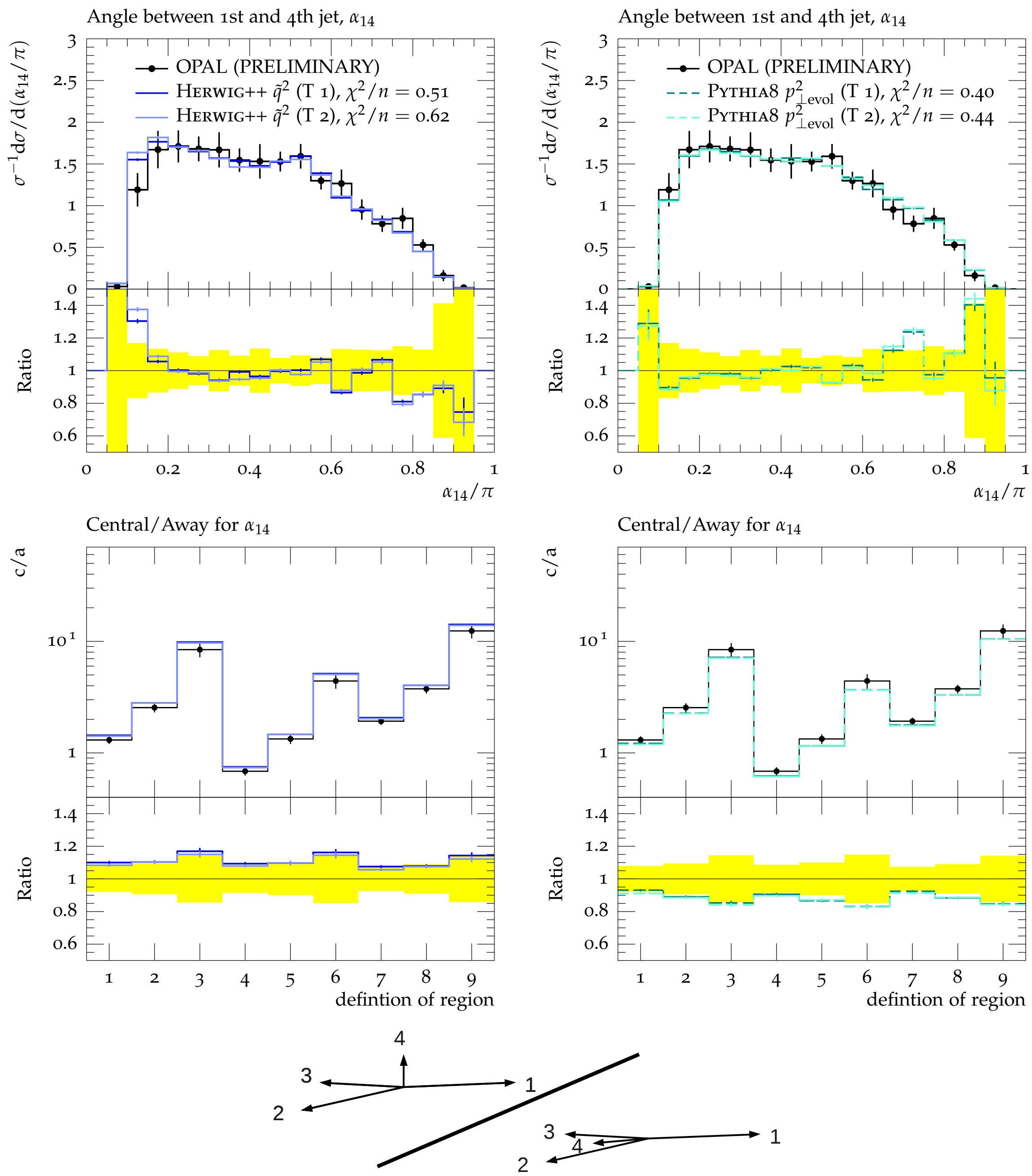


Figure 9.6: The normalized distribution of $\alpha_{14}$ and the ratio of the central to away region are plotted here. The plots on the left hand side show the results for the HERWIG++ angular-ordered shower, used with parameter values obtained by the tune to all observables (dark blue) and by the tune with emphasis on event shapes and jet rates (light blue). On the right hand side the predictions of PYTHIA8 are shown, for the tune to all observables (dark teal) and for the tune with emphasis on event shapes and jet rates (light teal). The ratio plot shows the deviation of the Monte Carlos with respect to the data.

### Conclusions

For both observables, $\alpha_{14}$ and $M_L^2/M_H^2$, non-perturbative effects occur for small values, especially for HERWIG++. To focus on the shower properties, the ratio of the central to away region of $\alpha_{14}$ is used, since the region with small values is excluded. The ratio reproduces the rate of events with effective $1 \to 3$ splittings, leading to events populating the away region of $\alpha_{14}$. The $p^2_{\perp\mathrm{dip}}$-ordered shower of HERWIG++ tends to slightly overestimate this rate, as does PYTHIA8. However, these effects are small and not very significant. The $q^2_{\mathrm{dip}}$-ordered shower shows a deviation of about two sigma in underestimating the amount of events in the away region. The asymmetry of the ratio of hemisphere masses reflects the relative amount of events with effective $1 \to 3$ splittings, compared to the event rate with two $1 \to 2$ splittings each. The conclusions for this observable confirm the results of the angular observable $\alpha_{14}$.

In conclusion, observables like the mass ratio and its asymmetry can be used to tell the shower models apart. This was revealed by the different predictions for these observables, as seen for instance in Fig. 9.5, as well as by the compatibility test.

## 9.3 Strong and Smooth Ordering in Vincia

In order to compare the ordering condition in VINCIA, see Sec. 5.2.2, additional tunes for VINCIA with smooth ordering for both evolution variables, antenna transverse momentum and antenna mass, are performed. The resulting parameter values can be found in Tab. A.19 in the appendix. In this section, the shower models are used with the parameter values obtained by the tune to all observables.

Fig. 9.7 shows a comparison between strong and smooth ordering for the $p^2_{\perp\mathrm{A}}$-ordered shower of VINCIA. The $\chi^2$-values for the normalized distributions for both observables, $\alpha_{14}$ and $M_L^2/M_H^2$, indicate that the sensitivity of the observables to the ordering condition is vanishingly low. The asymmetries, especially the one for the mass ratio, show slightly different results. The strongly-ordered shower produces more events where the clustering of the next jets happens on opposite sides, which leads to smaller values for the asymmetry. Despite the differences, the results of both ordering conditions lie within the error bars of the data.

The same histograms are shown in Fig. 9.8 to compare the effect of strong and smooth ordering within the mass-ordered VINCIA shower. As for the shower with ordering in transverse momentum the ordering condition has only vanishingly low influence on the distribution of the mass ratio. Both results of the Monte Carlo predictions lie either inside or just outside of the error band of the data. However the angle between the first and fourth jet shows higher sensitivity to the ordering condition for the mass-ordered shower. The strongly-ordered shower describes the normalized distribution of this observable better than the shower with smooth ordering, as indicated by the $\chi^2$-values. The same holds for the central over towards region due to the population of the phase space by the mass-ordered shower. This can be seen in the diagram in the middle of Fig. 5.3. The shower prefers soft wide-angle emissions over collinear ones. If the shower is smoothly-ordered, slightly unordered emissions are possible. Thus the smoothly-ordered shower does not get “as far” in phase space as the strongly-ordered shower and the relative amount of wide-angle emissions to collinear ones increases.

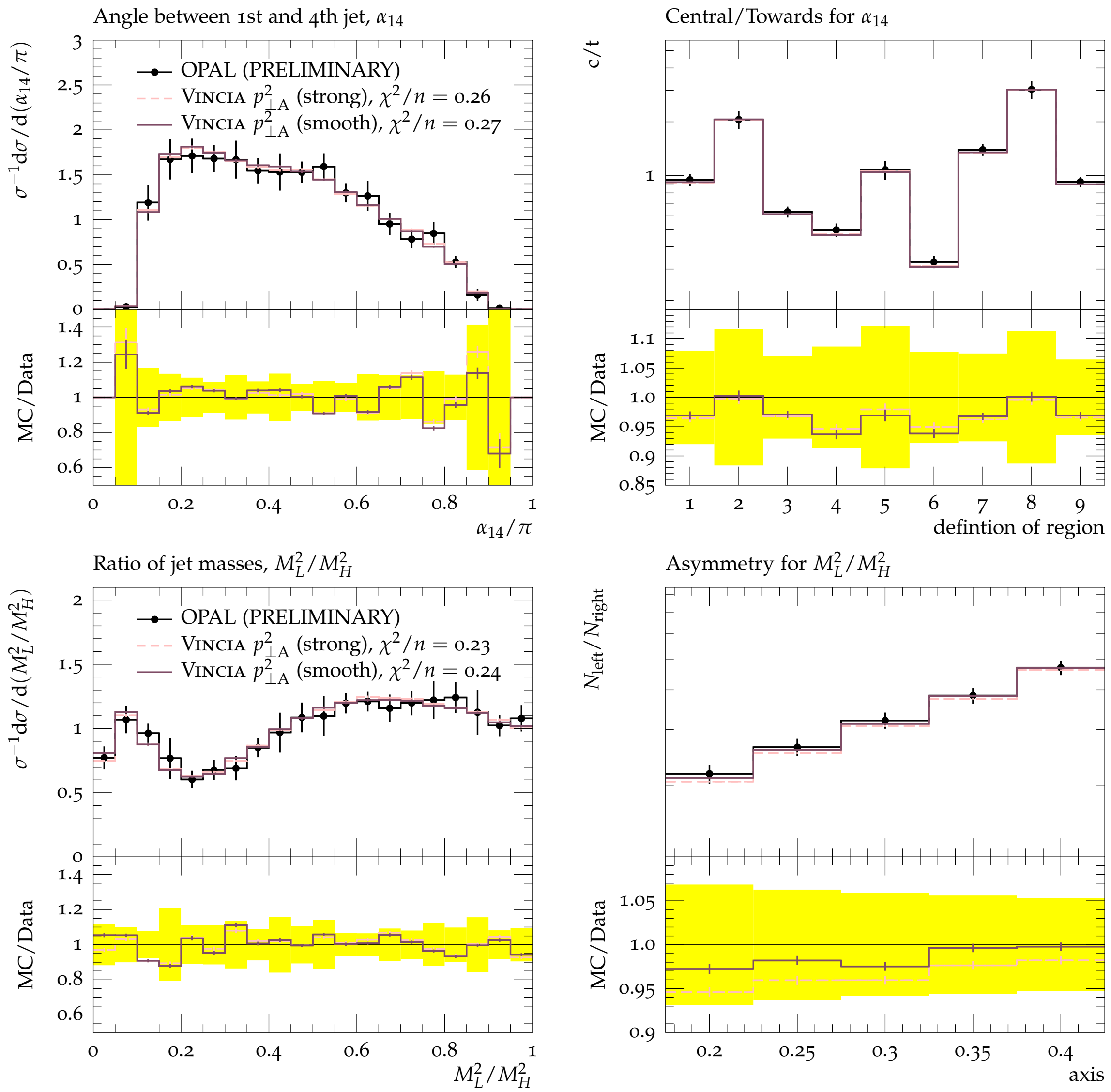


Figure 9.7: The plots show a comparison between strong (pink dashed line) and smooth (purple solid line) ordering for the $p^2_{\perp A}$-ordered shower of VINCIA with OPAL data: The upper plots show the normalized distribution of $\alpha_{14}$ on the left as well as the central over towards region on the right, as an example for the ratios. The normalized distribution of the mass ratio $M_L^2/M_H^2$ and the asymmetry are shown in the lower plots.

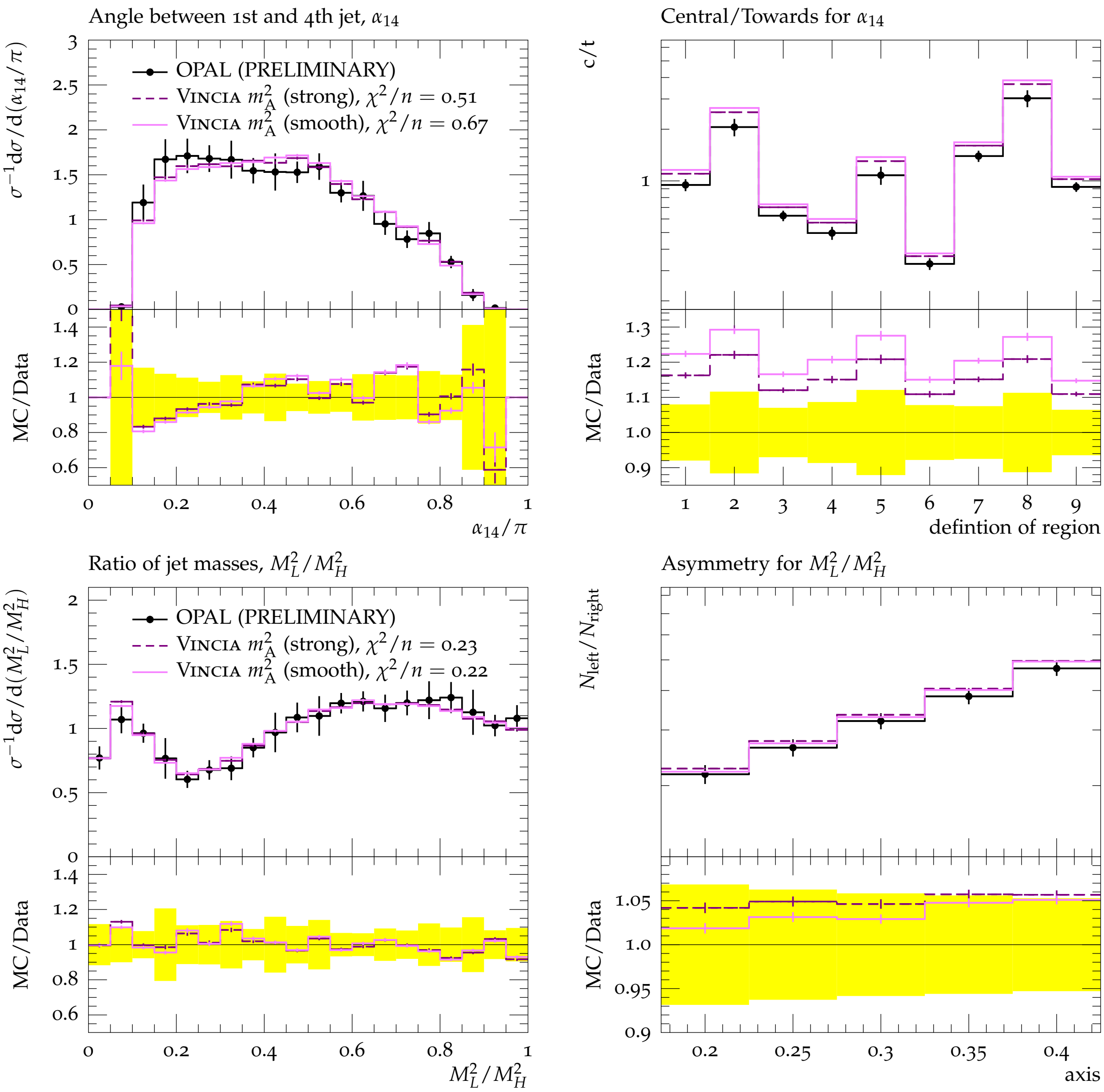


Figure 9.8: The plots show a comparison between strong (darker dashed line) and smooth (lighter solid line) ordering for the mass-ordered shower of VINCIA with OPAL data: The upper plots show the normalized distribution of $\alpha_{14}$ on the left as well as the central over towards region on the right, as an example for the ratios. The normalized distribution of the mass ratio $M_L^2/M_H^2$ and the asymmetry are shown in the lower plots.

## 9.4 Matching

To check the effect of including higher orders in the Monte Carlo event generators, additional tunes for VINCIA and the dipole shower of HERWIG++ were performed. The terminology of the matching procedure is given in Sec. 5.3. The parameter values obtained by the additional tunes can be found in Tab. A.20 for VINCIA and Tab. A.21 for HERWIG++ in the appendix. Note that the matrix-element correction in VINCIA only works correct when used with smooth ordering. In this section the shower models are used with the parameter values obtained by the tunes to all observables.

Fig. 9.9 compares the use of the VINCIA $p^2_{\perp\mathrm{A}}$-ordered shower with the default matching of PYTHIA8 to the same shower model with additional matrix-element corrections. The latter leads to LO accuracy for the fourth jet. The plots for the normalized distributions of $\alpha_{14}$ and $M_L^2/M_H^2$ show that there is no overall improvement when additional matching is used. The angle $\alpha_{14}$ gets slightly better described with additional matrix-element corrections whereas the mass ratio $M_L^2/M_H^2$ gets slightly worse. The asymmetries, shown on the right side of Fig. 9.9, agree with that. For the shower with additional matching as well as for the shower with the default matching of PYTHIA8, the prediction of the Monte Carlo lies within the error bars of the data.

The same plots are shown again in Fig. 9.10 for the $p^2_{\perp\mathrm{dip}}$-ordered dipole shower of HERWIG++. They lead basically to the same conclusions as for VINCIA. The normalized distribution of $\alpha_{14}$ gets slightly better described with the NLO version of the shower and the mass ratio $M_L^2/M_H^2$ gets slightly worse. The same holds for the asymmetries. For the central over towards region both predictions lie within the error bands of the data, whereas the asymmetry of the mass ratio both do not.

It is well known that the influence of matching in $e^+e^-$-collisions is small. For instance, the NLO corrections to the HERWIG++ dipole shower are small and the dipole splitting functions already coincide with the real emission matrix element very well. Nevertheless, the Monte Carlo event generators gain an improvement from matching in $e^+e^-$-collisions in the sense that the parameter values of the shower model get more physical. The strong coupling at the $Z^0$-pole gets closer to the measured value and the shower cutoff reaches a higher value when higher order corrections are implemented. This can be verified by checking the corresponding values in Tab. A.6 for the LO $p^2_{\perp\mathrm{dip}}$-ordered dipole shower of HERWIG++ and Tab. A.21 for NLO version.

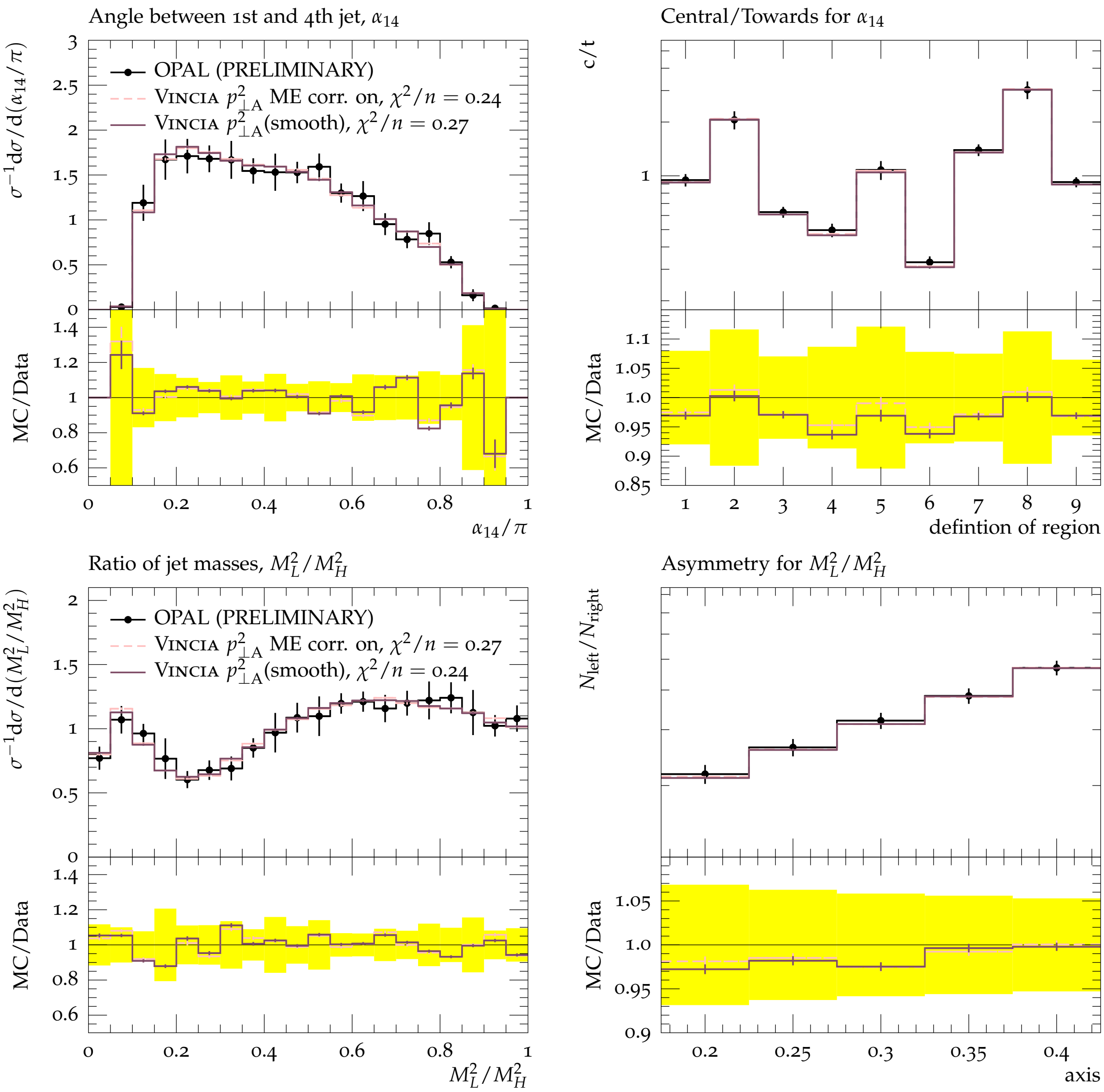


Figure 9.9: The plots show a comparison for the $p^2_{\perp\mathrm{A}}$-ordered shower of VINCIA with OPAL data when used with additional matrix-element correction for LO accuracy for the fourth jet (pink dashed line) and with the default PYTHIA8 matching (purple solid line): The upper plots show the normalized distribution of $\alpha_{14}$ on the left together with the central over towards region on the right, as an example for the ratios. The normalized distribution of the mass ratio $M_L^2/M_H^2$ and the asymmetry are shown in the lower plots.

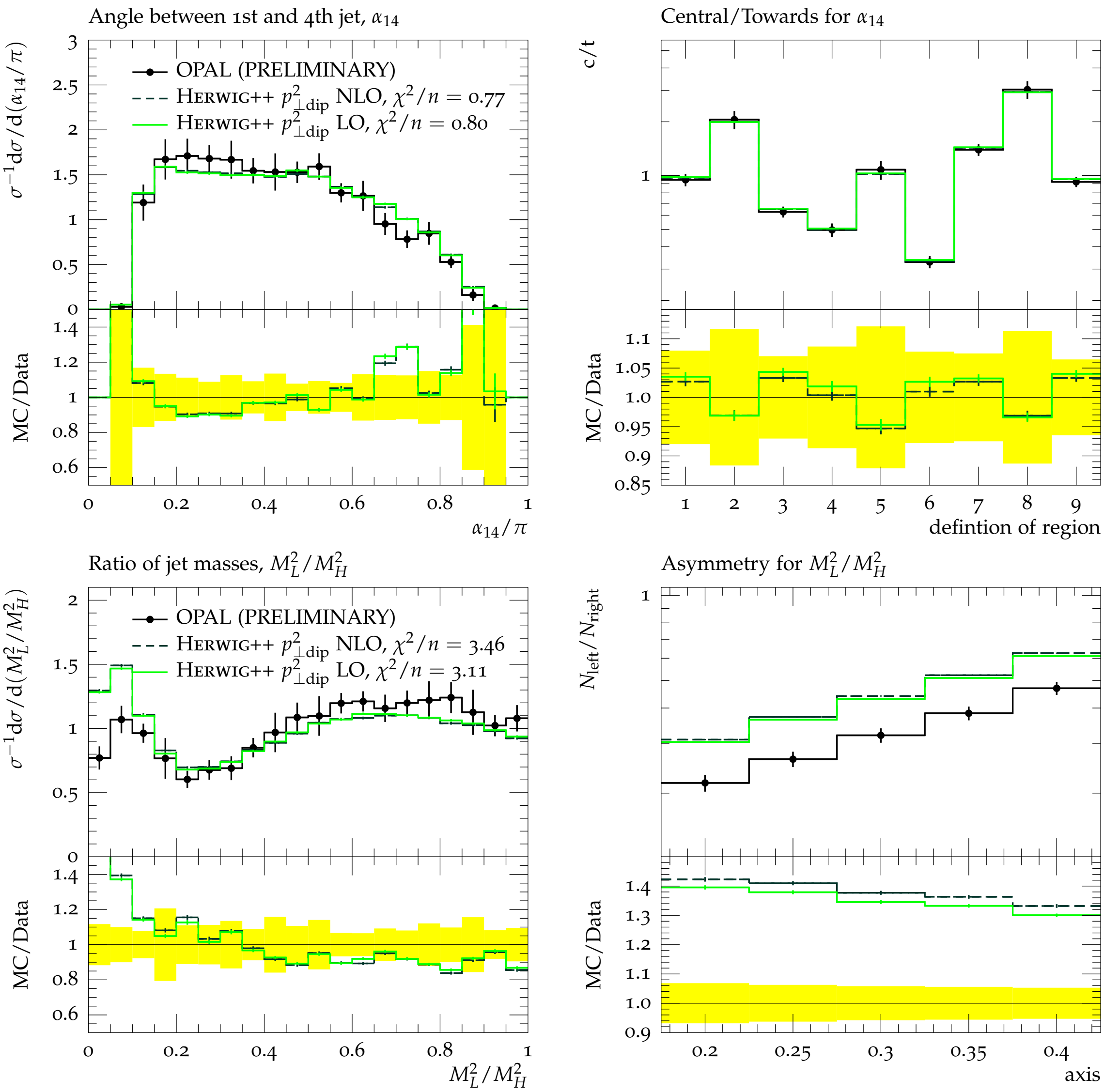


Figure 9.10: The plots show a comparison for the $p^2_{\perp\mathrm{dip}}$-ordered shower of VINCIA with OPAL data when used with NLO (darker dashed line) and LO (lighter solid line) accuracy: The upper plots show the normalized distribution of $\alpha_{14}$ on the left together with the central over towards region on the right, as an example for the ratios. The normalized distribution of the mass ratio $M_L^2/M_H^2$ and the asymmetry are shown in the lower plots.

# 10. Summary and Conclusions

The aim of this work was to analyze QCD properties, such as colour coherence or the emission of soft jets. Since these properties manifest themselves in the implementation of the shower algorithm in Monte Carlo event generators, different shower models are investigated and compared. On the one hand, the traditional parton shower approach has been used for decades. This algorithm is based on $1 \to 2$ splittings and is implemented for instance in Herwig++ with angular ordering or in Pythia8 with angular vetos. On the other hand, new approaches with $2 \to 3$ splittings become established, using Catani-Seymour partitioned dipoles like the Herwig++ dipole shower or antenna functions like Vincia. The choice of radiation function differs from model to model. Furthermore, the choice of evolution variable, such as transverse momentum or virtuality, depends on the model, as does the phase-space mapping, also known as recoil strategy.

The observables, which are used in this thesis to investigate shower properties, are sensitive to QCD colour coherence and angular ordering or to effective $1 \to 3$ splitting kernels and jet substructure. Event selection cuts are defined in a way to minimize disruptive influences of hadronization and $B$ decays. For Herwig++ large enhancements in the observable $\alpha_{14}$ showed up due to these disruptive effects. They were taken care of throughout the tuning. However, they were not be reduced completely. For all shower models, non-perturbative effects are visible for small values of the ratio of jet masses since massless partons after the termination of the parton shower exist on parton level. In addition to the normalized distributions of the observables, different definitions of the asymmetry for the variables are used. These asymmetries provide clear and easy tools that allow statements concerning the relative amounts of different types of emissions or event configurations.

To ensure a fair comparison of the different shower models, the main free parameters of the theoretical models are constrained by using existing LEP measurements. This procedure is referred to as generator tuning. In this work the parameters of the different shower models, the strong coupling and the shower cutoff, are tuned together with the main parameters of either the cluster hadronization model in Herwig++ or the Lund string model in Pythia8. For all shower models the same set of LEP data is used, including event shapes, jet rates, identified particle spectra, $b$ quark fragmentation functions and mean particle multiplicities. The main result of the generator tuning is the goodness of fit function. Since all LEP measurements use event samples of either Pythia6 or Jetset for the detector correction, the shower models of Pythia8 and Vincia might gain advantage over Herwig++, although the experiments claim to be independent of the underlying Monte Carlo generator for the detector corrections within the experimental systematics. Under the given conditions, Vincia with ordering in transverse momentum provides the best description of experimental LEP data.

After measuring the new observables with OPAL data, the results are compared with the predictions of the Monte Carlo event generators. Besides a few exceptions, the simulations provide good and consistent descriptions. The deviation between experimental data and Monte Carlo predictions are small with two sigma effects at most. The results of both observables, the angle between jets, $\alpha_{14}$, and the ratio of hemisphere masses, $M_L^2/M_H^2$, agree with each other. The rate of events with effective $1 \to 3$ splittings, leading to high values for $\alpha_{14}$ and small values for $M_L^2/M_H^2$, is slightly overestimated by Pythia8 and the $p_{\perp\mathrm{dip}}^2$-ordered shower of Herwig++. In contrast, the $q_{\mathrm{dip}}^2$-ordered shower shows about a two sigma deviation in underestimating the amount of effective $1 \to 3$ splittings. However, the visible effects are small and both observables show sensitivity to non-perturbative effects, especially for small values of the variables.

A special feature in Vincia is the possibility of using strong and smooth ordering for the same evolution variable. The effect of this ordering condition was investigated with the new observables. The latter did not provide enough information to draw a clear statement, if strong or smooth ordering for the shower is the more physical choice. For the dipole shower of Herwig++ the pure shower and the shower matched to higher order matrix elements was compared as well. As expected the influence of matching in $e^+e^-$-collisions is small since the NLO corrections are small and the dipole splitting functions in Herwig++ already coincide with the real emission matrix element very well. However, the Monte Carlo event generator gains an improvement from matching in the sense that the parameter values of the shower model get more physical, as shown for the dipole shower of Herwig++ with ordering in $p_{\perp\mathrm{dip}}^2$. The influence of the additional tree-level matching in Vincia for LO accuracy for the fourth jet is small as well.

It was not possible to tell the shower models of Vincia and Pythia8 apart with the help of former LEP measurements. This task was accomplished with the new observables. The two ordering variables of Vincia, transverse momentum and antenna mass, provide different predictions for the ratio of different regions of the angular observable $\alpha_{14}$. The asymmetry of the ratio of hemisphere masses can be used to tell Vincia and Pythia8 apart. These conclusions are additionally verified with the Kolmogorov test, a statistical test of compatibility in shape, performed within this work to check the compatibility between the new LEP measurements and the Monte Carlo predictions.

As mentioned above, Pythia8 and Vincia might gain advantage over Herwig++, for both, tuning and the description of the new measurements. To ensure a completely fair treatment for Herwig++ as well, the tuning procedure and the comparison between the Monte Carlo generators and LEP data in terms of the new observables should be repeated. The same LEP data set has to be used in the tuning process, but for the detector correction in all measurements Herwig has to be applied instead of Pythia6. Following this, Herwig should be used for the central value of the new measurements and the deviation to Pythia6 will then contribute to the systematical error. By comparing the outcome of the described procedure with the results in this thesis, a clear statement can be issued about how well the different theory models are able to describe existing LEP measurements and QCD properties, tested with the new observables.

# A. Tuning

## Tuning Observables

The following Tabs. A.1-A.5 list the observables and the according weights for the complete tune to all observables (column T 1) and for the tunes with emphasis on event shapes and jet rates (column T 2) used during the tuning process.

| Observable | Weight | | Observable | Weight | |
|---|---|---|---|---|---|
| | T 1 | T 2 | | T 1 | T 2 |
| $K^{*\pm}(892)$ spectrum | 1.0 | 1.0 | $\Lambda^0$ spectrum | 1.0 | 1.0 |
| $\rho$ spectrum | 1.0 | 1.0 | $\pi^0$ spectrum | 1.0 | 1.0 |
| $\omega(782)$ spectrum | 1.0 | 1.0 | $p$ spectrum | 1.0 | 1.0 |
| $\Xi^-$ spectrum | 1.0 | 1.0 | $\eta'$ spectrum | 1.0 | 1.0 |
| $K^{*0}$ spectrum | 1.0 | 1.0 | $\Xi^0(1530)$ spectrum | 1.0 | 1.0 |
| $\phi$ spectrum | 1.0 | 1.0 | $\pi^\pm$ spectrum | 1.0 | 1.0 |
| $\Sigma^\pm$ spectrum | 1.0 | 1.0 | $\eta$ spectrum | 1.0 | 1.0 |
| $\gamma$ spectrum | 1.0 | 1.0 | $K^0$ spectrum | 1.0 | 1.0 |
| $K^\pm$ spectrum | 1.0 | 1.0 | | | |

Table A.1: Identified particle spectra and the associated weights, taken from Ref. [46].

| Observable | Weight | | Observable | Weight | |
|---|---|---|---|---|---|
| | T 1 | T 2 | | T 1 | T 2 |
| Differential 2-jet rate | 2.0 | 10.0 | Differential 4-jet rate | 2.0 | 10.0 |
| Differential 3-jet rate | 2.0 | 10.0 | Differential 5-jet rate | 2.0 | 10.0 |

Table A.2: Jet rates and the associated weights, taken from Ref. [47].

| Observable | Weight T 1 | Weight T 2 | Observable | Weight T 1 | Weight T 2 |
|---|---|---|---|---|---|
| Mean $\rho^0(770)$ multiplicity | 10.0 | 0.0 | Mean $\chi_{c1}(3510)$ multiplicity | 10.0 | 0.0 |
| Mean $\Delta^{++}(1232)$ multiplicity | 10.0 | 0.0 | Mean $D^+$ multiplicity | 10.0 | 0.0 |
| Mean $K^{*+}(892)$ multiplicity | 10.0 | 0.0 | Mean $\Sigma^+$ multiplicity | 10.0 | 0.0 |
| Mean $\Sigma^0$ multiplicity | 10.0 | 0.0 | Mean $f_1(1285)$ multiplicity | 10.0 | 0.0 |
| Mean $\Lambda_b^0$ multiplicity | 10.0 | 0.0 | Mean $f_2(1270)$ multiplicity | 10.0 | 0.0 |
| Mean $K^+$ multiplicity | 10.0 | 0.0 | Mean $J/\psi(1S)$ multiplicity | 10.0 | 0.0 |
| Mean $\Xi^0(1530)$ multiplicity | 10.0 | 0.0 | Mean $B_u^+$ multiplicity | 10.0 | 0.0 |
| Mean $\Lambda(1520)$ multiplicity | 10.0 | 0.0 | Mean $B^**$ multiplicity | 10.0 | 0.0 |
| Mean $D_s^{*+}(2112)$ multiplicity | 10.0 | 0.0 | Mean $\Lambda_c^+$ multiplicity | 10.0 | 0.0 |
| Mean $\Sigma^-(1385)$ multiplicity | 10.0 | 0.0 | Mean $D^0$ multiplicity | 10.0 | 0.0 |
| Mean $f_1(1420)$ multiplicity | 10.0 | 0.0 | Mean $f_2'(1525)$ multiplicity | 10.0 | 0.0 |
| Mean $\phi(1020)$ multiplicity | 10.0 | 0.0 | Mean $\Sigma^\pm$ multiplicity | 10.0 | 0.0 |
| Mean $K_2^{*0}$ multiplicity | 10.0 | 0.0 | Mean $D_{s2}^+$ multiplicity | 10.0 | 0.0 |
| Mean $\Omega^-$ multiplicity | 10.0 | 0.0 | Mean $K^{*0}(892)$ multiplicity | 10.0 | 0.0 |
| Mean $\Sigma^\pm(1385)$ multiplicity | 10.0 | 0.0 | Mean $\Sigma^-$ multiplicity | 10.0 | 0.0 |
| Mean $\psi(2S)$ multiplicity | 10.0 | 0.0 | Mean $\pi^+$ multiplicity | 10.0 | 0.0 |
| Mean $D^{*+}$ multiplicity | 10.0 | 0.0 | Mean $f_0(980)$ multiplicity | 10.0 | 0.0 |
| Mean $B^*$ multiplicity | 10.0 | 0.0 | Mean $\Sigma^+(1385)$ multiplicity | 10.0 | 0.0 |
| Mean $\pi^0$ multiplicity | 10.0 | 0.0 | Mean $D_s^+$ multiplicity | 10.0 | 0.0 |
| Mean $\eta$ multiplicity | 10.0 | 0.0 | Mean $p$ multiplicity | 10.0 | 0.0 |
| Mean $a_0^+(980)$ multiplicity | 10.0 | 0.0 | Mean $B_s^0$ multiplicity | 10.0 | 0.0 |
| Mean $D_{s1}^+$ multiplicity | 10.0 | 0.0 | Mean $K^0$ multiplicity | 10.0 | 0.0 |
| Mean $\rho^+(770)$ multiplicity | 10.0 | 0.0 | Mean $B^+, B_d^0$ multiplicity | 10.0 | 0.0 |
| Mean $\Xi^-$ multiplicity | 10.0 | 0.0 | Mean $\Lambda$ multiplicity | 10.0 | 0.0 |
| Mean $\omega(782)$ multiplicity | 10.0 | 0.0 | Mean $\eta'(958)$ multiplicity | 10.0 | 0.0 |
| Mean $\Upsilon(1S)$ multiplicity | 10.0 | 0.0 | | | |

Table A.3: Multiplicities and the associated weights, taken from Ref. [48].

| Observable | Weight T 1 | Weight T 2 |
|---|---|---|
| $b$ quark fragmentation function $f(x_B^{\text{weak}})$ | 7.0 | 35.0 |
| Mean of $b$ quark fragmentation function $f(x_B^{\text{weak}})$ | 3.0 | 15.0 |

Table A.4: Observables for $b$ quarks and the associated weights, taken from Ref. [45].

| Observable | Weight | |
|---|---|---|
| | T 1 | T 2 |
| In-plane $p_\perp$ in GeV w.r.t. sphericity axes | 1.0 | 5.0 |
| In-plane $p_\perp$ in GeV w.r.t. thrust axes | 1.0 | 5.0 |
| Out-of-plane $p_\perp$ in GeV w.r.t. sphericity axes | 1.0 | 5.0 |
| Out-of-plane $p_\perp$ in GeV w.r.t. thrust axes | 1.0 | 5.0 |
| Mean out-of-plane $p_\perp$ in GeV w.r.t. thrust axis vs. $x_p$ | 1.0 | 5.0 |
| Mean $p_\perp$ in GeV vs. $x_p$ | 1.0 | 5.0 |
| Scaled momentum $x_p = \|p\|/\|p_{\mathrm{beam}}\|$ | 1.0 | 5.0 |
| Log of scaled momentum, $\log(1/x_p)$ | 1.0 | 5.0 |
| Energy-energy correlation, EEC | 1.0 | 5.0 |
| Sphericity, $S$ | 1.0 | 5.0 |
| Aplanarity, $A$ | 2.0 | 10.0 |
| Planarity, $P$ | 1.0 | 5.0 |
| $D$ parameter | 1.0 | 5.0 |
| $C$ parameter | 1.0 | 5.0 |
| 1-Thrust | 1.0 | 5.0 |
| Thrust major, $M$ | 1.0 | 5.0 |
| Thrust minor, $m$ | 2.0 | 10.0 |
| Oblatness, $O = M - m$ | 1.0 | 5.0 |
| Charged multiplicity distribution | 2.0 | 10.0 |
| Mean charged multiplicity | 150.0 | 750.0 |

Table A.5: Observables and the associated weights, taken from Ref. [46] and [44].

# Parameter Values

| | Default | Range | Herwig++ $\tilde{q}^2$ Tune 1 | Tune 2 |
|---|---|---|---|---|
| $\alpha_{M_Z}$ | 0.120 | $0.100 - 0.125$ | 0.123 | 0.123 |
| $p_\mathrm{T}^\mathrm{min}$ | 1.00 GeV | $(0.50 - 1.50)$ GeV | 1.39 GeV | 1.50 GeV |
| $m_{g,c}$ | 0.95 GeV | $(0.67 - 3.00)$ GeV | 0.70 GeV | 0.70 GeV |
| $\mathrm{Cl}_\mathrm{max}$ | 3.25 GeV | $(2.00 - 4.50)$ GeV | 3.59 GeV | 3.73 GeV |
| $\mathrm{Cl}_\mathrm{pow}$ | 1.28 | $2.00 - 10.00$ | 2.59 | 3.74 |
| $P_\mathrm{split}$ | 1.14 | fixed | 0.60 | 0.60 |

| | Default | Range | Herwig++ $p^2_{\perp\mathrm{dip}}$ Tune 1 | Tune 2 | Herwig++ $q^2_\mathrm{dip}$ Tune 1 | Tune 2 |
|---|---|---|---|---|---|---|
| $\alpha_{M_Z}$ | 0.113 | $0.100 - 0.138$ | 0.128 | 0.128 | 0.138 | 0.133 |
| $\mu_{\mathrm{IR},FF}$ | 1.41 GeV | $(0.50 - 2.00)$ GeV | 0.78 GeV | 0.95 GeV | 0.72 GeV | 0.98 GeV |
| $\mu_{\mathrm{soft},FF}$ | 0.24 GeV | fixed | 0.00 GeV | 0.00 GeV | 0.00 GeV | 0.00 GeV |
| $m_{g,c}$ | 1.08 GeV | $(0.67 - 3.00)$ GeV | 0.70 GeV | 0.70 GeV | 0.96 GeV | 2.30 GeV |
| $\mathrm{Cl}_\mathrm{max}$ | 4.17 GeV | $(2.00 - 4.50)$ GeV | 3.12 GeV | 3.36 GeV | 2.73 GeV | 2.98 GeV |
| $\mathrm{Cl}_\mathrm{pow}$ | 5.73 | $2.00 - 10.00$ | 5.72 | 4.91 | 2.00 | 10.0 |
| $P_\mathrm{split}$ | 0.77 | $0.00 - 1.40$ | 0.74 | 0.76 | 1.33 | 0.73 |

| | Default | Range | Vincia $p^2_{\perp\mathrm{A}}$ Tune 1 | Tune 2 | Vincia $m^2_\mathrm{A}$ Tune 1 | Tune 2 |
|---|---|---|---|---|---|---|
| $\alpha_S$ | 0.129 | $0.120 - 0.132$ | 0.132 | 0.132 | 0.132 | 0.132 |
| $p^{2\ \mathrm{min}}_{\perp\mathrm{A}}$ | 0.60 | $0.46 - 1.00$ | 0.65 | 0.54 | 0.84 | 0.64 |
| $a_\mathrm{L}$ | 0.38 | $0.20 - 0.70$ | 0.26 | 0.20 | 0.47 | 0.33 |
| $b_\mathrm{L}$ | 0.90 | $0.50 - 1.50$ | 0.74 | 0.71 | 0.82 | 0.76 |
| $a_\mathrm{ED}$ | 1.00 | $0.50 - 0.10$ | 0.93 | 0.92 | 0.50 | 0.50 |
| $\sigma$ | 0.275 | $0.200 - 0.400$ | 0.270 | 0.268 | 0.294 | 0.292 |

| | Default | Range | Pythia8 $p^2_{\perp\mathrm{evol}}$ $p^2_{\perp\mathrm{evol}}$ Tune 1 | Tune 2 |
|---|---|---|---|---|
| $\alpha_S$ | 0.138 | $0.120 - 0.139$ | 0.139 | 0.139 |
| $p^{2\ \mathrm{min}}_{\perp\mathrm{evol}}$ | 0.40 | $0.40 - 1.00$ | 0.41 | 0.40 |
| $a_\mathrm{L}$ | 0.30 | $0.20 - 0.70$ | 0.35 | 0.42 |
| $b_\mathrm{L}$ | 0.80 | $0.50 - 1.50$ | 0.94 | 1.05 |
| $a_\mathrm{ED}$ | 0.50 | $0.50 - 0.10$ | 0.95 | 0.83 |
| $\sigma$ | 0.304 | $0.200 - 0.400$ | 0.284 | 0.285 |

Table A.6: The tables list the parameters with their default value and the scanned range for the tuning. The last columns contain the values of the parameters obtained by the best tunes for either the first tune to all observables or the second tune with emphasis on the event shapes and jet rates.

# $\chi^2/N_{\mathbf{dof}}$ Values for Each Observable

The following Tabs. A.7-A.18 list the values of the goodness of fit function per degree of freedom $\chi^2/N_{\mathrm{dof}}$ for each of the observables used during the tuning process. After the first two columns denoting the weights five columns for each shower follow: The $\chi^2/N_{\mathrm{dof}}$ values for the shower with its default parameters and for the shower with tuned parameters for the four different tunes.

| | Weight | | Herwig++ $\tilde{q}^2$ | | | Herwig++ $p^2_{\perp\mathrm{dip}}$ | | | Herwig++ $q^2_{\mathrm{dip}}$ | | |
|---|---|---|---|---|---|---|---|---|---|---|---|
| Observable | T1 | T2 | Def. | T1 | T2 | Def. | T1 | T2 | Def. | T1 | T2 |
| $K^{*\pm}(892)$ spectrum | 1.0 | 1.0 | 0.6 | 0.6 | 0.6 | 2.9 | 0.6 | 0.9 | 2.3 | 1.2 | 6.3 |
| $\rho$ spectrum | 1.0 | 1.0 | 4.9 | 4.4 | 4.5 | 9.3 | 5.7 | 6.8 | 9.1 | 5.4 | 8.6 |
| $\omega(782)$ spectrum | 1.0 | 1.0 | 0.3 | 1.6 | 1.7 | 5.5 | 2.2 | 2.4 | 5.7 | 1.4 | 5.2 |
| $\Xi^-$ spectrum | 1.0 | 1.0 | 10.4 | 7.4 | 8.1 | 1157.3 | 22.5 | 20.1 | 1089.5 | 84.1 | 26.8 |
| $K^{*0}$ spectrum | 1.0 | 1.0 | 1.1 | 1.4 | 1.4 | 4.2 | 2.1 | 2.1 | 3.2 | 1.4 | 5.9 |
| $\phi$ spectrum | 1.0 | 1.0 | 4.2 | 4.0 | 3.6 | 6.4 | 3.2 | 3.3 | 5.7 | 3.7 | 12.5 |
| $\Sigma^\pm$ spectrum | 1.0 | 1.0 | 4.7 | 4.1 | 3.8 | 253.0 | 16.3 | 46.8 | 247.8 | 7.0 | 20.2 |
| $\gamma$ spectrum | 1.0 | 1.0 | 1.8 | 1.7 | 1.8 | 10.3 | 2.9 | 4.5 | 10.7 | 2.6 | 6.4 |
| $K^\pm$ spectrum | 1.0 | 1.0 | 10.1 | 8.1 | 10.1 | 153.3 | 55.3 | 63.2 | 122.0 | 60.2 | 242.4 |
| $\Lambda^0$ spectrum | 1.0 | 1.0 | 113.7 | 47.9 | 52.8 | 3230.3 | 73.0 | 310.4 | 3118.4 | 66.7 | 140.0 |
| $\pi^0$ spectrum | 1.0 | 1.0 | 1.1 | 2.1 | 2.2 | 3.7 | 1.1 | 1.7 | 3.4 | 1.2 | 2.1 |
| $p$ spectrum | 1.0 | 1.0 | 10.2 | 9.1 | 6.8 | 268.6 | 13.1 | 59.2 | 216.8 | 9.7 | 8.1 |
| $\eta'$ spectrum | 1.0 | 1.0 | 4.6 | 3.3 | 3.3 | 4.0 | 3.3 | 3.7 | 3.7 | 4.1 | 3.3 |
| $\Xi^0(1530)$ spectrum | 1.0 | 1.0 | 10.1 | 8.1 | 10.1 | 153.3 | 55.3 | 63.2 | 122.0 | 60.2 | 242.4 |
| $\pi^\pm$ spectrum | 1.0 | 1.0 | 25.9 | 30.5 | 30.0 | 134.1 | 36.5 | 55.0 | 164.2 | 29.0 | 91.9 |
| $\eta$ spectrum | 1.0 | 1.0 | 9.4 | 5.4 | 5.7 | 10.1 | 4.4 | 6.6 | 8.3 | 6.0 | 3.8 |
| $K^0$ spectrum | 1.0 | 1.0 | 7.9 | 7.2 | 9.2 | 112.1 | 38.2 | 44.1 | 86.9 | 48.5 | 293.7 |

Table A.7: $\chi^2/N_{\mathrm{dof}}$ values for identified particle spectra for the Herwig++ showers.

| Observable | Weight T1 | Weight T2 | VINCIA $p^2_{\perp\mathrm{A}}$ Def. | VINCIA $p^2_{\perp\mathrm{A}}$ T1 | VINCIA $p^2_{\perp\mathrm{A}}$ T2 | VINCIA $m^2_{\mathrm{A}}$ Def. | VINCIA $m^2_{\mathrm{A}}$ T1 | VINCIA $m^2_{\mathrm{A}}$ T2 | PYTHIA8 $p^2_{\perp\mathrm{evol}}$ Def. | PYTHIA8 $p^2_{\perp\mathrm{evol}}$ T1 | PYTHIA8 $p^2_{\perp\mathrm{evol}}$ T2 |
|---|---|---|---|---|---|---|---|---|---|---|---|
| $K^{*\pm}(892)$ spectrum | 1.0 | 1.0 | 0.6 | 0.7 | 0.7 | 0.8 | 0.7 | 0.7 | 0.5 | 0.6 | 0.6 |
| $\rho$ spectrum | 1.0 | 1.0 | 2.9 | 3.2 | 3.2 | 2.7 | 2.9 | 3.1 | 1.1 | 1.1 | 1.1 |
| $\omega(782)$ spectrum | 1.0 | 1.0 | 1.3 | 0.9 | 0.8 | 2.4 | 1.7 | 1.5 | 4.5 | 4.7 | 4.5 |
| $\Xi^-$ spectrum | 1.0 | 1.0 | 1.9 | 1.4 | 1.4 | 2.9 | 2.0 | 2.0 | 9.2 | 8.7 | 9.4 |
| $K^{*0}$ spectrum | 1.0 | 1.0 | 1.6 | 1.5 | 1.5 | 2.5 | 2.2 | 2.1 | 2.0 | 2.1 | 2.1 |
| $\phi$ spectrum | 1.0 | 1.0 | 6.3 | 5.4 | 5.9 | 9.9 | 6.7 | 7.2 | 4.9 | 5.2 | 5.5 |
| $\Sigma^\pm$ spectrum | 1.0 | 1.0 | 1.0 | 0.9 | 0.9 | 1.1 | 1.0 | 1.0 | 2.2 | 2.2 | 2.1 |
| $\gamma$ spectrum | 1.0 | 1.0 | 0.6 | 0.6 | 0.6 | 0.8 | 0.6 | 0.6 | 1.8 | 1.6 | 1.7 |
| $K^\pm$ spectrum | 1.0 | 1.0 | 3.1 | 4.9 | 5.0 | 5.6 | 5.6 | 5.8 | 2.9 | 3.3 | 3.2 |
| $\Lambda^0$ spectrum | 1.0 | 1.0 | 4.7 | 2.8 | 2.9 | 9.1 | 7.1 | 6.8 | 17.3 | 15.0 | 16.2 |
| $\pi^0$ spectrum | 1.0 | 1.0 | 0.5 | 0.4 | 0.3 | 1.4 | 0.9 | 0.8 | 1.3 | 1.0 | 0.9 |
| $p$ spectrum | 1.0 | 1.0 | 2.8 | 4.7 | 3.8 | 7.8 | 8.9 | 8.2 | 5.0 | 7.2 | 6.3 |
| $\eta'$ spectrum | 1.0 | 1.0 | 2.3 | 2.3 | 2.3 | 1.9 | 2.0 | 2.1 | 2.3 | 2.3 | 2.4 |
| $\Xi^0(1530)$ spectrum | 1.0 | 1.0 | 3.1 | 4.9 | 5.0 | 5.6 | 5.6 | 5.8 | 2.9 | 3.3 | 3.2 |
| $\pi^\pm$ spectrum | 1.0 | 1.0 | 49.2 | 28.5 | 29.8 | 45.2 | 31.7 | 33.7 | 27.4 | 17.0 | 17.1 |
| $\eta$ spectrum | 1.0 | 1.0 | 2.5 | 2.5 | 2.4 | 2.8 | 2.8 | 2.5 | 3.8 | 3.9 | 3.9 |
| $K^0$ spectrum | 1.0 | 1.0 | 4.4 | 6.8 | 7.6 | 9.2 | 8.0 | 8.5 | 4.4 | 4.9 | 4.9 |

Table A.8: $\chi^2/N_{\mathrm{dof}}$ values for identified particle spectra for the VINCIA and PYTHIA8 $p^2_{\perp\mathrm{evol}}$ showers.

| Observable | Weight | | Herwig++ $\tilde{q}^2$ | | | Herwig++ $p^2_{\perp\mathrm{dip}}$ | | | Herwig++ $q^2_{\mathrm{dip}}$ | | |
|---|---|---|---|---|---|---|---|---|---|---|---|
| | T1 | T2 | Def. | T1 | T2 | Def. | T1 | T2 | Def. | T1 | T2 |
| In-plane $p_\perp$ w.r.t. sphericity axes | 1.0 | 5.0 | 39.5 | 37.9 | 40.2 | 243.0 | 28.1 | 38.6 | 973.9 | 308.2 | 42.6 |
| In-plane $p_\perp$ w.r.t. thrust axes | 1.0 | 5.0 | 6.2 | 3.8 | 3.7 | 33.6 | 2.6 | 4.3 | 159.3 | 41.7 | 6.7 |
| Out-of-plane $p_\perp$ w.r.t. sphericity axes | 1.0 | 5.0 | 34.0 | 31.7 | 25.0 | 174.6 | 14.8 | 20.0 | 278.1 | 28.5 | 24.8 |
| Out-of-plane $p_\perp$ w.r.t. thrust axes | 1.0 | 5.0 | 9.2 | 8.9 | 7.0 | 42.7 | 4.1 | 5.7 | 67.1 | 8.9 | 5.8 |
| Mean out-of-plane $p_\perp$ w.r.t. thrust axis vs. $x_p$ | 1.0 | 5.0 | 21.6 | 25.7 | 29.0 | 147.3 | 66.5 | 62.4 | 494.4 | 168.6 | 41.0 |
| Mean $p_\perp$ in GeV vs. $x_p$ | 1.0 | 5.0 | 59.1 | 54.8 | 44.9 | 146.4 | 38.4 | 35.3 | 257.6 | 31.4 | 21.4 |
| Scaled momentum $x_p = \lvert p\rvert/\lvert p_{\mathrm{beam}}\rvert$ | 1.0 | 5.0 | 41.0 | 18.9 | 20.3 | 27.0 | 31.1 | 28.6 | 43.0 | 22.1 | 14.4 |
| Log of scaled momentum, $\log(1/x_p)$ | 1.0 | 5.0 | 43.7 | 17.8 | 18.8 | 28.9 | 30.8 | 29.0 | 46.0 | 22.4 | 13.2 |
| Energy-energy correlation, EEC | 1.0 | 5.0 | 22.0 | 8.5 | 7.2 | 7.0 | 5.4 | 3.9 | 36.9 | 4.9 | 5.3 |
| Sphericity, $S$ | 1.0 | 5.0 | 46.2 | 38.2 | 33.3 | 40.7 | 22.5 | 14.4 | 111.0 | 13.7 | 11.8 |
| Aplanarity, $A$ | 2.0 | 10.0 | 59.4 | 26.9 | 23.2 | 17.1 | 40.7 | 29.8 | 159.2 | 23.0 | 11.7 |
| Planarity, $P$ | 1.0 | 5.0 | 27.6 | 24.1 | 21.9 | 76.0 | 4.0 | 4.0 | 120.7 | 13.6 | 5.0 |
| $D$ parameter | 1.0 | 5.0 | 109.5 | 46.7 | 39.6 | 23.7 | 39.3 | 25.0 | 174.6 | 9.9 | 9.4 |
| $C$ parameter | 1.0 | 5.0 | 34.5 | 15.9 | 14.2 | 28.5 | 7.6 | 6.1 | 73.2 | 5.7 | 13.4 |
| 1-Thrust | 1.0 | 5.0 | 110.7 | 71.8 | 66.6 | 29.0 | 22.1 | 17.1 | 79.1 | 11.5 | 21.7 |
| Thrust major, $M$ | 1.0 | 5.0 | 71.2 | 132.3 | 127.6 | 130.2 | 131.2 | 94.4 | 239.5 | 76.1 | 43.7 |
| Thrust minor, $m$ | 2.0 | 10.0 | 68.2 | 39.5 | 36.5 | 30.5 | 60.2 | 44.0 | 190.4 | 28.9 | 22.6 |
| Oblatness, $O = M - m$ | 1.0 | 5.0 | 42.3 | 72.3 | 65.5 | 86.8 | 4.1 | 3.7 | 105.7 | 49.7 | 10.5 |
| Mean charged multiplicity | 150.0 | 750.0 | 8.4 | 1.6 | 0.9 | 1.4 | 2.5 | 2.7 | 4.5 | 0.0 | 0.0 |
| Charged multiplicity distribution | 2.0 | 10.0 | 2.1 | 1.0 | 1.1 | 3.1 | 1.6 | 1.7 | 3.0 | 0.5 | 1.0 |

Table A.9: $\chi^2/N_{\mathrm{dof}}$ values for event shapes for the Herwig++ showers.

| | Weight | | VINCIA $p_{\perp A}^2$ | | | VINCIA $m_A^2$ | | | PYTHIA8 $p_{\perp \mathrm{evol}}^2$ | | |
|---|---|---|---|---|---|---|---|---|---|---|---|
| Observable | T1 | T2 | Def. | T1 | T2 | Def. | T1 | T2 | Def. | T1 | T2 |
| In-plane $p_\perp$ w.r.t. sphericity axes | 1.0 | 5.0 | 41.7 | 18.2 | 17.2 | 97.8 | 37.8 | 37.6 | 33.4 | 26.7 | 26.7 |
| In-plane $p_\perp$ w.r.t. thrust axes | 1.0 | 5.0 | 14.7 | 9.4 | 8.9 | 28.8 | 17.6 | 17.9 | 9.8 | 10.5 | 10.7 |
| Out-of-plane $p_\perp$ w.r.t. sphericity axes | 1.0 | 5.0 | 23.5 | 19.0 | 18.9 | 41.6 | 28.2 | 27.8 | 16.9 | 16.9 | 16.3 |
| Out-of-plane $p_\perp$ w.r.t. thrust axes | 1.0 | 5.0 | 8.9 | 6.6 | 6.7 | 14.5 | 10.4 | 10.3 | 5.7 | 6.0 | 5.9 |
| Mean out-of-plane $p_\perp$ w.r.t. thrust axis vs. $x_p$ | 1.0 | 5.0 | 34.7 | 18.0 | 16.7 | 83.2 | 39.7 | 40.4 | 23.0 | 23.9 | 24.7 |
| Mean $p_\perp$ in GeV vs. $x_p$ | 1.0 | 5.0 | 33.8 | 20.0 | 20.0 | 75.5 | 50.6 | 53.1 | 24.5 | 24.6 | 25.2 |
| Scaled momentum $x_p = \lvert p \rvert / \lvert p_{\mathrm{beam}} \rvert$ | 1.0 | 5.0 | 7.6 | 6.2 | 5.5 | 28.7 | 18.0 | 16.7 | 13.8 | 13.6 | 13.3 |
| Log of scaled momentum, $\log(1/x_p)$ | 1.0 | 5.0 | 9.5 | 6.3 | 5.9 | 29.6 | 17.6 | 16.6 | 14.1 | 13.1 | 12.9 |
| Energy-energy correlation, EEC | 1.0 | 5.0 | 1.7 | 0.3 | 0.3 | 6.0 | 3.0 | 3.0 | 1.4 | 1.6 | 1.6 |
| Sphericity, $S$ | 1.0 | 5.0 | 7.2 | 1.0 | 1.1 | 27.7 | 4.4 | 5.0 | 2.1 | 2.2 | 2.3 |
| Aplanarity, $A$ | 2.0 | 10.0 | 6.6 | 8.7 | 8.6 | 17.8 | 6.1 | 6.2 | 6.0 | 5.0 | 4.9 |
| Planarity, $P$ | 1.0 | 5.0 | 8.7 | 2.9 | 3.0 | 27.2 | 11.0 | 11.2 | 7.1 | 6.1 | 6.2 |
| $D$ parameter | 1.0 | 5.0 | 8.1 | 8.3 | 7.6 | 6.9 | 10.8 | 10.5 | 9.2 | 9.0 | 8.7 |
| $C$ parameter | 1.0 | 5.0 | 2.9 | 0.8 | 0.9 | 2.5 | 3.9 | 3.3 | 4.6 | 4.1 | 3.9 |
| 1-Thrust | 1.0 | 5.0 | 5.4 | 2.3 | 2.2 | 4.6 | 6.8 | 5.9 | 4.9 | 4.7 | 4.6 |
| Thrust major, $M$ | 1.0 | 5.0 | 47.3 | 15.3 | 14.2 | 111.5 | 18.8 | 21.5 | 7.1 | 11.3 | 11.6 |
| Thrust minor, $m$ | 2.0 | 10.0 | 10.1 | 11.9 | 11.1 | 17.7 | 13.6 | 12.8 | 12.2 | 10.0 | 9.3 |
| Oblatness, $O = M - m$ | 1.0 | 5.0 | 5.5 | 1.8 | 1.8 | 19.3 | 6.9 | 7.3 | 3.7 | 2.3 | 2.4 |
| Mean charged multiplicity | 150.0 | 750.0 | 5.5 | 0.9 | 1.1 | 6.4 | 1.5 | 1.9 | 2.9 | 0.5 | 0.6 |
| Charged multiplicity distribution | 2.0 | 10.0 | 0.7 | 0.4 | 0.4 | 0.8 | 0.4 | 0.5 | 0.5 | 0.3 | 0.3 |

Table A.10: $\chi^2/N_{\mathrm{dof}}$ values for event shapes for the VINCIA and PYTHIA8 $p_{\perp \mathrm{evol}}^2$ showers.

| Observable | Weight T1 | Weight T2 | Herwig++ $\tilde{q}^2$ Def. | Herwig++ $\tilde{q}^2$ T1 | Herwig++ $\tilde{q}^2$ T2 | Herwig++ $p^2_{\perp\mathrm{dip}}$ Def. | Herwig++ $p^2_{\perp\mathrm{dip}}$ T1 | Herwig++ $p^2_{\perp\mathrm{dip}}$ T2 | Herwig++ $q^2_{\mathrm{dip}}$ Def. | Herwig++ $q^2_{\mathrm{dip}}$ T1 | Herwig++ $q^2_{\mathrm{dip}}$ T2 |
|---|---|---|---|---|---|---|---|---|---|---|---|
| Mean $\rho^0(770)$ multiplicity | 10.0 | 0.0 | 3.7 | 0.1 | 0.0 | 9.3 | 0.3 | 1.0 | 11.9 | 0.5 | 10.1 |
| Mean $\Delta^{++}(1232)$ multiplicity | 10.0 | 0.0 | 1.3 | 0.2 | 0.3 | 50.7 | 11.9 | 31.2 | 41.7 | 3.9 | 2.1 |
| Mean $K^{*+}(892)$ multiplicity | 10.0 | 0.0 | 0.5 | 0.3 | 0.6 | 12.6 | 0.9 | 2.2 | 9.6 | 2.7 | 28.0 |
| Mean $\Sigma^0$ multiplicity | 10.0 | 0.0 | 15.7 | 8.8 | 13.2 | 152.4 | 1.8 | 17.4 | 138.5 | 0.0 | 15.4 |
| Mean $\Lambda_b^0$ multiplicity | 10.0 | 0.0 | 0.4 | 3.8 | 3.8 | 3.8 | 3.8 | 3.8 | 3.8 | 3.8 | 3.8 |
| Mean $K^+$ multiplicity | 10.0 | 0.0 | 1.8 | 0.0 | 0.4 | 107.4 | 22.4 | 27.9 | 84.2 | 38.5 | 384.0 |
| Mean $\Xi^0(1530)$ multiplicity | 10.0 | 0.0 | 4.6 | 2.4 | 16.6 | 7446.6 | 0.4 | 261.3 | 7083.6 | 77.6 | 9.0 |
| Mean $\Lambda(1520)$ multiplicity | 10.0 | 0.0 | 59.8 | 63.7 | 63.9 | 60.9 | 66.3 | 64.9 | 61.3 | 65.5 | 66.5 |
| Mean $D_s^{*+}(2112)$ multiplicity | 10.0 | 0.0 | 0.8 | 0.7 | 0.7 | 0.4 | 0.6 | 0.4 | 0.5 | 0.5 | 0.9 |
| Mean $\Sigma^-(1385)$ multiplicity | 10.0 | 0.0 | 1.2 | 0.0 | 1.5 | 2742.0 | 65.7 | 352.4 | 2564.2 | 0.1 | 206.3 |
| Mean $f_1(1420)$ multiplicity | 10.0 | 0.0 | 14.5 | 15.0 | 14.5 | 8.0 | 16.5 | 14.8 | 8.2 | 17.1 | 13.4 |
| Mean $\phi(1020)$ multiplicity | 10.0 | 0.0 | 1.1 | 0.0 | 0.1 | 291.8 | 50.1 | 86.9 | 244.5 | 66.1 | 430.9 |
| Mean $K_2^{*0}$ multiplicity | 10.0 | 0.0 | 0.3 | 0.0 | 0.3 | 3.3 | 1.5 | 0.3 | 2.9 | 1.9 | 0.1 |
| Mean $\Omega^-$ multiplicity | 10.0 | 0.0 | 3.6 | 2.2 | 8.0 | 6744.8 | 0.2 | 50.5 | 6597.7 | 2.2 | 1.2 |
| Mean $\Sigma^{\pm}(1385)$ multiplicity | 10.0 | 0.0 | 9.2 | 1.7 | 7.5 | 4339.4 | 126.3 | 598.2 | 4065.4 | 3.1 | 366.7 |
| Mean $\psi(2S)$ multiplicity | 10.0 | 0.0 | 10.1 | 8.4 | 8.8 | 7.8 | 6.0 | 6.3 | 8.9 | 7.5 | 7.6 |
| Mean $D^{*+}$ multiplicity | 10.0 | 0.0 | 48.9 | 64.1 | 67.6 | 57.8 | 14.0 | 17.0 | 80.0 | 24.7 | 107.7 |
| Mean $B^*$ multiplicity | 10.0 | 0.0 | 14.1 | 75.9 | 78.3 | 26.6 | 16.3 | 20.0 | 29.3 | 19.7 | 27.0 |
| Mean $\pi^0$ multiplicity | 10.0 | 0.0 | 1.5 | 0.1 | 0.1 | 3.8 | 0.0 | 0.2 | 8.6 | 0.3 | 4.4 |
| Mean $\eta$ multiplicity | 10.0 | 0.0 | 0.8 | 2.0 | 2.3 | 11.0 | 1.2 | 2.8 | 13.4 | 1.3 | 5.2 |
| Mean $a_0^+(980)$ multiplicity | 10.0 | 0.0 | 0.2 | 0.5 | 0.6 | 1.6 | 0.7 | 0.8 | 1.8 | 0.7 | 1.6 |
| Mean $D_{s1}^+$ multiplicity | 10.0 | 0.0 | 22.3 | 21.2 | 19.8 | 41.1 | 16.1 | 24.5 | 33.5 | 20.1 | 6.1 |
| Mean $\rho^+(770)$ multiplicity | 10.0 | 0.0 | 1.6 | 0.3 | 0.2 | 0.9 | 0.1 | 0.0 | 1.3 | 0.0 | 1.0 |
| Mean $\Xi^-$ multiplicity | 10.0 | 0.0 | 9.7 | 1.0 | 20.9 | 5680.3 | 36.7 | 106.2 | 5278.2 | 271.3 | 61.5 |
| Mean $\omega(782)$ multiplicity | 10.0 | 0.0 | 4.0 | 0.0 | 0.1 | 20.9 | 1.4 | 2.9 | 25.8 | 1.8 | 21.2 |
| Mean $\Upsilon(1S)$ multiplicity | 10.0 | 0.0 | 4.0 | 4.0 | 4.0 | 4.0 | 4.0 | 4.0 | 4.0 | 4.0 | 4.0 |

Table A.11: $\chi^2/N_{\mathrm{dof}}$ values for particle multiplicities for the Herwig++ showers.

| Observable | Weight T1 | Weight T2 | VINCIA $p_{\perp\mathrm{A}}^2$ Def. | VINCIA $p_{\perp\mathrm{A}}^2$ T1 | VINCIA $p_{\perp\mathrm{A}}^2$ T2 | VINCIA $m_{\mathrm{A}}^2$ Def. | VINCIA $m_{\mathrm{A}}^2$ T1 | VINCIA $m_{\mathrm{A}}^2$ T2 | PYTHIA8 $p_{\perp\mathrm{evol}}^2$ Def. | PYTHIA8 $p_{\perp\mathrm{evol}}^2$ T1 | PYTHIA8 $p_{\perp\mathrm{evol}}^2$ T2 |
|---|---|---|---|---|---|---|---|---|---|---|---|
| Mean $\rho^0(770)$ multiplicity | 10.0 | 0.0 | 0.5 | 0.3 | 0.3 | 0.5 | 0.3 | 0.3 | 1.7 | 2.2 | 2.2 |
| Mean $\Delta^{++}(1232)$ multiplicity | 10.0 | 0.0 | 13.9 | 15.2 | 14.0 | 14.1 | 15.8 | 15.3 | 8.6 | 9.3 | 9.1 |
| Mean $K^{*+}(892)$ multiplicity | 10.0 | 0.0 | 0.4 | 0.8 | 0.8 | 0.4 | 0.5 | 0.6 | 0.1 | 0.1 | 0.1 |
| Mean $\Sigma^0$ multiplicity | 10.0 | 0.0 | 8.1 | 8.7 | 8.4 | 7.9 | 9.3 | 8.8 | 5.1 | 5.7 | 5.5 |
| Mean $\Lambda_b^0$ multiplicity | 10.0 | 0.0 | 0.8 | 0.8 | 0.8 | 0.8 | 0.8 | 0.8 | 0.7 | 0.7 | 0.7 |
| Mean $K^+$ multiplicity | 10.0 | 0.0 | 0.1 | 0.3 | 0.5 | 0.1 | 0.0 | 0.0 | 6.8 | 5.4 | 5.6 |
| Mean $\Xi^0(1530)$ multiplicity | 10.0 | 0.0 | 1.6 | 1.1 | 1.0 | 1.4 | 1.0 | 1.0 | 10.6 | 10.2 | 10.4 |
| Mean $\Lambda(1520)$ multiplicity | 10.0 | 0.0 | 67.6 | 67.6 | 67.6 | 67.6 | 67.6 | 67.6 | 67.6 | 67.6 | 67.6 |
| Mean $D_s^{*+}(2112)$ multiplicity | 10.0 | 0.0 | 0.5 | 0.5 | 0.5 | 0.5 | 0.5 | 0.5 | 0.5 | 0.5 | 0.5 |
| Mean $\Sigma^-(1385)$ multiplicity | 10.0 | 0.0 | 0.1 | 0.3 | 0.2 | 0.1 | 0.5 | 0.3 | 3.7 | 3.5 | 3.5 |
| Mean $f_1(1420)$ multiplicity | 10.0 | 0.0 | 21.8 | 21.8 | 21.8 | 21.8 | 21.8 | 21.8 | 21.8 | 21.8 | 21.8 |
| Mean $\phi(1020)$ multiplicity | 10.0 | 0.0 | 43.9 | 58.5 | 67.4 | 48.7 | 47.2 | 53.5 | 16.9 | 19.1 | 18.7 |
| Mean $K_2^{*0}$ multiplicity | 10.0 | 0.0 | 13.9 | 13.9 | 13.9 | 13.9 | 13.9 | 13.9 | 13.9 | 13.9 | 13.9 |
| Mean $\Omega^-$ multiplicity | 10.0 | 0.0 | 3.5 | 3.7 | 3.7 | 3.5 | 3.6 | 3.5 | 8.1 | 8.3 | 8.3 |
| Mean $\Sigma^{\pm}(1385)$ multiplicity | 10.0 | 0.0 | 5.5 | 7.2 | 6.2 | 5.4 | 7.8 | 7.1 | 0.1 | 0.0 | 0.0 |
| Mean $\psi(2S)$ multiplicity | 10.0 | 0.0 | 7.3 | 6.6 | 6.6 | 6.6 | 6.5 | 6.4 | 6.5 | 6.7 | 7.0 |
| Mean $D^{*+}$ multiplicity | 10.0 | 0.0 | 3.0 | 1.3 | 1.4 | 2.3 | 1.7 | 1.7 | 7.2 | 7.3 | 7.0 |
| Mean $B^*$ multiplicity | 10.0 | 0.0 | 1.0 | 1.1 | 1.1 | 1.1 | 1.1 | 1.1 | 1.1 | 1.1 | 1.1 |
| Mean $\pi^0$ multiplicity | 10.0 | 0.0 | 0.3 | 1.0 | 0.9 | 0.2 | 0.8 | 0.7 | 0.3 | 0.8 | 0.7 |
| Mean $\eta$ multiplicity | 10.0 | 0.0 | 2.9 | 3.6 | 3.5 | 2.7 | 3.5 | 3.4 | 0.6 | 0.4 | 0.5 |
| Mean $a_0^+(980)$ multiplicity | 10.0 | 0.0 | 6.0 | 6.0 | 6.0 | 6.0 | 6.0 | 6.0 | 6.0 | 6.0 | 6.0 |
| Mean $D_{s1}^+$ multiplicity | 10.0 | 0.0 | 1.4 | 1.4 | 1.4 | 1.5 | 1.4 | 1.4 | 1.5 | 1.3 | 1.2 |
| Mean $\rho^+(770)$ multiplicity | 10.0 | 0.0 | 0.1 | 0.1 | 0.1 | 0.2 | 0.1 | 0.1 | 0.3 | 0.3 | 0.3 |
| Mean $\Xi^-$ multiplicity | 10.0 | 0.0 | 6.5 | 9.4 | 9.2 | 6.3 | 9.2 | 9.2 | 2.1 | 1.6 | 2.0 |
| Mean $\omega(782)$ multiplicity | 10.0 | 0.0 | 2.3 | 2.9 | 2.7 | 2.0 | 2.9 | 2.7 | 21.5 | 24.0 | 23.8 |
| Mean $\Upsilon(1S)$ multiplicity | 10.0 | 0.0 | 3.7 | 3.6 | 3.6 | 3.4 | 3.3 | 3.4 | 3.6 | 3.6 | 3.7 |

Table A.12: $\chi^2/N_{\mathrm{dof}}$ values for particle multiplicities for the VINCIA and PYTHIA8 $p_{\perp\mathrm{evol}}^2$ showers.

| Observable | Weight | | Herwig++ $\tilde{q}^2$ | | | Herwig++ $p^2_{\perp \rm dip}$ | | | Herwig++ $q^2_{\rm dip}$ | | |
|---|---|---|---|---|---|---|---|---|---|---|---|
| | T1 | T2 | Def. | T1 | T2 | Def. | T1 | T2 | Def. | T1 | T2 |
| Mean $\chi_{c1}(3510)$ multiplicity | 10.0 | 0.0 | 11.3 | 10.8 | 10.9 | 10.6 | 10.6 | 10.4 | 10.8 | 10.7 | 10.5 |
| Mean $D^+$ multiplicity | 10.0 | 0.0 | 12.4 | 16.0 | 16.2 | 17.1 | 63.5 | 47.2 | 12.0 | 35.2 | 32.1 |
| Mean $\Sigma^+$ multiplicity | 10.0 | 0.0 | 0.1 | 0.5 | 0.0 | 86.2 | 3.6 | 0.5 | 76.6 | 9.1 | 1.6 |
| Mean $f_1(1285)$ multiplicity | 10.0 | 0.0 | 2.2 | 2.9 | 2.9 | 4.8 | 4.6 | 4.2 | 5.0 | 4.7 | 5.9 |
| Mean $f_2(1270)$ multiplicity | 10.0 | 0.0 | 14.8 | 6.1 | 8.6 | 1.2 | 3.2 | 0.6 | 0.5 | 4.9 | 9.6 |
| Mean $J/\psi(1S)$ multiplicity | 10.0 | 0.0 | 33.7 | 25.1 | 24.1 | 20.0 | 11.9 | 13.4 | 24.0 | 18.2 | 2.7 |
| Mean $B_u^+$ multiplicity | 10.0 | 0.0 | 1.9 | 0.0 | 0.0 | 8.9 | 63.1 | 41.9 | 2.3 | 25.3 | 7.5 |
| Mean $B^{*}*$ multiplicity | 10.0 | 0.0 | 11.8 | 23.0 | 23.3 | 23.1 | 22.6 | 22.7 | 23.1 | 22.5 | 23.1 |
| Mean $\Lambda_c^+$ multiplicity | 10.0 | 0.0 | 0.1 | 6.1 | 6.6 | 0.8 | 15.2 | 9.9 | 1.2 | 11.5 | 15.9 |
| Mean $D^0$ multiplicity | 10.0 | 0.0 | 0.3 | 0.3 | 0.3 | 0.1 | 8.0 | 4.4 | 1.1 | 1.8 | 0.0 |
| Mean $f_2'(1525)$ multiplicity | 10.0 | 0.0 | 0.0 | 0.0 | 0.0 | 6.6 | 0.5 | 0.0 | 6.0 | 0.9 | 0.0 |
| Mean $\Sigma^\pm$ multiplicity | 10.0 | 0.0 | 14.6 | 2.9 | 9.6 | 624.9 | 0.9 | 27.1 | 564.0 | 14.2 | 41.0 |
| Mean $D_{s2}^+$ multiplicity | 10.0 | 0.0 | 3.1 | 2.9 | 3.1 | 2.1 | 4.5 | 3.5 | 2.2 | 3.8 | 4.9 |
| Mean $K^{*0}(892)$ multiplicity | 10.0 | 0.0 | 0.2 | 0.1 | 0.6 | 54.6 | 1.3 | 6.1 | 39.4 | 7.5 | 133.7 |
| Mean $\Sigma^-$ multiplicity | 10.0 | 0.0 | 3.0 | 0.8 | 2.4 | 118.5 | 0.0 | 6.1 | 107.1 | 2.2 | 8.8 |
| Mean $\pi^+$ multiplicity | 10.0 | 0.0 | 11.5 | 1.0 | 0.9 | 31.2 | 0.1 | 2.5 | 73.2 | 5.1 | 34.8 |
| Mean $f_0(980)$ multiplicity | 10.0 | 0.0 | 32.7 | 42.6 | 44.1 | 55.9 | 38.5 | 41.6 | 59.3 | 37.7 | 48.9 |
| Mean $\Sigma^+(1385)$ multiplicity | 10.0 | 0.0 | 10.9 | 1.8 | 6.8 | 3904.3 | 113.6 | 540.4 | 3659.8 | 3.5 | 336.2 |
| Mean $D_s^+$ multiplicity | 10.0 | 0.0 | 0.0 | 1.4 | 1.4 | 3.9 | 10.6 | 8.6 | 2.7 | 5.2 | 8.6 |
| Mean $p$ multiplicity | 10.0 | 0.0 | 28.6 | 0.1 | 0.9 | 640.1 | 27.9 | 166.6 | 525.8 | 11.2 | 10.9 |
| Mean $B_s^0$ multiplicity | 10.0 | 0.0 | 0.0 | 3.7 | 3.7 | 3.7 | 2.5 | 3.5 | 2.9 | 1.5 | 4.0 |
| Mean $K^0$ multiplicity | 10.0 | 0.0 | 2.9 | 24.1 | 37.4 | 694.9 | 223.7 | 254.1 | 564.3 | 331.9 | 2291.9 |
| Mean $B^+, B/d^0$ multiplicity | 10.0 | 0.0 | 0.0 | 0.3 | 0.3 | 1.3 | 5.3 | 3.8 | 0.7 | 2.6 | 1.2 |
| Mean $\Lambda$ multiplicity | 10.0 | 0.0 | 25.0 | 6.9 | 4.1 | 12938.6 | 5.9 | 766.7 | 11816.3 | 98.8 | 475.5 |
| Mean $\eta'(958)$ multiplicity | 10.0 | 0.0 | 9.9 | 10.2 | 10.3 | 7.1 | 5.9 | 6.1 | 8.2 | 6.5 | 4.8 |

Table A.13: $\chi^2/N_{\rm dof}$ values for particle multiplicities for the Herwig++ showers.

| Observable | Weight T1 | Weight T2 | VINCIA $p^2_{\perp\mathrm{A}}$ Def. | VINCIA $p^2_{\perp\mathrm{A}}$ T1 | VINCIA $p^2_{\perp\mathrm{A}}$ T2 | VINCIA $m^2_{\mathrm{A}}$ Def. | VINCIA $m^2_{\mathrm{A}}$ T1 | VINCIA $m^2_{\mathrm{A}}$ T2 | PYTHIA8 $p^2_{\perp\mathrm{evol}}$ Def. | PYTHIA8 $p^2_{\perp\mathrm{evol}}$ T1 | PYTHIA8 $p^2_{\perp\mathrm{evol}}$ T2 |
|---|---|---|---|---|---|---|---|---|---|---|---|
| Mean $\chi_{c1}(3510)$ multiplicity | 10.0 | 0.0 | 10.9 | 10.8 | 10.9 | 10.9 | 10.9 | 10.9 | 10.9 | 10.9 | 10.9 |
| Mean $D^+$ multiplicity | 10.0 | 0.0 | 19.6 | 22.6 | 22.6 | 20.7 | 21.6 | 21.5 | 18.2 | 18.1 | 18.0 |
| Mean $\Sigma^+$ multiplicity | 10.0 | 0.0 | 0.0 | 0.0 | 0.0 | 0.0 | 0.0 | 0.0 | 0.5 | 0.4 | 0.4 |
| Mean $f_1(1285)$ multiplicity | 10.0 | 0.0 | 10.5 | 10.5 | 10.5 | 10.5 | 10.5 | 10.5 | 10.5 | 10.5 | 10.5 |
| Mean $f_2(1270)$ multiplicity | 10.0 | 0.0 | 68.6 | 68.6 | 68.6 | 68.6 | 68.6 | 68.6 | 68.6 | 68.6 | 68.6 |
| Mean $J/\psi(1S)$ multiplicity | 10.0 | 0.0 | 0.0 | 0.1 | 0.0 | 0.0 | 0.0 | 0.0 | 0.5 | 0.8 | 0.6 |
| Mean $B_u^+$ multiplicity | 10.0 | 0.0 | 3.4 | 3.5 | 3.3 | 3.5 | 3.5 | 3.6 | 5.3 | 5.4 | 5.2 |
| Mean $B^*\ast$ multiplicity | 10.0 | 0.0 | 24.2 | 24.2 | 24.2 | 24.2 | 24.2 | 24.2 | 24.2 | 24.2 | 24.2 |
| Mean $\Lambda_c^+$ multiplicity | 10.0 | 0.0 | 5.7 | 5.5 | 5.6 | 5.7 | 5.5 | 5.6 | 4.8 | 4.8 | 4.8 |
| Mean $D^0$ multiplicity | 10.0 | 0.0 | 1.3 | 2.2 | 2.2 | 1.7 | 1.9 | 1.8 | 4.9 | 5.0 | 4.9 |
| Mean $f_2'(1525)$ multiplicity | 10.0 | 0.0 | 4.0 | 4.0 | 4.0 | 4.0 | 4.0 | 4.0 | 4.0 | 4.0 | 4.0 |
| Mean $\Sigma^\pm$ multiplicity | 10.0 | 0.0 | 10.2 | 12.5 | 11.1 | 10.3 | 13.8 | 12.6 | 2.6 | 3.4 | 3.1 |
| Mean $D_{s2}^+$ multiplicity | 10.0 | 0.0 | 5.9 | 5.9 | 5.9 | 5.9 | 5.9 | 6.0 | 6.1 | 6.0 | 6.0 |
| Mean $K^{*0}(892)$ multiplicity | 10.0 | 0.0 | 1.6 | 3.6 | 4.4 | 1.6 | 2.4 | 2.7 | 0.1 | 0.4 | 0.4 |
| Mean $\Sigma^-$ multiplicity | 10.0 | 0.0 | 2.6 | 3.0 | 2.7 | 2.5 | 3.4 | 3.1 | 0.7 | 0.9 | 0.8 |
| Mean $\pi^+$ multiplicity | 10.0 | 0.0 | 6.0 | 1.4 | 1.8 | 7.2 | 1.9 | 2.4 | 0.9 | 0.0 | 0.0 |
| Mean $f_0(980)$ multiplicity | 10.0 | 0.0 | 145.2 | 145.2 | 145.2 | 145.2 | 145.2 | 145.2 | 145.3 | 145.4 | 145.4 |
| Mean $\Sigma^+(1385)$ multiplicity | 10.0 | 0.0 | 8.6 | 10.5 | 9.4 | 8.3 | 10.8 | 10.2 | 0.3 | 0.4 | 0.4 |
| Mean $D_s^+$ multiplicity | 10.0 | 0.0 | 0.1 | 0.0 | 0.0 | 0.0 | 0.1 | 0.0 | 0.2 | 0.2 | 0.3 |
| Mean $p$ multiplicity | 10.0 | 0.0 | 2.1 | 3.8 | 2.7 | 2.0 | 4.6 | 3.7 | 1.3 | 2.4 | 2.0 |
| Mean $B_s^0$ multiplicity | 10.0 | 0.0 | 1.5 | 1.4 | 1.3 | 1.4 | 1.4 | 1.4 | 2.2 | 2.2 | 2.2 |
| Mean $K^0$ multiplicity | 10.0 | 0.0 | 21.5 | 39.8 | 46.4 | 22.1 | 27.5 | 31.8 | 0.9 | 0.1 | 0.1 |
| Mean $B^+, B/d^0$ multiplicity | 10.0 | 0.0 | 0.9 | 0.9 | 0.8 | 0.9 | 0.9 | 0.9 | 1.1 | 1.1 | 1.1 |
| Mean $\Lambda$ multiplicity | 10.0 | 0.0 | 19.4 | 12.5 | 13.9 | 20.6 | 11.9 | 13.4 | 67.8 | 59.2 | 62.4 |
| Mean $\eta'(958)$ multiplicity | 10.0 | 0.0 | 0.0 | 0.0 | 0.0 | 0.0 | 0.0 | 0.0 | 0.2 | 0.1 | 0.1 |

Table A.14: $\chi^2/N_{\mathrm{dof}}$ values for particle multiplicities for the VINCIA and PYTHIA8 $p^2_{\perp\mathrm{evol}}$ showers.

| Observable | Weight T1 | Weight T2 | Herwig++ $\tilde{q}^2$ Def. | Herwig++ $\tilde{q}^2$ T1 | Herwig++ $\tilde{q}^2$ T2 | Herwig++ $p^2_{\perp\mathrm{dip}}$ Def. | Herwig++ $p^2_{\perp\mathrm{dip}}$ T1 | Herwig++ $p^2_{\perp\mathrm{dip}}$ T2 | Herwig++ $q^2_{\mathrm{dip}}$ Def. | Herwig++ $q^2_{\mathrm{dip}}$ T1 | Herwig++ $q^2_{\mathrm{dip}}$ T2 |
|---|---|---|---|---|---|---|---|---|---|---|---|
| Differential 2-jet rate | 2.0 | 10.0 | 6.2 | 8.2 | 8.9 | 4.2 | 2.5 | 1.8 | 6.1 | 2.0 | 1.4 |
| Differential 3-jet rate | 2.0 | 10.0 | 4.9 | 17.0 | 20.8 | 10.6 | 5.1 | 3.6 | 15.3 | 0.4 | 2.2 |
| Differential 4-jet rate | 2.0 | 10.0 | 10.5 | 24.0 | 27.7 | 15.5 | 8.1 | 6.1 | 20.9 | 1.2 | 5.5 |
| Differential 5-jet rate | 2.0 | 10.0 | 2.4 | 27.5 | 33.4 | 28.3 | 11.2 | 9.2 | 35.6 | 1.7 | 11.0 |

Table A.15: $\chi^2$ values for jet rates for the Herwig++ showers.

| Observable | Weight T1 | Weight T2 | Vincia $p^2_{\perp\mathrm{A}}$ Def. | Vincia $p^2_{\perp\mathrm{A}}$ T1 | Vincia $p^2_{\perp\mathrm{A}}$ T2 | Vincia $m^2_{\mathrm{A}}$ Def. | Vincia $m^2_{\mathrm{A}}$ T1 | Vincia $m^2_{\mathrm{A}}$ T2 | Pythia8 $p^2_{\perp\mathrm{evol}}$ Def. | Pythia8 $p^2_{\perp\mathrm{evol}}$ T1 | Pythia8 $p^2_{\perp\mathrm{evol}}$ T2 |
|---|---|---|---|---|---|---|---|---|---|---|---|
| Differential 2-jet rate | 2.0 | 10.0 | 0.2 | 0.4 | 0.4 | 0.5 | 0.1 | 0.2 | 0.5 | 0.5 | 0.5 |
| Differential 3-jet rate | 2.0 | 10.0 | 0.3 | 0.7 | 0.7 | 0.3 | 0.5 | 0.4 | 0.6 | 0.5 | 0.6 |
| Differential 4-jet rate | 2.0 | 10.0 | 0.6 | 0.9 | 0.9 | 0.6 | 0.8 | 0.8 | 0.8 | 0.7 | 0.7 |
| Differential 5-jet rate | 2.0 | 10.0 | 0.4 | 0.6 | 0.6 | 0.7 | 0.7 | 0.7 | 0.8 | 0.6 | 0.7 |

Table A.16: $\chi^2$ values for jet rates for the Vincia and Pythia8 $p^2_{\perp\mathrm{evol}}$ showers.

| Observable | Weight T1 | Weight T2 | Herwig++ $\tilde{q}^2$ Def. | Herwig++ $\tilde{q}^2$ T1 | Herwig++ $\tilde{q}^2$ T2 | Herwig++ $p^2_{\perp\mathrm{dip}}$ Def. | Herwig++ $p^2_{\perp\mathrm{dip}}$ T1 | Herwig++ $p^2_{\perp\mathrm{dip}}$ T2 | Herwig++ $q^2_{\mathrm{dip}}$ Def. | Herwig++ $q^2_{\mathrm{dip}}$ T1 | Herwig++ $q^2_{\mathrm{dip}}$ T2 |
|---|---|---|---|---|---|---|---|---|---|---|---|
| $b$ quark fragmentation function $f(x_B^{\mathrm{weak}})$ | 7.0 | 35.0 | 35.3 | 28.4 | 33.2 | 228.1 | 449.1 | 387.0 | 137.3 | 311.9 | 232.3 |
| Mean of $b$ quark fragmentation function $f(x_B^{\mathrm{weak}})$ | 3.0 | 15.0 | 12.9 | 12.5 | 14.6 | 42.9 | 53.9 | 50.3 | 32.1 | 40.6 | 41.5 |

Table A.17: $\chi^2$ values for observables for $b$ quarks for the Herwig++ showers.

| Observable | Weight T1 | Weight T2 | Vincia $p^2_{\perp\mathrm{A}}$ Def. | Vincia $p^2_{\perp\mathrm{A}}$ T1 | Vincia $p^2_{\perp\mathrm{A}}$ T2 | Vincia $m^2_{\mathrm{A}}$ Def. | Vincia $m^2_{\mathrm{A}}$ T1 | Vincia $m^2_{\mathrm{A}}$ T2 | Pythia8 $p^2_{\perp\mathrm{evol}}$ Def. | Pythia8 $p^2_{\perp\mathrm{evol}}$ T1 | Pythia8 $p^2_{\perp\mathrm{evol}}$ T2 |
|---|---|---|---|---|---|---|---|---|---|---|---|
| $b$ quark fragmentation function $f(x_B^{\mathrm{weak}})$ | 7.0 | 35.0 | 2.7 | 0.0 | 0.0 | 3.6 | 0.6 | 0.3 | 0.6 | 1.1 | 1.5 |
| Mean of $b$ quark fragmentation function $f(x_B^{\mathrm{weak}})$ | 3.0 | 15.0 | 5.2 | 2.6 | 2.0 | 4.8 | 2.5 | 1.7 | 3.5 | 4.3 | 4.4 |

Table A.18: $\chi^2$ values for observables for $b$ quarks for the Vincia and Pythia8 $p^2_{\perp\mathrm{evol}}$ showers.

# Parameters of Additional Tunes

The following Tabs. A.19-A.21 list the parameter values that result from tuning HERWIG++ and VINCIA with different configurations.

| | Default | Range | VINCIA $p^2_{\perp\mathrm{A}}$ Tune 1 | VINCIA $p^2_{\perp\mathrm{A}}$ Tune 2 | VINCIA $m^2_{\mathrm{A}}$ Tune 1 | VINCIA $m^2_{\mathrm{A}}$ Tune 2 |
|---|---|---|---|---|---|---|
| $\alpha_S$ | 0.129 | $0.120 - 0.132$ | 0.129 | 0.129 | 0.132 | 0.132 |
| $p^{2\ \mathrm{min}}_{\perp\mathrm{A}}$ | 0.60 | $0.46 - 1.00$ | 0.50 | 0.46 | 0.76 | 0.67 |
| $a_{\mathrm{L}}$ | 0.38 | $0.20 - 0.70$ | 0.38 | 0.25 | 0.39 | 0.37 |
| $b_{\mathrm{L}}$ | 0.90 | $0.50 - 1.50$ | 0.86 | 0.72 | 0.71 | 0.71 |
| $a_{\mathrm{ED}}$ | 1.00 | $0.50 - 0.10$ | 0.60 | 0.87 | 0.55 | 0.51 |
| $\sigma$ | 0.275 | $0.200 - 0.400$ | 0.264 | 0.263 | 0.291 | 0.292 |

Table A.19: The tables list the parameters with their default value and the scanned range for tuning VINCIA with smooth ordering. The last columns contain the values of the best tunes for the first tune to all observables and for the second tune with emphasis on the event shapes and jet rates.

| | Default | Range | VINCIA $p^2_{\perp\mathrm{A}}$ Tune 1 | VINCIA $p^2_{\perp\mathrm{A}}$ Tune 2 |
|---|---|---|---|---|
| $\alpha_S$ | 0.129 | $0.120 - 0.132$ | 0.131 | 0.130 |
| $p^{2\ \mathrm{min}}_{\perp\mathrm{A}}$ | 0.60 | $0.46 - 1.00$ | 0.60 | 0.46 |
| $a_{\mathrm{L}}$ | 0.38 | $0.20 - 0.70$ | 0.44 | 0.24 |
| $b_{\mathrm{L}}$ | 0.90 | $0.50 - 1.50$ | 0.97 | 0.74 |
| $a_{\mathrm{ED}}$ | 1.00 | $0.50 - 0.10$ | 0.55 | 0.64 |
| $\sigma$ | 0.275 | $0.200 - 0.400$ | 0.260 | 0.260 |

Table A.20: The tables list the parameters with their default value and the scanned range for tuning VINCIA with matching and smooth ordering. The last columns contain the values of the best tunes for the first tune to all observables and for the second tune with emphasis on the event shapes and jet rates.

| | Default | Range | HERWIG++ $p_{\perp\mathrm{dip}}^2$ Tune 1 | Tune 2 |
|---|---|---|---|---|
| $\alpha_{M_Z}$ | 0.118 | 0.100 – 0.138 | 0.127 | 0.127 |
| $\mu_{\mathrm{IR},FF}$ | 1.25 GeV | (0.50 – 2.00) GeV | 0.81 GeV | 1.01 GeV |
| $\mu_{\mathrm{soft},FF}$ | 0.00 GeV | fixed | 0.00 GeV | 0.00 GeV |
| $m_{g,c}$ | 1.01 GeV | (0.67 – 3.00) GeV | 0.70 GeV | 0.79 GeV |
| $\mathrm{Cl}_{\mathrm{max}}$ | 3.66 GeV | (2.00 – 4.50) GeV | 3.11 GeV | 3.27 GeV |
| $\mathrm{Cl}_{\mathrm{pow}}$ | 5.68 | 2.00 – 10.00 | 7.90 | 10.00 |
| $P_{\mathrm{split}}$ | 0.77 | 0.00 – 1.40 | 0.70 | 0.72 |

Table A.21: The tables list the parameters with their default value and the scanned range for tuning the HERWIG++ dipole shower with matching. The last columns contain the values of the best tunes for the first tune to all observables and for the second tune with emphasis on the event shapes and jet rates.

# B. LEP Data

## Difference in Opening Angles: $\alpha^*$

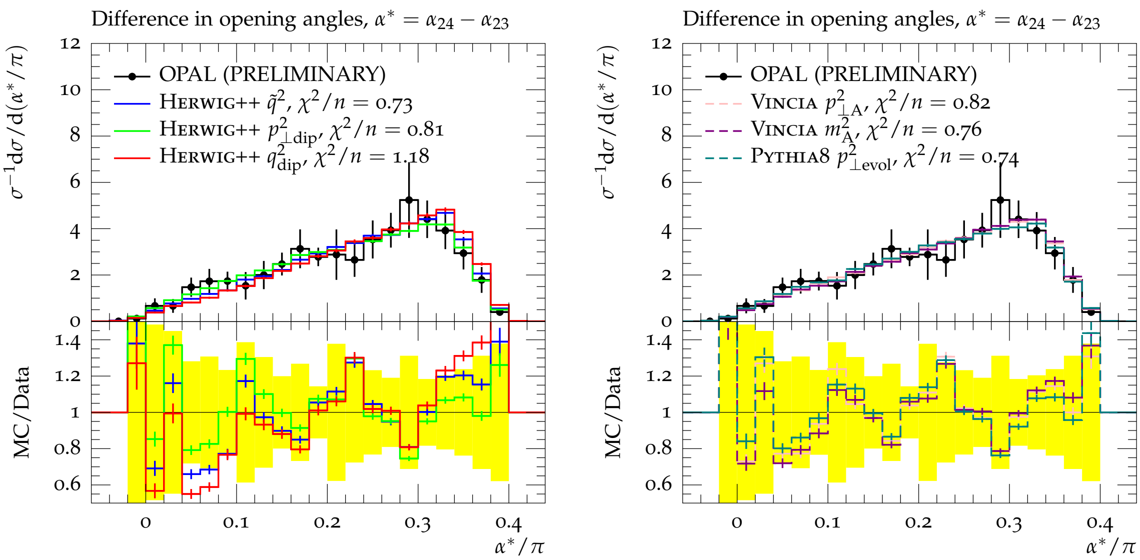


Figure B.1: The plots show the normalized distribution of the difference in opening angles. The plots on the left hand side show the results for the HERWIG++ shower models, the angular-ordered shower (blue) and the dipole shower with ordering in $p^2_{\perp\mathrm{dip}}$ (green) and $q^2_{\mathrm{dip}}$ (red). The predictions of PYTHIA8 (teal) and VINCIA with ordering in $p^2_{\perp\mathrm{A}}$ (pink) and antenna mass (violet) are shown on the right. The ratio plot shows the deviation of the Monte Carlos with respect to the data. The description of line style and colour holds for all plots in this section.

## Double Ratios: $C(2, 2.0)$, $C_s(1, 0.2)/C_h(1, 0.2)$ and $C_s(1, 2.0)/C_h(1, 2.0)$

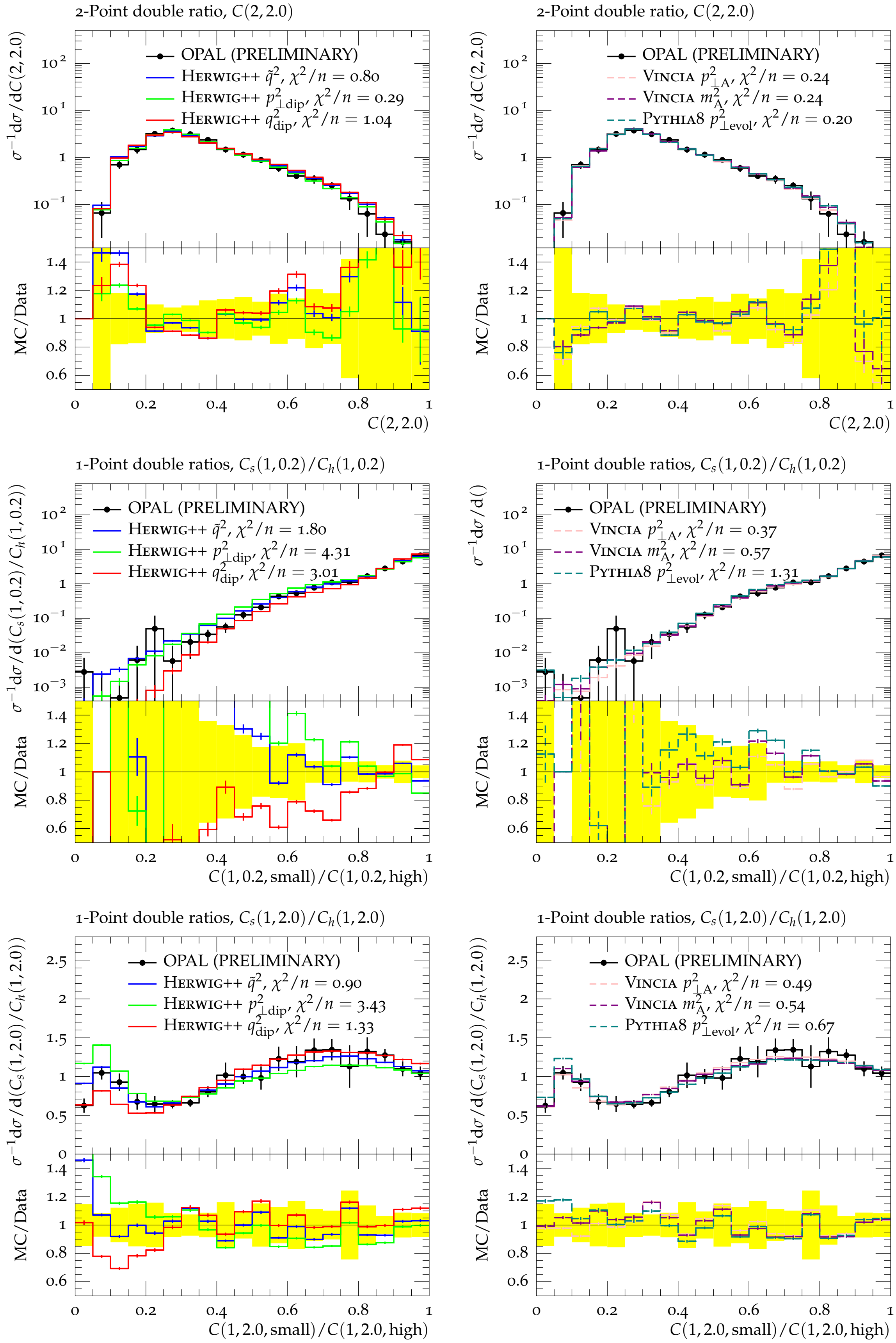


Figure B.2: The plots show the normalized distribution of the 2-point double ratio $C(2, 2.0)$ and the 1-point double ratios $C_s(1, 0.2)/C_h(1, 0.2)$ and $C_s(1, 2.0)/C_h(1, 2.0)$.

# Bibliography


[1] M. Bähr, S. Gieseke, M. Gigg, D. Grellscheid, K. Hamilton, et al., *Herwig++ Physics and Manual*, *Eur.Phys.J.* **C58** (2008) 639–707, [`arXiv:0803.0883`].

[2] T. Sjöstrand, S. Mrenna, and P. Skands, *A Brief Introduction to PYTHIA 8.1*, *Comput.Phys.Commun.* **178** (2008) 852–867, [`arXiv:0710.3820`].

[3] M. E. Peskin and D. V. Schroeder, *An Introduction to Quantum Field Theory (Frontiers in Physics).* Perseus Books, 1995.

[4] L. H. Ryder, *Quantum Field Theory.* Cambridge University Press, 1996.

[5] R. K. Ellis, W. J. Stirling, and B. R. Webber, *QCD and collider physics*, vol. 8. Cambridge University Press, 2003.

[6] D. J. Gross and F. Wilczek, *Ultraviolet Behavior of Nonabelian Gauge Theories*, *Phys.Rev.Lett.* **30** (1973) 1343–1346.

[7] H. D. Politzer, *Reliable Perturbative Results for Strong Interactions?*, *Phys.Rev.Lett.* **30** (1973) 1346–1349.

[8] "The opal detector." http://opal.web.cern.ch/Opal/tour/detector.html, May, 2001. Accessed: 2013-08-14.

[9] P. Z. Skands, *Introduction to QCD*, `arXiv:1207.2389`.

[10] A. Buckley, J. Butterworth, S. Gieseke, D. Grellscheid, S. Höche, et al., *General-purpose event generators for LHC physics*, *Phys.Rept.* **504** (2011) 145–233, [`arXiv:1101.2599`].

[11] G. Dissertori, I. Knowles, and M. Schmelling, *Quantum Chromodynamics: High energy experiments and theory International Series of Monographs on Physics No. 115.* Oxford University Press, 2003.

[12] **NLO Multileg Working Group**, Z. Bern et al., *The NLO multileg working group: Summary report*, `arXiv:0803.0494`.

[13] R. D. Field and R. P. Feynman, *Quark elastic scattering as a source of high-transverse-momentum mesons*, *Physical Review D* **15** (1977), no. 9 2590.

[14] R. D. Field and R. P. Feynman, *A parametrization of the properties of quark jets*, *Nuclear Physics B* **136** (1978), no. 1 1–76.

[15] B. Andersson, G. Gustafson, G. Ingelman, and T. Sjöstrand, *Parton Fragmentation and String Dynamics*, *Phys.Rept.* **97** (1983) 31–145.

[16] T. Sjöstrand, *Jet Fragmentation of Nearby Partons*, *Nucl.Phys.* **B248** (1984) 469.

[17] B. Webber, *A QCD Model for Jet Fragmentation Including Soft Gluon Interference*, *Nucl.Phys.* **B238** (1984) 492.

[18] E. Boos, M. Dobbs, W. Giele, I. Hinchliffe, J. Huston, et al., *Generic user process interface for event generators*, `hep-ph/0109068`.

[19] J. Alwall, A. Ballestrero, P. Bartalini, S. Belov, E. Boos, et al., *A Standard format for Les Houches event files*, *Comput.Phys.Commun.* **176** (2007) 300–304, [`hep-ph/0609017`].

[20] T. Gleisberg, S. Höche, F. Krauss, M. Schönherr, S. Schumann, et al., *Event generation with SHERPA 1.1*, *JHEP* **0902** (2009) 007, [`arXiv:0811.4622`].

[21] F. Maltoni and T. Stelzer, *MadEvent: Automatic event generation with MadGraph*, *JHEP* **0302** (2003) 027, [`hep-ph/0208156`].

[22] K. Arnold, M. Bähr, G. Bozzi, F. Campanario, C. Englert, et al., *VBFNLO: A Parton level Monte Carlo for processes with electroweak bosons*, *Comput.Phys.Commun.* **180** (2009) 1661–1670, [`arXiv:0811.4559`].

[23] W. T. Giele, D. A. Kosower, and P. Z. Skands, *A Simple shower and matching algorithm*, *Phys.Rev.* **D78** (2008) 014026, [`arXiv:0707.3652`].

[24] S. Gieseke, P. Stephens, and B. Webber, *New formalism for QCD parton showers*, *JHEP* **0312** (2003) 045, [`hep-ph/0310083`].

[25] S. Plätzer and S. Gieseke, *Coherent Parton Showers with Local Recoils*, *JHEP* **1101** (2011) 024, [`arXiv:0909.5593`].

[26] S. Plätzer and S. Gieseke, *Dipole Showers and Automated NLO Matching in Herwig++*, *Eur.Phys.J.* **C72** (2012) 2187, [`arXiv:1109.6256`].

[27] G. Marchesini, B. Webber, G. Abbiendi, I. Knowles, M. Seymour, et al., *Herwig version 5.9*, `hep-ph/9607393`.

[28] S. Catani and M. H. Seymour, *A General algorithm for calculating jet cross-sections in NLO QCD*, *Nucl.Phys.* **B485** (1997) 291–419, [`hep-ph/9605323`].

[29] T. Sjöstrand, S. Mrenna, and P. Z. Skands, *PYTHIA 6.4 Physics and Manual*, *JHEP* **0605** (2006) 026, [`hep-ph/0603175`].

[30] T. Sjostrand and P. Z. Skands, *Transverse-momentum-ordered showers and interleaved multiple interactions*, *Eur.Phys.J.* **C39** (2005) 129–154, [`hep-ph/0408302`].

[31] M. H. Seymour, *A Simple prescription for first order corrections to quark scattering and annihilation processes*, *Nucl.Phys.* **B436** (1995) 443–460, [`hep-ph/9410244`].

[32] M. H. Seymour, *Matrix element corrections to parton shower algorithms*, *Comput.Phys.Commun.* **90** (1995) 95–101, [`hep-ph/9410414`].

[33] S. Frixione and B. R. Webber, *Matching NLO QCD computations and parton showersimulations*, *JHEP* **0206** (2002) 029, [hep-ph/0204244].

[34] S. Frixione, F. Stoeckli, P. Torrielli, B. R. Webber, and C. D. White, *The MCaNLO 4.0 Event Generator*, arXiv:1010.0819.

[35] S. Frixione, F. Stoeckli, P. Torrielli, and B. R. Webber, *NLO QCD corrections in Herwig++ with MC@NLO*, *JHEP* **1101** (2011) 053, [arXiv:1010.0568].

[36] A. Buckley, J. Butterworth, L. Lönnblad, H. Hoeth, J. Monk, et al., *Rivet user manual*, arXiv:1003.0694.

[37] M. Dobbs and J. B. Hansen, *The HepMC C++ Monte Carlo event record for High Energy Physics*, *Comput.Phys.Commun.* **134** (2001) 41–46.

[38] A. Buckley, H. Hoeth, H. Lacker, H. Schulz, and J. E. von Seggern, *Systematic event generator tuning for the LHC*, *Eur.Phys.J.* **C65** (2010) 331–357, [arXiv:0907.2973].

[39] H. Schulz, *Systematic event generator tuning with professor*, diplomarbeit, Humboldt-Univeristät zu Berlin, 2009.

[40] M. Cacciari, G. P. Salam, and G. Soyez, *FastJet User Manual*, *Eur.Phys.J.* **C72** (2012) 1896, [arXiv:1111.6097].

[41] S. Catani, Y. L. Dokshitzer, M. Olsson, G. Turnock, and B. Webber, *New clustering algorithm for multi - jet cross-sections in e+ e- annihilation*, *Phys.Lett.* **B269** (1991) 432–438.

[42] G. P. Salam, *Towards Jetography*, *Eur.Phys.J.* **C67** (2010) 637–686, [arXiv:0906.1833].

[43] **SM AND NLO MULTILEG and SM MC Working Groups**, J. Alcaraz Maestre et al., *The SM and NLO Multileg and SM MC Working Groups: Summary Report*, arXiv:1203.6803.

[44] **ALEPH Collaboration**, R. Barate et al., *Studies of quantum chromodynamics with the ALEPH detector*, *Phys.Rept.* **294** (1998) 1–165.

[45] **ALEPH Collaboration**, A. Heister et al., *Study of the fragmentation of b quarks into B mesons at the Z peak*, *Phys.Lett.* **B512** (2001) 30–48, [hep-ex/0106051].

[46] **DELPHI Collaboration**, P. Abreu et al., *Tuning and test of fragmentation models based on identified particles and precision event shape data*, *Z.Phys.* **C73** (1996) 11–60.

[47] **JADE Collaboration, OPAL Collaboration**, P. Pfeifenschneider et al., *QCD analyses and determinations of alpha(s) in e+ e- annihilation at energies between 35-GeV and 189-GeV*, *Eur.Phys.J.* **C17** (2000) 19–51, [hep-ex/0001055].

[48] **Particle Data Group**, C. Amsler et al., *Review of Particle Physics*, *Phys.Lett.* **B667** (2008) 1–1340.

[49] A. J. Larkoski, J. J. Lopez-Villarejo, and P. Z. Skands, *Helicity-Dependent Showers and Matching with VINCIA*, *Phys.Rev.* **D87** (2013) 054033, [arXiv:1301.0933].

[50] T. Sjöstrand, *High-energy physics event generation with PYTHIA 5.7 and JETSET 7.4*, *Comput.Phys.Commun.* **82** (1994) 74–90.

[51] **OPAL Collaboration**, G. Abbiendi et al., *Measurement of event shape distributions and moments in e+ e- -> hadrons at 91-GeV - 209-GeV and a determination of alpha(s)*, *Eur.Phys.J.* **C40** (2005) 287–316, [hep-ex/0503051].

[52] **OPAL Collaboration**, G. Alexander et al., *Measurement of the $Z^0$ line shape parameters and the electroweak couplings of charged leptons*, *Z.Phys.* **C52** (1991) 175–208.

[53] **OPAL Collaboration**, J. Allison et al., *The Detector simulation program for the OPAL experiment at LEP*, *Nucl.Instrum.Meth.* **A317** (1992) 47–74.

[54] A. J. Larkoski, G. P. Salam, and J. Thaler, *Energy Correlation Functions for Jet Substructure*, arXiv:1305.0007.

[55] R. Brun and F. Rademakers, *ROOT: An object oriented data analysis framework*, *Nucl.Instrum.Meth.* **A389** (1997) 81–86.

# Acknowledgements

Zunächst möchte ich mich bei Herrn Dr. Stefan Gieseke und Herrn Prof. Dr. Dieter Zeppenfeld für die Möglichkeit bedanken, meine Masterarbeit hier am Institut für Theoretische Physik anzufertigen.

Mein besonderer Dank gilt Herrn Dr. Stefan Gieseke für die wunderbare Betreuung dieser Arbeit. Für die ständige Bereitschaft, meine Fragen und Probleme zu besprechen, bin ich ebenso dankbar wie für seine vielen hilfreichen Vorschläge. Außerdem möchte ich mich für die Möglichkeit, am *MCnet* Meeting in Manchester teilzunehmen, bedanken, sowie für seine Korrekturvorschläge zu dieser Arbeit.

Herrn Prof. Dr. Ulrich Nierste danke ich herzlich für die Übernahme des Korreferats.

Jeg vil også gerne takke Dr. Peter Skands, som altid havde tid til en snak og kom med mange hjælpsomme idéer. Jeg er meget taknemmelig for den tid jeg havde på CERN, hvor jeg havde mulighed for at arbejde sammen med Peter og lære fra ham. Specielt skal nævnes de mange beskrivelser og forklaringer af Vincia, der altid var utroligt spændende og lærerige.

*MCnet* danke ich für die Finanzierung meines Aufenthalts am CERN im Rahmen dieser Arbeit. Bei Herrn Dr. Simon Plätzer möchte ich mich für die Diskussionen zu Herwig++ und im Allgemeinen für seinen Anregungen bedanken. Für die Unterstützung im experimentellen Teil und für weitere Korrekturvorschläge danke ich Stefan Kluth und Christoph Pahl. Bei letzterem bedanke ich mich insbesondere für die Hilfe bei der Datenanalyse während meines Aufenthalts am CERN.

Für das Korrekturlesen dieser Arbeit möchte ich mich bei Alexander Wlotzka, Daniel Rauch, Maximilian Löschner, Carla Krauss und Pascal Friederich bedanken und im Besonderen bei Misha Strittmatter, Christian Röhr und Johannes Bellm.

Außerdem bedanke ich mich bei allen Instituts-Mitgliedern, besonders bei meinen Zimmerkollegen, für die freundliche und hilfsbereite Atmosphäre.

Zu guter Letzt möchte ich mich bei meinen Eltern und meiner Schwester für ihre Geduld und den Rückhalt in den letzten Jahren bedanken. Insbesondere danke ich meinen Eltern für die finanzielle Unterstützung.